6-1-2016

Synthesis and characterization of efficient polyamide thin film nanocomposite membranes

Mohamed M. A. Elleithy

The American University in Cairo

School of Science and Engineering

Nanotechnology Program

Synthesis and Characterization of Efficient Polyamide Thin Film Nanocomposite Membranes

A Thesis in

Nanotechnology

By

Mohamed M. Elleithy

Under the supervision of

Prof. Mathias Ulbricht, *Lehrstuhl für Technische Chemie II, Universität Duisburg-Essen, Germany*

Dr. Ahmed S.G. Khalil, *Center for Environmental and Smart Technology, Fayoum University, Egypt*

Prof. Amal Essawi, *Department of Mechanical Engineering, The American University in Cairo, Egypt*

Prof. Adham Ramadan, *Department of Chemistry, The American University in Cairo, Egypt*

Submitted in Partial Fulfillment of the Requirements for the Degree of Masters of Science in Nanotechnology

Spring 2016

TO MY BELOVED PARENTS AND SISTERS

ACKNOWLEDGEMENTS

I would like to express my immense gratitude to all my advisors Prof. Mathias Ulbricht, Dr. Ahmed S.G. Khalil, Prof. Amal Essawi and Prof. Adham Ramadan for their consistent support along the course of my studies. Special thanks to Prof. Mathias Ulbricht for hosting me at his research laboratories in Germany for a period of 9 months, teaching me and guiding my research activities. Without his help, this dissertation would not have been possible. Also, I'm so much in debt to Prof. Adham Ramadan for his guidance and forever cordial help. You taught me how to effectively manage my time, keep tracking of my work progress and to visualize the big picture of my work every now and then. Besides, the simplicity and interactive way of teaching that you practice during the courses makes it very informative and memorable. Thank you for everything.

I would like to thank Prof. Amal Essawi for the very fruitful scientific discussions, her help planning my experiments and her incomparable kindness. You have the attitude and the substance of a genius which is a thing I wish I could have someday. Also words can't define my great gratefulness to Dr. Ahmed S.G. Khalil who has been a leading example to me of dedication to scientific research. He has always been powering my eagerness to learn more and do more. What I have learned from him extends beyond research to cover many other skills including how to overcome burdens, long-term planning and persistence on one's goal.

I am foremost thankful to the DAAD (Deutscher Akademischer Austauschdienst) and the AUC for funding through research and travel scholarships that I was granted. Also, I would like to express my deep appreciation to all my professors in the Nanotechnology program. Special thanks to Dr. Nageh Allam, Dr. Hanadi Salem and Dr. Mohab Anis. The exceptional faculty members have given the program its essence and reputation, which in turns drawn the program success story.

I would like to thank all my colleagues Thorsten van den Berg, Anne Vaterrodt, Xi Lin, Ibrahim Elsherbiny and Nouran Ashraf for the support during my laboratory practical work. You have all shared with me your knowledge so graciously with all patience and willingness to help.

To all my friends, there must be countless favors you have done to me with the numerous speeches of support and encouragement. This endless unconditional support rendered me speechless. Whatever I would do trying to reciprocate will never be enough. Thanks a lot to Ahmed Mohyeldin, Omar Salem, Ahmed Abdelbaky, Youmna Emad, Yosra Hammoda, Ahmed Amer and Rana Elshaer.

Finally, I would like to thank my parents for their blessings and unwavering emotional and financial support during my studies. Heartfelt thanks are owned by my beloved sisters who are my true motivators.

LIST OF ABBREVIATIONS

A	Membrane area
BSA	Bovine serum albumin
CA	Cellulose Acetate
CFP	Capillary flow porometer
CSA	Camphor sulphonic acid
d	Pore diameter
DMAc	N,N-dimethylacetamide
DMF	N,N-dimethylformamide
DMSO	Dimethylsulfoxide
DLS	Dynamic light scattering
ε	Membrane porosity
ED	Electrodialysis
EIPS	Evaporation induced phase separation
FTIR	Fourier transform infrared
γ	Surface tension
H-NMR	Proton nuclear magnetic resonance
IP	Interfacial polymerization
J_0	Initial membrane flux
J_a	Membrane flux after time interval
J_w	Hydraulic permeability
l	Membrane thickness
LB3	Polystyrene latex beads
LIPS	Liquid induced phase separation
η	Dynamic viscosity
m	Membrane mass
MED	Multiple effect distillation
MF	Microfiltration
MPD	m-phenylene diamine
MSF	Multi-stage flash
NF	Nanofiltration
NIPS	Non-solvent induced phase separation
NG	Nucleation and growth
NMP	N-methyl-2-pyrrolidone
NPs	Nanoparticles
P	Pressure
PEG	Polyethylene glycol
PEI	Poly(ether-imide)
PES	Polyether sulfone
PPG	Polypropylene glycol
PSF	Polysulfone
PVDF	Polyvinylidene Fluoride
ρ_{PES}	Polymer density
RFR	Relative flux reduction
RH	Relative humidity
RO	Reverse osmosis
SEM	Scanning electron microscopy
SD	Spinodal decomposition

TEA	Triethylamine
TEG	Triethylene glycol
TFC	Thin film composite membrane
TFNC	Thin film nanocomposite membrane
TIPS	Thermal-induced phase separation
TMC	Trimesoyl chloride
UF	Ultrafiltration
VC	Vapor compression
VIPS	Vapor-induced phase separation

ABSTRACT

The availability of fresh water is directly associated with accessible natural resources. However, 2.5 billion of the world's population (around 40%) does not have access to proper sanitation systems, with 6 to 8 million annual deaths related to inadequate water supply, sanitation and hygiene in 2013. Currently, sea water desalination offers a feasible strategy to face global water challenge. Different water desalination techniques were developed and membrane desalination is currently the highest cost effective technique. Reverse osmosis (RO) system is by far considered the least expensive membrane process. Typically, RO system uses the thin film composite (TFC) membranes. A typical TFC membrane consists of two layers: a top dense polyamide (PA) skin layer (responsible for salt rejection) applied on an underlying support layer (responsible for mechanical support of the thin PA layer). Recently, a new category of membranes has emerged known as thin film nanocomposite membranes (TFNC) where nanoparticles (NPs) are incorporated into the support layer to enhance its properties.

The support layer surface pore diameters are quite crucial in supporting and preserving the integrity of the PA layer. Thus, the ideal support layer shall comprise a non-porous to slightly porous top surface. However, a support layer with non-porous surface would resist the water flow. Consequently, the main target of the work represented was to fabricate a highly porous membrane that could still support a PA layer on top of it. Membranes with symmetric cross section have high permeability due to the highly interconnected porous structure. Yet, the surface of the symmetric membranes is also highly porous; and hence, serving as a TFNC support is challenging.

Thus, this study focuses on tailoring symmetric TFNC support membranes to effectively support the PA layer. Firstly, we investigated the influence of different fabrication parameters on the support membrane properties. This entailed the understanding of the thermodynamic behavior of the cast solution during fabrication till the final precipitation of the support membrane. TFNC support membranes were prepared using cast solution of Polyethersulfone (PES) polymer in N-methyl-2-pyrrolidone (NMP) as a solvent. Afterwards, the effect of non-solvent addition was investigated using Triethylene Glycol (TEG). Furthermore, Pluronic® (Plu) and Titanium dioxide (TiO_2) NPs were incorporated in two different sets of experiments to compare the enhancement of support membrane hydrophilicity and mechanical stability.

Support membranes were fabricated using two consecutive phase separation processes, namely: Vapor-Induced Phase Separation (VIPS) followed by Liquid-Induced Phase Separation (LIPS). Various conditions were tested during the VIPS process, including relative humidity degree (RH) at exposure, exposure time and the effect of air convection during the exposure period. The cast solutions were prepared under 30% and 80% RH for exposure time ranging from 1 to 5 minutes. Forced convection condition was applied to the cast

solutions whereas compressed dry air was introduced to the cast solution during the exposure period. On the other hand, free convection condition was defined in terms of the absence of compressed dry air introduction during VIPS process.

Solution composition was systematically changed to further understand its influence on the thermodynamic behavior under VIPS process. This entailed studying the change in PES content ranging from 10 to 15 wt%, as well as the TEG (0 to 60 wt%), Plu (0 to 5 wt%) and TiO_2 (0 to 1 wt%). This variability in cast solution composition clarified the influences of the solution viscosity and hygroscopicity on the thermodynamic behavior of the cast solution, which in turns, reflected on the support membrane final morphology. Afterwards, support membranes were characterized for their cross-sectional morphology using scanning electron microscopy, pore size distribution using the capillary flow porometer, hydrophilicity using contact angle method, surface charge using surface charge analyzer and chemical composition using Fourier transform infrared spectroscopy and proton nuclear magnetic resonance. Also, membranes hydraulic permeability and wettability were tested.

Membranes fabricated under different conditions showed various structures including asymmetric and symmetric cross section morphologies. The effect of air convection was significantly important and in some cases even switched the cross section structure from asymmetric to completely symmetric. Interestingly, at low RH value (30%) and under free convection condition, membranes with semi-symmetric structure were successfully produced. This novel structure holds the privileges of both symmetric and asymmetric membranes. It showed high water permeability and mechanical stability due to the highly interconnected pores structure, as well as, having a very thin skin surface to support the PA layer on top of it. Furthermore, the semi-symmetric membrane showed higher compaction resistance (91.3%) and recovery (94%) as compared to the asymmetric membrane. As a consequence, the semi-symmetric morphology was considered as the structure of our interest as a TFNC support membrane.

Support membrane hydrophilicity, water permeability, mechanical stability and morphology are known to have high contribution to the overall TFNC membrane performance. Thus, the developed semi-symmetric structure was then reproduced using cast solutions containing the hydrophilic additives Plu and TiO_2. Results showed that the addition of TiO_2 had increased both the membrane hydrophilicity and compaction resistance. However, semi-symmetric supports were only achievable with 0.05 and 0.1 wt% TiO_2 concentrations.

As a concluding step, polyamide (PA) top skin layer was fabricated on semi-symmetric support membranes of different compositions. The final TFNC showed the higher permeability values when semi-symmetric supports were compared to asymmetric support of same composition. Furthermore, the highest TFC permeability was for support membrane containing 1 wt% Plu and that containing 0.1 wt% TiO_2.

TABLE OF CONTENTS

LIST OF FIGURES

LIST OF TABLES

Chapter 1

Introduction

Chapter 1 : Introduction

1.1. Water global challenge

Water has always been described as the main source of life and the core of sustainable development. As water resources directly contribute to food and energy production, they influence economic growth, human health and environmental sustainability. Although three-fourths of our planet's surface is water covered, 97% of which is in the oceans, 2% is unreachable fresh water and less than 1% is available for human usage [1]. Among which, only 0.3% represent accessible water with sufficient quality for direct human use.

Referring to the World Health Organization reports, 2.5 billion of the world's population (around 40%) does not have access to proper sanitation systems [2], with 6-8 million annual deaths related to inadequate water supply, sanitation and hygiene in 2013 [3,4]. Those problems arise predominantly in developing countries as shown in Figure 1.1. Even more, the problem has been exacerbated by the increasing water withdrawals. Currently, energy production and agricultural activities account for 15% [5] and 70% [6] of global freshwater withdrawal, respectively. The increasing rates negatively influence the global water cycle. In addition, such intensive wastewater production introduces more pollutants to the water system that deteriorate fresh water quality [7].

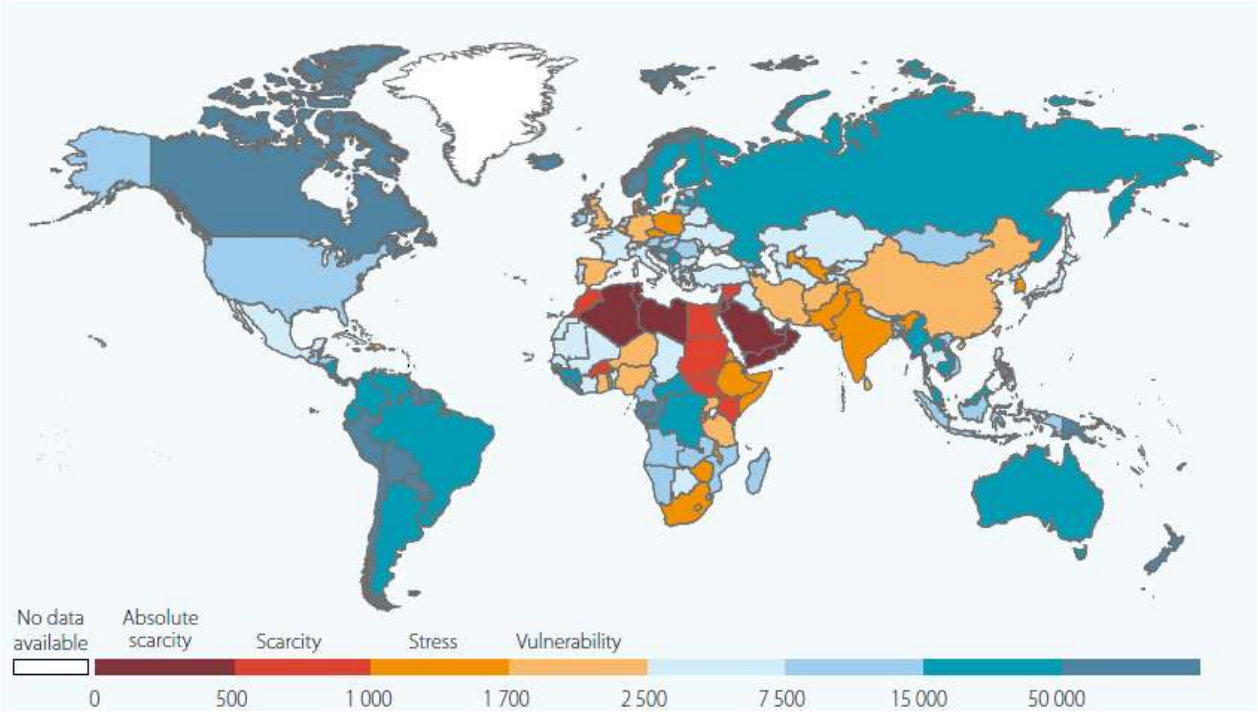

Figure 1.1: The values indicate total annual quantity from renewable water resources (in m^3/capita) [6]

Accordingly, population living under severe water stress reached 2.8 billion and expected to increase to 3.9 billion by 2050 [8]; yet, without accounting for climatic changes. According to

the UN World Water Development Report 2015, the world is expected to face 40% deficit in potable water by 2030. Furthermore, relationship between population growth and water demand has proven to be non-linear. As the world population annual growth is ca. 80 million, by 2050 world would be populated by 9.1 billion with ever-increasing water demands for domestic purposes as well as agriculture, industry and energy production [9]. Also, other factors play important role in water sustainability; including, global warming, urbanization, interest in biofuel production, quality of infrastructures and water management regulations [10,11].

From a national viewpoint, Egypt is the third most-populous country in Africa and the first in the Middle East. The rapid industrial growth and population increase in rural areas has resulted in a large escalation of demand for fresh water. According to some studies considering population expansion rates, predictions estimated Egypt population to reach 104 million by 2025 [12,13]. As a consequence, the demand for potable water in Egypt is projected to be 12.9×10^9 m^3/year by 2025 which represents 3.5 times the present demand, of approximately 3.7×10^9 m^3/year. Yet, the national annual water share from the river Nile (primary fresh water resource) has declined from 2500 m^3/capita in 1950 to about 923 m^3/capita in 2009, 680 m^3/capita in 2012 [14], and is expected to further decrease to 350 m^3/capita in 2050 which reflects severe water scarcity (water scarcity limit is 1000 m^3/capita). Furthermore, the rising conflicts with upper Nile basin countries threaten the annual national water share. Hence, the situation urges the development of cost effective renewable source for fresh water.

On the other hand, the Egyptian coastline stretches to 3,500 km along the Red and Mediterranean Seas. This represents readily accessible saline sea water. Subsequently, a viable supplemental source of fresh water is sea water desalination. Latest studies for the national status of desalination showed that it contributes to 0.76% of total fresh water production starting from 0.08 mil.m^3/d in 2007 [15], 0.166 mil.m^3/d in 2011 and increased to 0.229 mil.m^3/d by 2012 [16]. Desalination plants are mainly localized at coastal areas where extending freshwater pipelines were not considered cost effective. However, the government proposed a rescue plan with implementation of desalination plants to reach a sustainable production of 1.123 mil.m^3/d by 2037 [15]. This national plan allocated a capital investment of 10.56 billion EGPs as an initiative to promote desalination solutions.

1.2. Desalination technologies

Desalination stands for the process of salt removal from water feed to produce fresh water. This removal can take place by either one of two primary processes, namely: Thermal processes and Membrane technologies.

1.2.1. Thermal distillation

Resembling the natural hydrologic cycle, thermal processes entail phase change that involves heating up of saline water to its boiling point. Steam produced from evaporation condenses back on a collector producing fresh water. The major adopted distillation

technologies are multi-stage flash (MSF), multiple effect distillation (MED) and vapor compression (VC).

A. Multistage Flash Evaporation (MSF)

The process consists of several successive chambers of decreasing pressure. Due to sudden pressure reduction from one chamber to another, the preheated feed water is vaporized. Afterwards, the process is repeated stage-by-stage through successive chambers of decreasing pressure. The vapor produced condenses on heat exchange tubes carrying the new feed solution so as to heat it up and minimize energy losses. Concomitantly, the vapor condensate on the tubes drips into the fresh water reservoirs [17]. The concentrated saline solution remained after the process is discharged. The feed solution temperature decreases as water evaporates. Accordingly, the process requires external heating power with relatively high energy consumption to further induce water evaporation. Process efficiency could be increased via increasing the temperature used. Yet, heating up the system could promote scale formation and system materials corrosion. On the other hand, increasing the efficiency by increasing the number of stages would substantially increase the capital costs [18].

B. Multi Effect Distillation (MED)

Multi Effect Distillation, as another technology of thermal desalination, has a relatively low recovery percentages compared to other thermal technologies. The process involves heating up the feed solution using steam from burnt fuel. The feed solution is sprinkled on tubes containing hot steam. This induces the evaporation of water from the feed solution. The water vapor is then collected as fresh water that moves through tubes in the following chamber to act as a heater. The remaining feed solution which was not evaporated is pumped to the following chamber of lower pressure. Again, the feed is sprinkled on tubes that contain fresh water vapor produced from the previous chamber which act as a heater. The produced vapor is used to heat the feed for the next stage to eliminate the energy consumption. Once vapor is generated as a secondary steam, it goes to the next chamber and transfer its latent heat to the low temperature feed solution [19]. This process is repeated in successive stages depending on the required production capacity. At the end, brine is discharged and water vapor is collected as fresh water produced.

C. Vapor Compression (VC)

Vapor compression desalination refers to a distillation process where feed solution is preheated using compressed vapor. The preheated solution is then drawn to a chamber and allowed to evaporate using tubes containing compressed vapor. The produced water vapor is collected and compressed. Then the compressed vapor moves through heat exchange tubes to heat the feed water in the chamber and preheat the feed before entering the chamber. Afterwards, the compressed vapor loses most of its latent heat through the exchange process. Accordingly, it exits the cycle as produced fresh water. On the other

hand, the remaining brine is discharged. The evaporation chamber also includes an external heater to supplement the heat exchanger in inducing feed evaporation [20].

1.2.2. Membrane processes

A membrane is defined as a selective barrier interphase between two phases. Cost effectiveness and small environmental footprint render polymeric membrane more advantageous compared to thermal processes. In addition, as membrane technologies are easier to up-scale and are performed isothermally, their integration with other processes such as a selective separation step is more feasible [21]. However, membranes are prone to fouling which decreases the membrane lifespan and increases the costs of the process. Investigations are focusing more on polymeric materials as they are relatively inexpensive, easier to fabricate and could be modified to produce more chemical selective separation membrane compared to ceramic membranes.

Regardless of the membrane material, the aim of membrane development is to increase membrane flux, rejection and resistance to fouling [22]. This is mostly influenced by membrane pore size and hydrophilicity. Membrane pore diameters need to be appropriate to the intended separation application. However, smaller pore size membranes are not necessarily better. As they require more energy for operation. Accordingly, a trade-off between size exclusion performance and membrane throughput is the main motive for further development of membranes for different processes.

A. Electrodialysis (ED)

Electrodialysis represents a process of demineralization of water and other fluids containing ionic salts using a constant electric field and selective ion-exchange membranes. Feed solutions pass between selective membranes and dissolved ionic solutes dissociate due to an external applied electric field. The ions pass through the respective selective ionic membranes leaving fresh water behind. The ion-exchange membranes are polymeric films with ionic groups trapping and exchanging ions.

The principle of multi-chamber electrodialysis is applied using a set of separated alternating cation exchange and anion exchange membranes between two external electrodes. The positive ion species crosses the cation exchange membrane. Once the cation crosses it is trapped in the new compartment as there is an anion exchange membrane. Same process happens to the negative species with after crossing the anion exchange membrane. Thus, demineralized and concentrated solutions flow in alternative compartments and are separated accordingly [23].

B. RO desalination

When two solutions of different salinities are mixed, the solutes are distributed equally throughout the whole solution. This takes place through solute diffusion from regions of high concentration to low concentration. When both solutions are separated by a semi-permeable membrane allowing only the passage of water molecules, water molecules will

spontaneously diffuse from the low concentration solution to the high concentration solution side (osmosis process). This diffusion is driven by osmotic pressure difference, which is dependent on the difference of solute concentrations in the two solutions. RO involves the application of pressure on the solution with high salt concentration. This pressure exceeds the osmotic pressure difference between the two solutions. Accordingly, it creates a net force which drives the water molecules from the high concentration solution to the lower concentration solution through the semi-permeable membrane. This process can be used to produce fresh water as shown in Figure 1.2 [24]. Thus, for the RO systems, 87% of the operational costs account for electricity (energy), labor and chemicals for feed pretreatment [25]. Membranes with higher flux and higher fouling resistance can reduce energy and chemical pretreatment costs. Thus, membrane material development is essential for increasing the cost effectiveness of RO process.

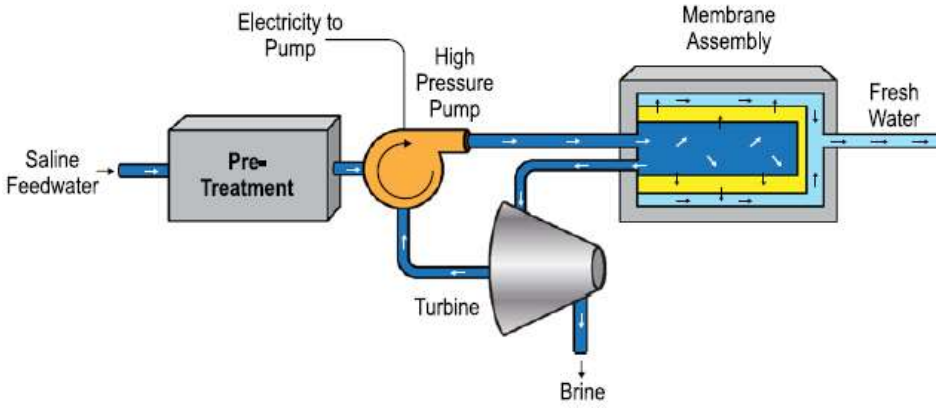

Figure 1.2: Schematic representation of RO desalination system [24]

1.2.3. Energy requirements and economics of desalination processes

Theoretically, the absolute minimum energy for salt removal from water regardless of technology using Van't Hoff formula is 0.8 KWh/m^3 (≈3 KJ/Kg) [26]. The formula is used to calculate the osmotic pressure exerted by a salt solution.

Equation 1: $$\pi = cRT$$

Where π is the osmotic pressure (bar), *C* is the molar concentration of the salt ions, *R* is the universal gas constant (L.bar/K.mol) and *T* is the temperature in degree Kelvins.

For simplification, we assume that the seawater salt concentration is equivalent to aqueous solution of 33 g/L NaCl. According to Van't Hoff formula, this solution has an osmotic pressure of 27.8 bar or (278000 kg/m^2). Desalination process entails the displacement of water from high concentration solution to low concentration solution against the osmotic pressure difference. Thus, the minimum theoretical energy required is calculated as the

work done on seawater of cross sectional area 1 m^2 to displace it 1 m against its osmotic pressure using the following equation:

Equation 2: $$W = F.x$$

Where *W* is the work done expressed in (J), *F* is the force due to osmotic pressure (N) and *x* is the displacement (m).

The concept of minimum energy requirement is well established based on the calculation of the difference in free energy between feed (saline water) and permeate (fresh water) assuming a salinity of 33,000 ppm at 100 ^{0}K [27]. This value considers complete reversibility of all operations with no energy losses; thus, unrealistic. The practical minimum consumption is orders of magnitude of the theoretical value which has been estimated to be approximately 5 KWh/m^3 for RO systems and 50 KWh/m^3 for thermal processes [28].

Membrane technologies (RO and ED) consume relatively lower energy as it only requires electricity to run the pressure pumps. On the contrary, MSF, MED and TVC processes require two sources for energy: thermal and electrical. Also, thermal processes necessitate the use of thermal resistant system components, large spaces and descaling chemical pretreatment; which in turn increase the capital investment. Table 1.1 presents the average costs for water production by the major desalination processes.

Table 1.1: The average costs for water desalination based on feed salinity of 33,000 ppm using various desalination technologies

Process	Capacity (x10^3 m^3/d)	Production cost ($/$m^3$)	Reference
MSF	23-528	0.56–1.75	29,30,31,32
MED	91-320	0.52–1.01	33
VC	30	0.87–0.95	34
RO	100-320	0.45–0.66	35

Generally, all thermal desalination processes produce water with much lower dissolved salts compared to potable water named distilled water. Many research activities have been conducted to evaluate the health effects of drinking distilled water with highly reduced salt content, and it was found that this has negative impact on human health [36]. This in turns necessitates the post treatment process of solute addition before reaching end users, which reduces the cost effectiveness by adding further expenditures.

Shown in Figure 1.3 [37] is the market share of each desalination technology. Considerable attention world widely is drawn towards RO systems for their cost effective production of desalinated water. Thus the global market showed technology switching from thermal to membrane desalination systems since early 21st century [38], as represented in Figure 1.4 [39]. As a result, adopting this technology is of great benefit to our national development

using state-of-art technology. Still, further development of membrane materials is required to increase its life span, hydraulic permeability and decrease its carbon footprint.

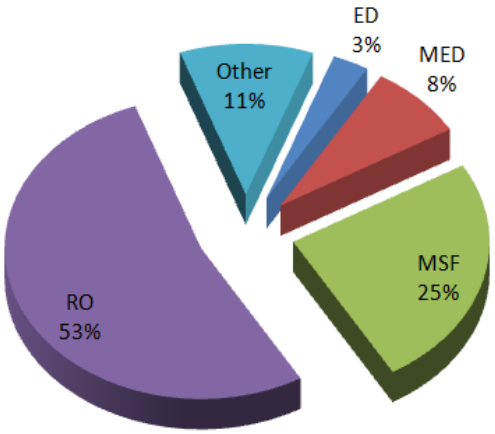

Figure 1.3: Global market share of different desalination technologies [37]

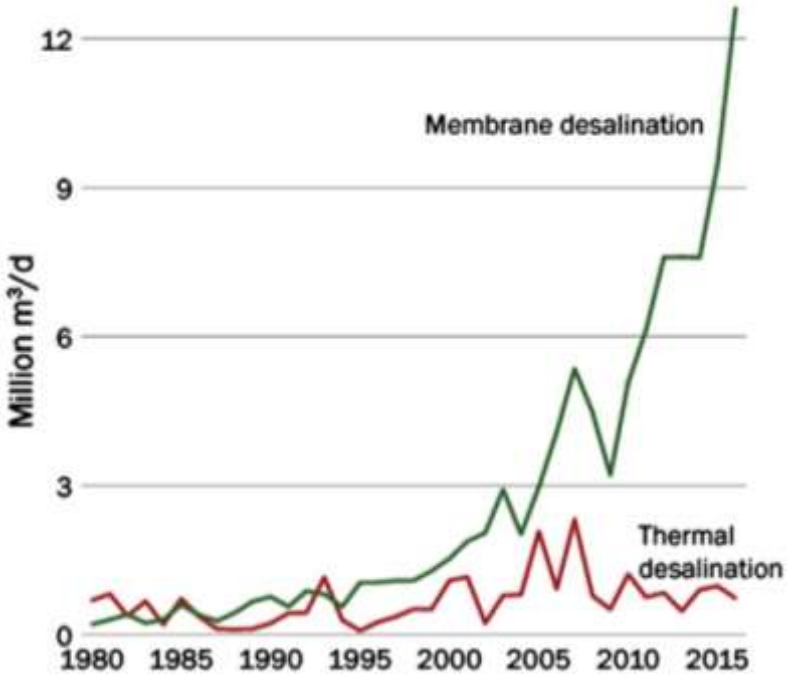

Figure 1.4: Global market adoption of membrane versus thermal desalination technologies as of 2002 [39]

1.3. Thin Film Composite Membranes

The first breakthrough in membrane technology in the field of desalination RO membranes was in 1957 when Reid and Breton successfully developed a Cellulose Acetate (CA) dense membrane with high salt rejection values. Almost 6 years later, Loeb and Sourirajan fabricated the first asymmetric CA membrane [40]. The developed membrane had highly porous inner membrane structure, yet, comprises dense skin layer responsible for solute rejection. Thus, it showed superior performance for salt rejection and approximately 10 folds enhancement of water flux compared to dense CA. This performance encouraged the

commercialization of the asymmetric CA membranes for microfiltration and ultrafiltration applications. Furthermore, the impact of membrane structural change was inspiring for the development of Thin Film Composite (TFC) membranes [41].

The TFC membrane synthesis comprises two polymeric layers: a support layer and an active layer. Typically, the support layer is an asymmetric membrane with dense surface layer that is not sufficient to reject solutes, but which could effectively support the active layer on top of it. The active layer is applied on the support using interfacial polymerization (IP) process. With IP, Cadotte et. al synthesized a very thin polyamide active layer of <0.2 µm thickness that increased the solute rejection as a promising RO membrane [42]. However, the support structure and features have significant influence on the overall performance. In this regards, researchers used supports with different structures to study their influence on RO performance.

Based on the membrane cross-section structure, membranes are divided into two categories: isotropic (symmetric) and anisotropic (asymmetric) membranes as shown in Figure 1.5 (a) and (b) respectively. As seen in the micrographs, there is a significant variation in the cross-section morphology between both types. Accordingly, each type holds its own advantages based on that morphology. Anisotropic membranes, for instance, are well known for their top skin layer that could effectively support the application of polyamide thin film on the surface. On the contrary, the relatively large surface pores of the isotropic membranes allow them to have significantly higher flux rates.

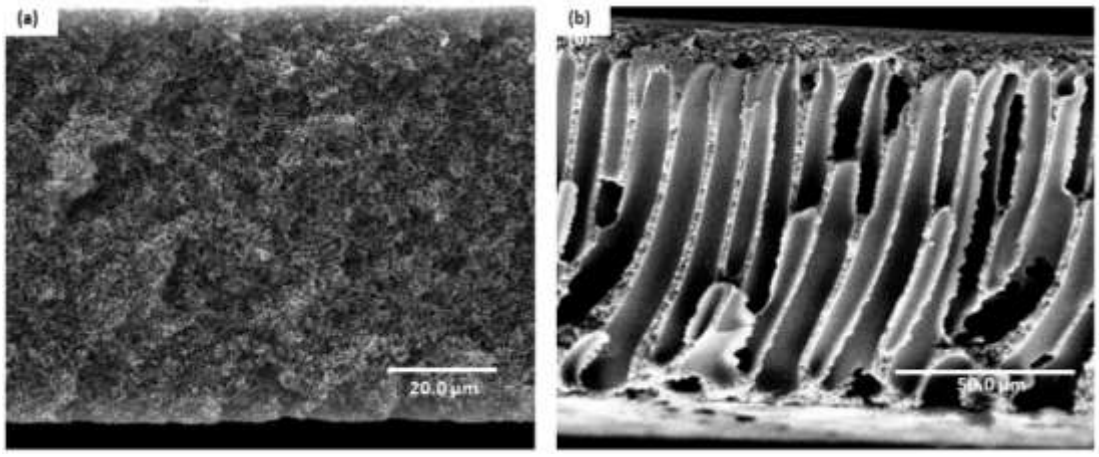

Figure 1.5: Major membrane category based on cross sectional morphology (a) isotropic membrane and (b) anisotropic membrane (retrieved from results)

In practice, membranes are packed in well-sealed modules to have high surface area of membrane filtration in relatively small space. The spiral-wound module is shown in Figure 1.6 which is one of the most common modules currently used. Such modules allow the use of hundreds of square meters of membranes to increase the throughput. Consequently, a relatively small enhancement in membrane flux corresponds to orders of magnitude increase in the process throughput capacity and decrease in energy consumption.

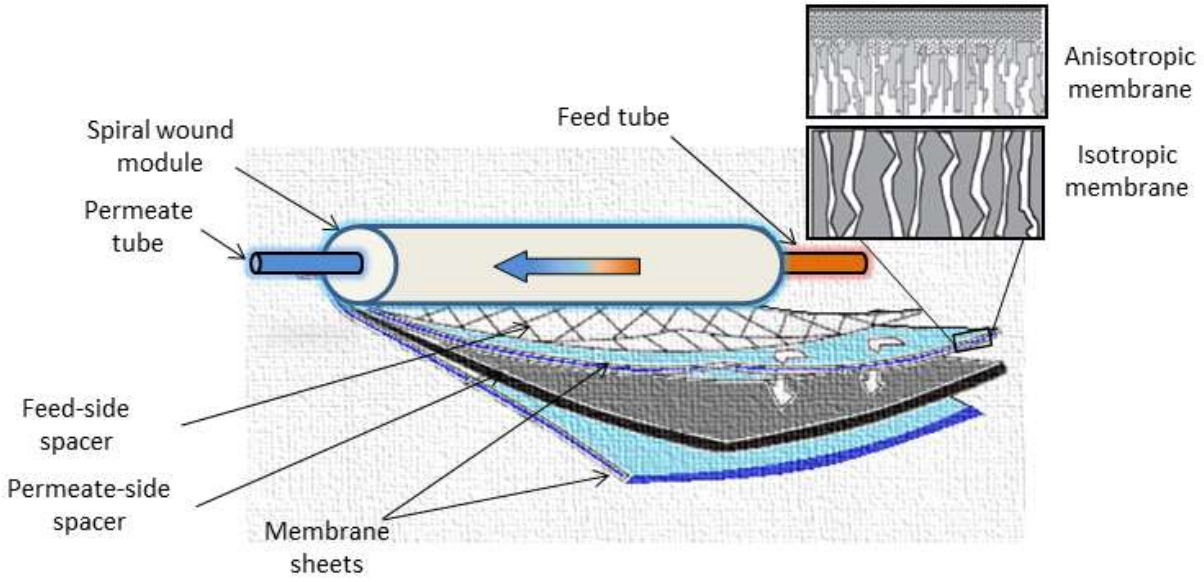

Figure 1.6: Schematic presentation of spiral-wound module [43]

On the other hand, the mean flow pore diameter of the membrane identifies its application. Based on pore diameter, membranes are of four major types: (1) Microfiltration (MF), (2) Ultrafiltration (UF), (3) Nanofiltration (NF), and (4) Reverse Osmosis (RO) membranes. Figure 1.7 represents the selective separation of each membrane type with respect to its average pore diameter.

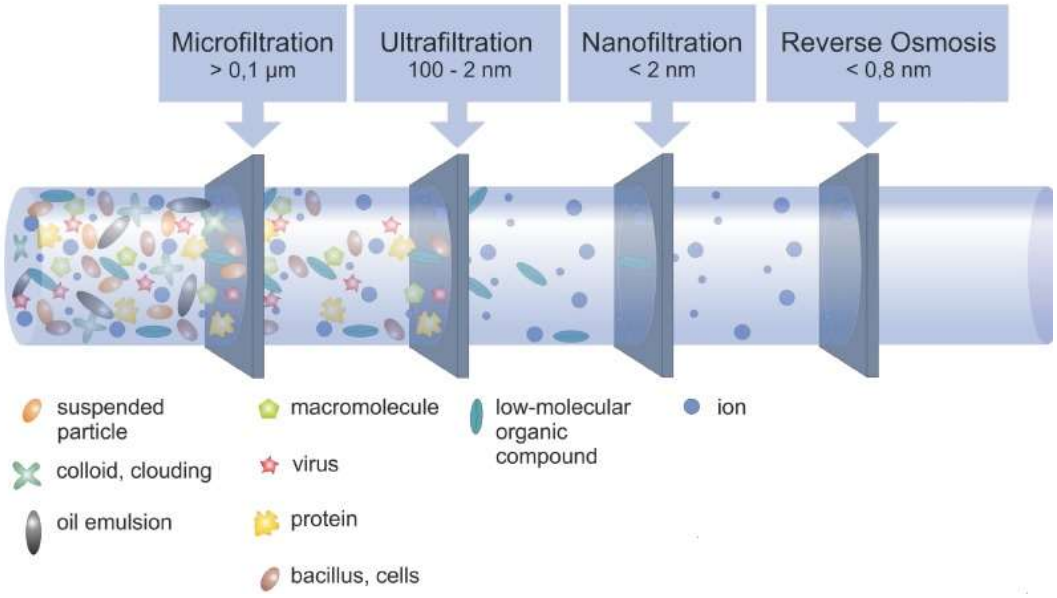

Figure 1.7: Schematic representation of membrane selective separation based on mean flow pore diameter [44]

Currently membranes are widely commercialized for many applications. For instance, dialysis membranes, controlled release drug delivery systems, gas separation and water desalination. Membranes market value increased from less than $ 20 million in 2003, to

21.2 billion $ in 2013 and is forecasted to reach $ 39.3 billion by 2019 [45]. These figures reflect the importance of membrane development and the need to acquire a national hands-on experience to the state-of-the-art in this field.

1.4. Statement of purpose

This research aims at improving the TFC membrane performance by modifying the support layer. Pursuing this goal, we started with adopting a highly porous, large pore diameter MF membrane developed earlier that had superior MF performance compared to commercially available MF membranes. The effect of different parameters on the final membrane morphology was investigated. In accordance, membrane morphology was tailored with controlling fabrication process parameters to obtain more efficient TFC support membrane. The membrane pore size tailoring and properties optimization were conducted through two main work phases:

1. Understanding the effect of changing various VIPS parameters on the thermodynamic and kinetic behavior of the cast solution through characterizing the final membrane structure, and hence, the fabrication of efficient TFNC support-membrane. This took place through breakdown of different parameters to be understood individually.
    a) Studying the effect of varying non-solvent and hydrophilic additive contents in the cast solution on the final membrane structure. This is done in order to optimize the membrane hydrophilicity.
    b) Studying the effect of adding TiO_2 nanoparticles to the membrane material on the TFC support layer flux and compression resistance.
    c) Studying the effect of casting parameters influencing membrane morphology. This entailed the study of varying RH value and exposure time. Also, changing the convection conditions in the humidity chamber during VIPS process. This is conducted so as to optimize the adopted MF membrane pore diameter to achieve TFNC support layer with relatively high water flux; yet, pertain structure that could successfully substitute the typical asymmetric TFNC support layer.
2. Testing the performance of membrane samples with different pore structure as a microfiltration membrane and TFNC support layer.
    a) Testing the filtration performance of support membranes using polystyrene latex beads.
    b) Testing the support membranes with different cross section morphology for compaction resistance.
    c) Testing the TFNC membrane performance in RO system for salt rejection and permeability.

Chapter 2

Literature Review

Chapter 2 : Literature Review

This chapter serves to highlight the main research endeavors developing membranes with different morphologies intended for various applications. The main focus will be on the effect of fabrication process parameters to tailor membrane cross sectional morphology, in addition to highlighting the effect of different membrane additives. Further to that, we will present some of the activities done to study the effect of support layer on TFC membrane performance in RO process and enhance TFC membranes' support using TiO_2 nanoparticles (NPs). At last will be a review of the synthesis of TFC active layer.

2.1. Phase separation process

Phase separation processes introduce non-solvents, either in a liquid or vapor phase, to the cast film during membrane fabrication. Some phase separation techniques aim at the out-diffusion of the solvent from the cast solution rather than the in-diffusion of the non-solvent. Thus, regardless of the methodology, phase inversion takes place by decreasing polymer stability in the solution forcing it to aggregate or coalesce to form a solid membrane [46]. This transformation from stable state to the final coagulation forming a membrane can be accomplished by several methods, including [47]:

1- Thermally induced phase separation (TIPS): where the decrease in solution temperature will decrease the degree of polymer solubility. Thus, polymer precipitation takes place and the membrane is formed. Afterwards, the solvent is removed by extraction or evaporation [48].
2- Non-solvent induced phase separation (NIPS): This process takes place through the exposure of the polymer homogenous solution to relatively large amount of non-solvent. The non-solvent replaces the solvent in the cast solution and decreases the polymer stability. This process is categorized into either liquid induced phase separation (LIPS) or vapor induced phase separation (VIPS) where non-solvent is introduced in its liquid or vapor phase, respectively [49].
3- Evaporation induced phase separation (EIPS): In this process the solvent used should have a high vapor pressure. After homogenous solution casting, the cast film is allowed to stand for the solvent to evaporate causing the loss of solution stability and the polymer precipitation [50].

2.1.1 Non-solvent induced phase separation

Among all the different phase inversion techniques, NIPS processes are the most commonly used to fabricate membranes with wide range of morphologies [51]. The homogenous polymer solution is initially cast on a suitable support using a blade of specific thickness. Directly afterwards, the cast film is drawn to a humidity chamber to undergo VIPS then to the final coagulation bath for LIPS process to take place. During the process of combined VIPS/LIPS, parameters control effectively tailors the membrane final morphology relying on the thermodynamic behavior of the cast film and the process kinetics.

In 1981, VIPS was firstly introduced by Zsigmondy and Bachmann [52] followed by a comprehensive description for the process by Elford [53]. Since then, VIPS drew attention due to its capability of synthesizing membranes with various morphologies. Typically the process entails the preparation of cast solution with 3 to 4 components (polymer/solvent/non-solvent/additive) which is then casted as a thin film on appropriate substrate that is exposed to non-solvent in its gaseous state. Afterwards, the cast film is immersed in a non-solvent bath for complete precipitation of the polymer (i.e. combined with LIPS) or for washing the membrane matrix from solvent traces. Thus in VIPS process, phase separation is governed mainly by non-solvent inflow rather than solvent outflow. From materials perspective, literature mainly focuses on four polymers; namely, PVDF [54,55,56], PES [57,58,59,60,61], PSF and PEI [62,63]

2.1.2 Achievable morphologies using VIPS

The structure variety starts from highly porous symmetric structure to asymmetric with dense top layer. The four main morphologies are:

a- *Symmetric cellular structure:* this occurs mainly when non-solvent inflow is relatively slow and precipitation takes place via spinodal decomposition process (SD) with no further slow coarsening of polymer domain. On the other hand, the asymmetry might arise from the formation of surface liquid layer that creates concentration gradient; hence, large cellular pores are formed near the cast film/air interface.

b- *Symmetric nodular structure:* this structure results from a process known as "crystallization-initiation gelling" when the polymer used is semi-crystalline or crystalline in relatively high concentration. In such a case, the growth of crystalline domain before, or at an early stage of solution gelling, results in the final nodular structure. Li et al. showed that the dissolution temperature used during cast solution preparation could affect the final membrane structure through altering the time of inducing the crystallization process [64]. Using PVDF cast solution, they found that increasing the dissolution temperature resulted in more nodular structure as the crystallization was initiated during the gelling process. However, at a dissolution temperature below 40^0C, the membrane cross section was lacy and bi-continuous.

c- *Sponge-like, lacy or bicontinuous structure:* it is the most desirable structure for applications requiring high fluxes. The interconnectivity of porous structure retains low resistance to fluid permeation. However, it is less common to reach such a structure due to the rapid transformation to either a cellular or a nodular structure with polymer vetrifiction progress. Thus preserving the bicontinuous structure is challenging and typically requires slow kinetics with the modulation of polymer dissolution temperature and an optimizing solution viscosity. Nguyen et al. studied the effect of polymer nature on the final membrane structure [65]. They concluded that semi-crystalline polymers undergo crystallization after liquid-liquid phase separation not during solution gelling. This resulted in an interconnected porous

structure. On the contrary, amorphous polymers tend to form a cellular structure as no crystallization took place while the precipitation took place through SD.

d- *Asymmetric finger-like structure:* this structure is more common with LIPS process. Yet, using combined VIPS/LIPS might develop the same morphology when the exposure to humid air is significantly short. It results from the abrupt precipitation of polymer from the top cast solution surface forming a dense skin once immersed in a non-solvent bath. The skin inhibits the further diffusion of the non-solvent to the deeper layers allowing time for macrovoid growth forming the finger-like pores.

2.1.3 Thermodynamics and kinetics of phase inversion

The thermodynamic behavior of the cast solution system and its representative phase diagram is dependent on the system components. In the membrane casting process, the typical cast solution is made up of two (polymer/solvent), three (polymer/solvent/non-solvent) or four components (with additive). Hereby we will focus on the ternary system thermodynamic isotherm as the cast solution used in our study is composed of (polymer/solvent/hydrophilic additive). The study of the thermodynamic process started with the earlier work of Micheals in 1971 [66]. As shown in Figure 2.1, the triangular phase diagram three vortices represent the pure system components of polymer, solvent and non-solvent. The homogenous cast solution starts at a point in the stable (homogenous) region that corresponds to the ratios between the three components. As the non-solvent concentration increases through its in-diffusion to the system or the out-diffusion of the solvent, the solution composition shifts forward until it crosses the binodal boundary reaching the metastable region. In the metastable region the solution starts to separate into two phases, a polymer-rich phase and a polymer-lean phase. If the initial polymer concentration is above the critical point where the binodal and spinodal curves intersect, the polymer-lean phase will start nucleating in the polymer-rich phase directly after crossing the binodal boundary. On the contrary, the polymer-rich phase nucleates if the initial polymer concentration was below the critical point. In either case, the process of nucleation and growth (NG) takes place until the system composition crosses the spinodal boundary.

Crossing the spinodal boundary brings the system to the unstable region where the polymer solution starts to instantaneously separate to two distinctive phases. The two phases exist in a thermodynamic equilibrium state with compositions linked by the tie lines. As this phase separation progresses, the polymer is precipitated and vetrified via spinodal decomposition (SD). The polymer rich phase forms the final membrane skeleton, while the porous interconnected structure is the conclusion of the polymer-lean phase existed during NG process in the metastable region. On the other hand, if the NG took place through the polymer rich phase (below the critical point), the resultant will be polymeric powder in a continuous liquid phase.

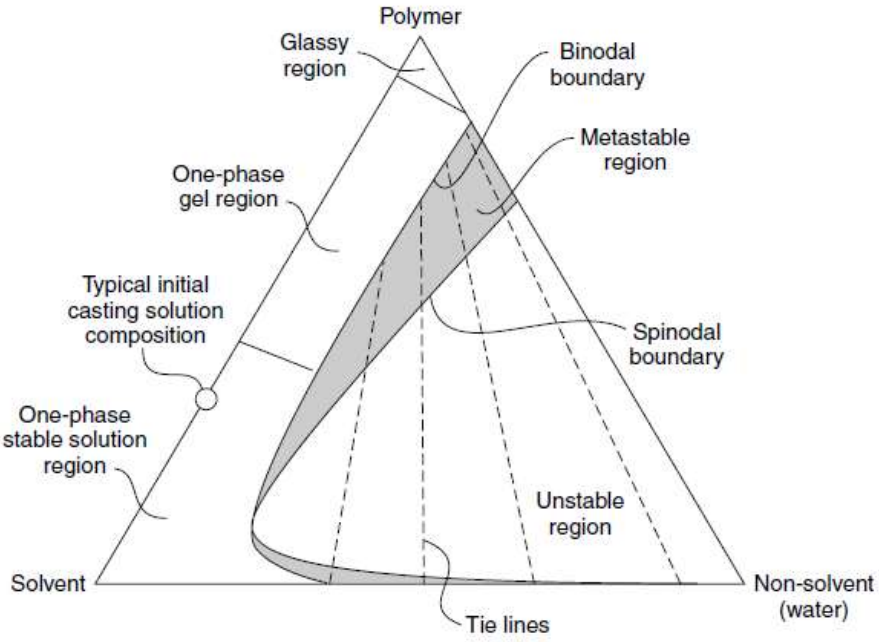

Figure 2.1: Thermodynamic ternary phase diagram representing different stages of stability of a cast solution [67]

The final membrane morphology is also ascribed to the kinetics of the phase inversion process. As the rate of solvent/non-solvent demixing changes, the membrane final structural is dramatically influenced in terms of the pore diameter and cross sectional morphology. Thus, parameters that could tailor the membrane pore diameter and porosity rely mainly on manipulating the kinetics of phase separation.

In 1987, Smolders et al. attempted to study the diffusion processes in the ternary system used by Loeb and Sourirajan for the fabrication of asymmetric CA membranes. They prepared a diffusion model to calculate the composition path of CA/acetone/water system in the ternary phase diagram. They used light transmission analysis to measure the time taken until the system starts the liquid-liquid demixing. They concluded that the formation of skin and underlying dense sublayer for the asymmetric structure resulted from the higher polymer concentration at the upper layers of the cast film. The phase separation technique used was LIPS and the high polymer concentration at the surface was a result of rapid liquid-liquid demixing and removal of the solvent near the interface [68].

On the other hand, formation of macrovoids in the membrane sublayer has been attributed to many factors. Researchers argued that the onset of macrovoid formation is at the interface between cast film and coagulation bath. Steven et al. proposed that interfacial tension gradients initiate convective cells that create the macrovoids [69]. Furthermore, Ray et al. added that these convective cells are due to the steep concentration gradient at the interface [70]. While Strathmann et al. claimed that the macrovoids initiation points are caused by the mechanical stresses at the interface [71]. On the contrary, Smolders et al. argued that the macrovoid initiation should not be attributed to interfacial phenomena, as

some macrovoids appear to start at a large distance from the interface and that the interfacial effects would be nullified by the high solution viscosity. They suggested that macrovoids are formed by the expansion of a polymer-lean nucleus in the cast film. This expansion would only take place if the diffusion front of the nucleus is subjected to stable composition in the cast film (i.e. delayed demixing onset condition). The stability at the nucleus front arises from the increased solvent concentration as a result of further expansion of the nucleus away from the interface. Additionally, the skin barrier formed from instantaneous demixing at the interface prohibits further introduction of non-solvent to the nucleus. Therefore, the nucleus keeps expanding by imbibing solvent from the stable front at a rate higher than the flow of the non-solvent from the nucleus to the polymer solution. Such expansion would be hindered if new nuclei are created not far from the expanding nucleus [72].

Wang et al. studied the effects of the surfactant degree of miscibility with the non-solvent in the coagulation bath on the formation of macrovoids. Results showed that larger macrovoids were formed when the surfactant used had higher miscibility with the non-solvent, hence facilitating the non-solvent inflow to the sublayer. They examined the time elapsed for macrovoid formation and concluded that the initiation of macrovoid takes less than 2 seconds. On the other hand, the expansion of the macrovoid was found to be independent of the surrounding environment after macrovoid initiation. In other words, once the polymer-lean phase nuclei were created in the cast film, macrovoids started to propagate whether the cast film is still in the coagulation bath or left on air. They also found that the growing speed of a macrovoid is higher than the non-solvent penetration speed from the coagulation bath [73]. These results agree with the explanations in the preceding paragraph for mechanism of macrovoid initiation and growth providing more evidence that macrovoid growth is to a certain limit independent from interfacial phenomena.

2.1.4 Effect of VIPS parameters on membrane morphology

A. Polymer concentration

Polymer concentration mainly alters process kinetics through changing the solution viscosity. However, it also has an important effect on the thermodynamic stability of the cast solution. Di Luccio et al. showed that by increasing polymer concentration, the solution become thermodynamically less stable and less water is required to precipitate the solution [74]. But from a kinetics perspective, increasing viscosity by increasing the solution polymer content hinders water uptake (slower kinetics). As a result, two contradictory factors interplay in the process of VIPS when the polymer concentration is increased: facilitated precipitation due to a thermodynamic effect and delayed precipitation due to the slow kinetics of non-solvent absorption.

To better understand the influence of polymer concentration, Barth et al. investigated the thermodynamic behavior of the polyethersulfone (PES)/N,N-dimethylformamide (DMF)/water system. They found that PES concentration of 8.5 wt% introduced the system

to SD upon immersion in the coagulation bath, as the system passed directly through its critical point to the unstable region. They recommended the use of higher PES concentration, because relatively low PES content lead to the formation of large finger-like pores and skinless structure. Consequently, the membrane lost its separation property. It was also found that increasing PES to 16 wt% or above decreased the number of macrovoids and membranes had thicker and denser skin layers [75].

Lee et al. examined the water uptake of PSF/NMP system under a combined VIPS/LIPS process. Although the water vapor uptake was approximately similar for 15, 20 and 25 wt% polymer concentrations, the time elapsed to reach phase separation under humid air was inversely proportional to the polymer concentration. In other words, increasing polymer concentration shortened the time required to cross the binodal boundary. It is however worth mentioning that the solution viscosity increased, but the effect of viscosity was not considered in their study. Their experiment showed that the cast solution containing 15 wt% PSF took approximately 13 min under 90% RH to reach unstable condition. Consequently, SD was induced by an absorbed vapor concentration of 5.8 wt% [76].

Atinkaya et al. developed a model to determine the effect of the polymer/non-solvent ratio on the membrane final morphology using the EIPS/LIPS process. Results confirmed that the cast film-air interface reached the binodal boundary earlier than the bulk of the cast film regardless of the initial polymer to non-solvent ratio. They stated that solvent evaporation started from the surface followed by solvent diffusion from the inner layers of the cast film to its top layers. The solvent diffusion carried the dissolved polymer in the direction, creating a higher polymer concentration at the top layer of the cast film. Furthermore, the precipitation started earlier for the cast solutions with higher non-solvent content, whereas increasing the polymer content resulted in higher concentration at the top layer and the formation of a denser membrane skin [77].

Su et al. used FT-IR microscopy to examine the phase separation process for a PS/NMP/water system. They investigated PS concentrations of 10 and 20 wt% under 70% RH. The results demonstrated that phase separation took place by SD throughout the whole cross section of the 10 wt% PS cast film. On the contrary, with 20 wt% PS, the cast film remained longer at the metastable region as a result of three main factors. The first was the delayed propagation of absorbed water vapor as a result of the increased viscosity. The second aspect delaying the vapor absorption was the formation of a skin layer after 3 min exposure to humid air. Due to interfacial tension near the solution-air interface, the polymer-rich phase coarsened and formed the skin layer. The third factor was that 20 wt% PS cast solution had wider gap between binodal and spinodal boundaries. Accordingly, more water was required to bring the system to SD, and thus, the formed cross section morphology was mainly due to NG rather than SD [78].

Another factor that interplays with polymer concentration is the interfacial temperature difference between the cast film and the surroundings. According to Henry's law, the

increase in polymer concentration decreases the solvent vapor pressure. It was also proven that during NG, the growth of polymer-lean droplets is directly proportional to the temperature difference at the interface [79]. Zhiping et al. examined the effect of using PES with increasing concentration with respect to RH and temperature under VIPS process. Their findings showed that pore size increased with the decrease of PES concentration, the increase of PES molecular weight or the increase of RH degree. Results were explained in light of the interfacial temperature difference where the degree of solvent evaporation increases with decreasing the PES content, thus, the temperature difference at the interface increases. Accordingly, polymer-lean droplets grew faster and resulted in larger final pore sizes [80].

In 2012, Peng et al. studied the effect of vapor temperature with solutions of increasing PVDF on the final morphology prepared by VIPS process. They concluded that at high polymer concentration, the solid-liquid demixing taking place in the thermodynamic stable region could have enough time for polymer to crystallize. Therefore, the polymer crystallization resulted in a porous skin layer upon complete precipitation. Furthermore, the pore size at the top surface increased with increasing vapor temperature from 27 to 75 ^{0}C. This substantiated that the interfacial temperature difference had high influence on surface nuclei growth [81].

Holda et al. postulated that the increase in polymer concentration increases the solution viscosity exponentially and decreases the quantity of non-solvent required to initiate precipitation. Therefore, the delayed kinetics substantially delays demixing process and macrovoids decreased with increasing polymer concentration [82].

B. Type of solvent

Solvency power is considered a key factor affecting the kinetics of phase separation. When solvency power is low, a small quantity of non-solvent could induce phase separation. As a result, asymmetric morphology is often obtained. Generally, for a suitable phase separation process to occur, the solvent has to have a relatively high solvency power to the polymer in question, along with adequate miscibility with the non-solvent. Theoretically, Hansen suggested that solubility parameters are affected by hydrogen bonding, polar forces and dispersion forces between solvent and polymer [83]. Accordingly, it is possible to determine the appropriate solvent by comparing solvent and polymer solubility parameters to properly create a membrane forming cast solution.

Wei et al. generated the ternary phase diagram for PES/solvent/water system. Among the solvents tested with this model was NMP which showed the highest miscibility gap with PES as compared to N,N-dimethylacetamide (DMAc), N,N-dimethylformamide (DMF) and dimethylsulfoxide (DMSO) as NMP showed the lowest interaction parameter with PES. It was therefore concluded that NMP would serve as a better solvent for PES. Increasing the interaction parameter between non-solvent/solvent (i.e less miscible) increases the miscibility gap, which is reflected in the increase of the thermodynamic stable region.

However, with the increase in polymer/solvent or polymer/non-solvent interaction parameters, the miscibility gap decreased and the solution is less stable [84]. The recommendation of NMP as a PES solvent was later practically confirmed by the work of Brazin et al. [85]

Barzin et al. calculated water/NMP and water/DMAc interaction parameters based on the Flory-Huggins equation. They found that water/DMAc has a lower interaction parameter, and hence, narrower miscibility gap, as DMAc has a higher affinity to water than that of NMP to water. Phase separation using LIPS process of PES/DMAc/water solution resulted in a membrane with a sponge-like cross-sectional morphology [85]. They also evaluated the morphological structure of both systems in order to develop a better understanding of macrovoid formation using LIPS process. In the DMAc/water system macrovoids were inhibited. This observation was strikingly opposite to the widely accepted rule of macrovoid formation which postulates that the better the mixing between solvent and non-solvent, the higher is the formation and expansion of macrovoids. Yet, they ascribed this phenomenon to the process of polymer vitrification [86].

In the ternary phase diagram, the line that separates the homogenous solution region from the polymer glass region is called the vitrification boundary. The intersection between the vitrification boundary and the binodal boundary is the Berghmans' point. The tie line passing through this point determines the gelation boundary. According to Barzin's calculations, which included the data reported by Li et al., the gelation boundary for the PES/DMAc/water system is closer to the binodal boundary than that for the PES/NMP/water system [87]. In this respect, the gelation of PES occurs at a relatively lower non-solvent concentration when DMAc is the system solvent. Thus, the earlier gelation prevented the progression of the macrovoids through increased viscosity.

Han et al. studied different PES-Matrimid polymer blends by a combined VIPS/LIPS process. The cast film was exposed to 55% RH for 30 sec before final immersion in a non-solvent bath. They showed that the interaction between the polymer blend and the DMF was higher than that with the NMP. Hence, DMF solutions were less stable, and accordingly, developed asymmetric final membrane structure. On the other hand, polymer blend with 20% to 60% Matrimid shifted the phase inversion process to a further delayed demixing as the viscosity increased. Subsequently, macrovoid formation was inhibited and membranes with skin layer and sponge-like cross section were achievable [88].

Another solvent factor that influences the process kinetics is solvent viscosity. Tsai et al. noticed that the bi-continuous structure was transformed to the less interconnected cellular structure when the solvent was changed from 2P to NMP. They explained that the viscosity of 2P (13 mPa.s) compared to NMP (1-2 mPa.s) was the reason for this drastic transformation. The increased viscosity slowed down the polymer-rich phase coalescence and facilitated the polymer gelling [89].

C. Hydrophilic additives

The general aim of additives is to enhance the final membrane hydrophilicity, porosity, mechanical stability and morphology. There are many types of additives, including: polymers (hydrophilic or amphiphilic), inorganic nanoparticles or non-solvents. They increase solution viscosity and slow down the process kinetics.

PVP, PEG and Pluronic® are among the most widely used hydrophilic additives. Kang et al. studied the effect of PVP addition on membrane surface morphology. They revealed that increasing PVP content accelerated water uptake from humid air, which resulted in larger surface pore sizes [90]. Han and coworkers used PVP from 5 to 20 wt%. They illustrated that at low PVP concentration, PVP hydrophilic effect of increasing water absorption overshadowed its viscosity hindrance. In contrast, high PVP concentration delayed phase separation due to the increased viscosity. The solution stayed at the thermodynamic homogenous region during exposure to non-solvent vapor. Subsequently, it resulted in asymmetric finger-like membrane morphology upon instantaneous demixing in a non-solvent water bath [91].

Pluronic® (Plu) is an amphiphilic triblock copolymer composed of hydrophilic poly(ethylene oxide) (PEO) and hydrophobic poly(propylene oxide) (PPO) blocks which is often used as a hydrophilic additive. Wang et al. synthesized Plu and demonstrated its excellent impact on membrane flux recovery and fouling resistance, with long term performance [92]. The stability arises from its entanglement with the PES due to the presence of PPG hydrophobic blocks. Furthermore, Susanto et al. examined membrane stability using similar molar masses of PEG, PVP and Plu. They tested the addition of 10 wt% of each in a PES/NMP cast solution. Results showed that membranes with Plu had the highest hydraulic permeability with comparable dextrane rejection. Although PES-PEG membranes were the most hydrophilic, PES-Plu membranes retained higher fouling resistance due to Plu higher stability in membrane matrix [93]. Further to that, their later work showed that increasing Plu content had a synergistic effect with the non-solvent content to boost the hydraulic permeability. It was suggested that the effect of increased viscosity was the dominating factor for allowing more time for NG to take place. They also showed that with Plu® F127, the maximum allowable TEG content to make a homogenous solution was 25wt%. Beyond this concentration, the incompatibility between TEG and the high PEG fraction of Plu led to dissolution problems. However, when they switched to Plu® PE6400, they could increase TEG content to 60 wt% with 5 wt% Plu [94].

The PES/Plu membranes were reported in many applications including oil/water emulsion separation [95], pervaporation [96] and microfiltration [94] with peak performances. Yet, blending with hydrophilic polymers changes the casting solution viscosity, and impacts the final membrane morphology and pore structure [97]. Moreover, hydrophilic membranes have a tendency to swell in aqueous solutions, which leads to an increase in pore size, loss of selectivity and a decrease in mechanical strength [98]. In this regard, polymer blending

would require a control of pore size and cross sectional structure for the membrane to maintain its selectivity, high flux and mechanical strength.

A solution composition close to the binodal boundary results in more porous membranes as longer time is available for NG [99,100]. The addition of a hydrophilic additive thermodynamically brings the solution closer to this boundary, and kinetically modulates the solvent and non-solvent diffusion through hydrophilicity or viscosity changes. The increase of the hydrophilicity or the decrease in the solution stability result in more sponge-like membrane skeletons with high molecular weight additives such as polyvinylpyrrolidone (PVP) and polyethylene glycol (PEG). The effect of high molecular weight additives on solution hydrophilicity was supported by results of Boom et al. who reported the elimination of macrovoids with PVP addition to the cast solution [101]. Additionally, Torrestiana et al. who validated that increasing either PVP, PEG or water content, increased permeability of UF PES membranes [102]. Similar behavior was observed by Qusay et al. [103] and Chakrabarty et al. [104]. On the other hand, other researchers attributed their results to the degree of delayed demixing based on the increase in solution viscosity. Kim et al. observed that increasing the PEG content or molecular weight tended to form membranes with larger pores. Thus, more viscous solutions would require more time before complete coagulation, thus leading to larger pore sizes [99]. Ohya et al. examined the addition of PEG with various molecular weights to a PSF/NMP system. In their work they neglected the NMP evaporation and correlated the induction of phase separation to vapor absorption and the delay onset of phase separation to the hindrance of absorption due to the increased viscosity. They found that with the addition of PEG 150 Kda the membrane had a smooth lattice structure which they attributed to the PSF/PEG demixing after complete saturation of polymer-lean phase [105].

To get more insight on the contradicting effects of hydrophilic additives, Ma et al. proposed a model to relate non-solvent in-diffusion speed with final membrane morphology. They used inorganic salts with various concentrations to increase solution hydrophilicity. The non-solvent in-diffusion speed increased with the initial addition of salts, then declined with further addition. This was due to the initial effect of increased hydrophilicity followed by resistance due to increased solution viscosity. The final membrane structure changed from anisotropic to sponge-like and, with high salt concentration, to a particulate structure [106].

Additives might also interfere with the gelation boundary. Venault et al. showed the effect of copolymer addition on the PVDF membrane final structure undergoing a VIPS process. The increase of copolymer concentration from 1 to 4 wt% decreased the nodular size of the PVDF membrane. It should be pointed out that the nodular structure is a result of crystallization-initiation gelling. When the copolymer was added as 5 wt%, the process of gelation shifted to a non-crystallization initiation, forming a bi-continuous membrane structure. This was explained in light of the increase in solution viscosity, which hindered the domain growth and coarsening, leading to the preservation of pore connectivity [107].

Bhatacharjee et al. conducted experiments to evaluate the effect of additives to the PES/NMP/water system. They tested the addition of PVP and PEG. It was found that the stability decreased with the increase of additive molecular weight. Additionally, the increase in additive content increased the solution viscosity and decreased the leaching out of additives from the cast film in the coagulation bath. Additives therefore decreased the thermodynamic stability and hindered the kinetics of the process through increased viscosity. Both factors are counteracting. Although less thermodynamic stability would form a more porous structure as a result of earlier crossing of the metastable region, kinetic hindrance will form denser structures due to delayed demixing. However, they found that with 5 wt% PEG, with molecular weight from 0.4 kDa to 10 kDa, the kinetic hindrance had the dominating influence on the final structure. Yet, thermodynamic instability was more influential with a further increase of the PEG molecular weight. Similar to that was the effect of increasing the additive concentration, hence causing an increase in pore sizes [108].

D. Non-solvent additives

Non-solvent additives affect the final membrane morphology through modulating the phase separation kinetics. Young et al. proposed that the addition of a non-solvent to the cast solution facilitated nucleation. Nuclei formed were believed to slow the liquid-liquid demixing by increasing solution viscosity. These factors resulted in the inhibition of the growth of finger-like structures [109]. Peng et al. studied the effect of increasing the cast solution viscosity through non-solvent addition. They found that increasing the cast solution viscosity retarded macrovoid formation by enhancing polymer chain entanglement and inhibiting non-solvent intrusion and convection [110]. These findings were in agreement with other reported results in the literature [111,112].

With respect to the nature of the non-solvent, Jansen et al. effectively prepared asymmetric membranes with ultrathin skin layer using the LIPS process. Comparing low molar mass highly polar non-solvents (e.g. methanol) to larger and less polar non-solvent (e.g. butanol), they found that the former induced faster coagulation. They concluded that rapid coagulation induced the formation of the ultrathin skin layer [113].

Greenwood et al. prepared skinless PES membranes using triethylene glycol (TEG) in the coagulation bath [114]. On the other hand, Li and coworkers added diethylene glycol (DEG) to the cast solution and successfully prepared highly interconnected porous PES membranes using a combined VIPS/LIPS process [115]. Ulbricht group showed that the TEG content in the cast solution of PES/NMP had a strong positive effect on membrane hydraulic permeability. Increasing the TEG content from 45 to 60 wt% increased the permeability by more than 4 folds. However, this effect was only noticed under a combined VIPS/LIPS process. When the system underwent only LIPS, the increase of TEG content had a negligible effect on permeability. On the other hand, permeability increased consistently with increasing exposure time, yet, the trend leveled-off after one minute of exposure. They referred to the hygroscopic power of TEG as the main cause for the induction of phase

separation through NG. Thus, the further increase in the exposure time allowed more time for growth of nuclei and influenced the membrane permeability [94].

E. Nanoparticles addition

The incorporation of nanoparticles (NPs) in polymeric membrane has been reported. NPs could impart a major enhancement to membrane characteristics and performance, including membrane permeability, mechanical properties, fouling resistance, selectivity, and thermal and chemical stability. A major limiting challenge to nanoparticle incorporation is their dispersion in the cast solution. Metal oxide NPs tend to agglomerate due to high specific surface areas and the surface hydroxyl groups that arise from acidity during NPs synthesis [116]. Surface interactions render the dispersion of nanoparticles with diameter less than 100 nm difficult. Surface interactions stated in the literature include: (a) van der Waal interactions, (b) overlap of electric double layer around the particles, (c) overlap of hydrogen bonded surface-water molecules and (d) overlap of polymer adsorbed on article surface [117]. In addition, factors that affect the probability of aggregation include particles concentration [118] and solution ionic strength [119]. The typical approaches for NPs incorporation are either NPs blending in the cast solution or surface self-assembly by subjecting the membrane to a dipping solution with functionalized NPs [120]. Although the latter is considered a relatively easier process, it increases surface roughness which negatively affects fouling resistance [121]. Li et al. and Luo et al. successfully prepared membranes with self-assembly of crude NPs on PES ultrafiltration membranes, and it showed poor antifouling resistance [122,123].

Among the inorganic NPs used for membrane enhancement, TiO_2 has been the focus of numerous studies due to its availability, stability and photocatalytic activity mitigating fouling [124,125,126,127]. With considerably small quantities, NPs could enhance water permeability, thermal and mechanical resistance, in addition to the privileges of having hydrophilic surface and small achievable particle size (≤ 21 nm) [128]. Furthermore, for water treatment applications, it is considered as an ideal choice due to its oxidation power, photostability and non-toxicity [129].

The general approach for TiO_2 incorporation is by the addition of predetermined amount to the cast solution followed by a combined VIPS/LIPS process. Wu et al. applied surface modification by ɣ-aminopropyl triethoxysilane. Silane acts as a coupling agent which reduces surface free energy and hence increases NPs-matrix interaction, reducing agglomeration. Therefore, they were able to synthesize membranes using 100 µm cast knife without loss in membrane mechanical stability [130]. A similar approach was taken by Yang et al. by using sodium dodecyl sulfate [131].

Teow et al. showed that the incorporation of TiO_2 NPs in a PVDF matrix had a significant enhancement for fouling resistance accompanied by increase in hydraulic permeability. These findings suggested that observed improvements were due to increased membrane hydrophilicity. Yet, excessive addition of TiO_2 caused pore blocking and loss in membrane

performance [132]. Yang et al. studied the addition of surface modified TiO_2 to PS membranes. The hydraulic permeability increased steadily till 2 wt% TiO_2, further addition resulted in a decrease in permeability. The steady increase of permeability was interpreted in terms of the increase of solution viscosity which slowed down the demixing process. As a consequence, membrane cross-section showed a clear shifting from asymmetric to sponge-like structure with a dense top layer [131].

Similar results were presented by Soto et al. They showed that increasing TiO_2 concentration created more open and porous structure using a VIPS/LIPS process. They incorporated TiO_2 NPs in a PES/DMF system. In a concentration range from zero to 0.4 wt%, the highest permeability, hydrophilicity and fouling resistance was achieved at 0.2 wt%. Further addition induced aggregation and declined membrane performance. They showed that by the addition of ethanol to the solution, the dielectric constant of the solvent mixture decreased and hence particles aggregation was provoked. Increasing the NPs or ethanol concentration switched the structure from sponge-like to finger-like due to the increased rates of solvent/non-solvent demixing and affinity of system to water [133].

Similarly in earlier works by Mulder's [134] and Kim's [135] groups, it was found that the inter-diffusion speeds increased with increasing NPs content. They explained this by two factors. The first was the increased affinity of NPs to water leading to enhanced diffusion of water to the cast film. The second factor was the negative influence of the particles on the interaction between polymer and solvent molecules, leading to the facilitation of demixing. These two factors were predominated by the viscosity increase at higher concentration ranges.

In the study conducted by Wu et al., they increased the concentration of functionalized TiO_2 (30 nm in diameter) from 0 to 0.7 wt% in a PES/DMAc/water system with the PES concentration set at 15 wt%. Results showed a peak hydraulic permeability at 0.5 wt% TiO_2. This was due to the increased hydrophilicity due to NPs surface hydroxyl and amino groups. Consequently, membrane fouling performance with Bovine Serum Albumin (BSA) showed a flux decline of 55% with 0.5 wt% NPs compared to 87% decline for the pristine membrane. However, a further increase in NPs amounts led to the formation of aggregates which in turns induced mechanical defects in the membrane matrix. These aggregates caused pore blocking and reduced permeability. Similarly, membrane mechanical properties were negatively affected: the breaking strain and strength increased initially, reaching a peak value with 0.5 wt% TiO_2 followed by a drastic decrease with higher NPs concentrations [136].

Razmjou et al. used silane modified TiO_2 NPs in 2, 4 and 6 wt% in a PES/PVP/DMAc system using a VIPS/LIPS process at 50% RH. Their results showed a superior fouling performance for the 2 wt% composition. Flux recovery after the BSA fouling test rose from 57% to 84%. This was due to the increase in hydrophilicity and the alleviation of surface roughness. They also pinpointed the increase in membrane fouling resistance with NPs concentration beyond

2 wt%, suggesting that particles aggregation, and the resulting increase in surface roughness, was the reason for this loss of performance [137].

With respect to particle size, Cao et al. demonstrated that the smaller the particle size of TiO_2 NPs, the higher was the antifouling effect. According to AFM measurements, membranes with smaller particles had lower surface roughness and smaller mean pore diameters [138].

F. RH degree and exposure time

Considering that water is the most commonly used non-solvent, the non-solvent vapor pressure is often expressed in percentage relative humidity (RH %). The exposure time to RH degree affects the pores interconnectivity and the thermodynamic state reached before final coagulation under LIPS. Thus, exposure time represents a key factor for determining the final membrane morphology. With very short exposure time, membrane is barely affected by the non-solvent vapor and morphology represents merely the influence of the coagulation bath. Generally speaking, long exposure time allows polymer-lean phase coarsening and hence more porous morphology.

Chen et al. tested the effect of the humidity exposure period on membrane morphology. They used polymer blend of cellulose acetate (CA)/polyethyleimine with a combined VIPS/LIPS process under RH of 95% at 50^0C. Observation showed that the highest permeability was achieved at an exposure time of 2 min. They concluded that increasing the exposure to humid air resulted in further polymer-lean coarsening which increased the pore size, yet, polymer-rich phase coalescence decreased pore connectivity and final membrane permeability [139]. Similar observation was reported by Shin et al. using PES with 2-methoxyethanol [140].

Sun et al. investigated the effect of different VIPS parameters on cellulose nitrate membranes in acetone. The increase of RH exposure time initially increased the water flux, but, with the further increase of exposure time beyond 2 minutes, the membrane flux significantly declined. This was explained in terms of the evaporation rate of acetone. At lower RH values (50 to 60 % RH), acetone evaporation was the driving factor for phase separation. Accordingly, increasing the exposure time allowed longer period for polymer-lean growth. On the contrary, at RH ranging from 70 to 90%, vapor absorption was dominating and increasing the exposure time decreased the pore diameter. This is due to the effect of rapid phase separation at high RH values. Beyond a certain period of vapor absorption, further exposure to RH allows the polymer-rich phase to coarsen. Subsequently, pore connectivity and size decreased. Strikingly, the largest pore diameters were recorded when solution was exposed to 70% RH for 1 or 2 minutes. The final pore size decreased with either increasing or decreasing RH values. This is because acetone evaporation and water vapor absorption acted synergistically to increase the polymer-lean nuclei growth at 70% RH [141].

Caquineau et al. studied the effect of RH values on membrane final morphology. They measured the mass variation of the casting solution while it was subjected to various RH conditions. Initially, the total mass of the solution increased due to the inflow of water vapor to the cast film. However, after around 30 minutes at 30% RH, the mass started to decline presenting the simultaneous solvent and water loss from the cast film. Furthermore, increasing RH values decreased the rate of solvent evaporation. They also stated that the uptake of water vapor, driven mainly by the hygroscopicity of the (NMP) solvent, made the system reach the metastable domain where NG was initiated. However, macrovoid formation was inhibited due to the slowness of the non-solvent introduction which made the nucleation rate higher than the growth [142]. They also anticipated that at low values of RH (27%), the composition crossed the binodal boundary twice. The first time was from homogenous state to metastable state due to the imbibing of non-solvent. The second time was due to the diffusion of NMP from the lower layers of the cast film to the top layers driven by the concentration gradient along with the evaporation of non-solvent from the cast film surface, thus resulting in the shift to a homogenous state at the upper layers. Furthermore, the migration of NMP to the upper layers decreased the viscosity. This allowed the nuclei formed at the upper cross-section to grow relatively larger than those at the lower cross-section. It is worth mentioning that during the experiment the air flow rate was 2.5 $Lmin^{-1}$ which was kept constant throughout the experiments and is believed to enhance the evaporation from the cast film surface [142].

Menut et al. measured the mass transfer of the cast film containing NMP in dry and humid environments. Under dry conditions with laminar flow rate of 2.5 $Lmin^{-1}$, the initial NMP concentration declined from 84 wt% to 3.68 wt% in 11 hours at 40 ^{0}C. They divided the mass transfer curve into three domains. In the first domain, the drying conditions rate was the limiting factor. In the second domain, the limitation came from the cast film structure and diffusion of solvent from the inner layers. The third domain was limited by the vitrification of the polymer, and the mass decrease was negligible. On the other hand, when the surrounding environment was humid air, the water inflow dominated the mass transfer. It was observed that the total mass increased by 6.72, 18.88 and 54.08 wt% at RH exposure of 30, 50 and 70%, respectively. It is important to note that this increase in weight reflected the higher water vapor absorption to solvent evaporation [143]. This agrees with the observations of Matsuyama et al. for a PVDF/DMF system. However, the percentage increase in weight was around 5 wt% in the latter case [144]. Thus, the increase of 54 wt% represented in Menut's work was justified by the higher effect of hygroscopicity of NMP to absorb water vapor. Moreover, the mass increase of pure NMP solution under humid air was found similar to that in the polymer solution. This observation verified that a liquid layer of NMP was formed over the cast film and that the mass increased respective to the liquid layer uptake of water vapor regardless of the underlying cast film viscosity. This was later verified by Lee et al. work which showed that vapor absorption was similar in different binary solutions of PSF/NMP [76].

Furthermore, Matsuyama et al. exposed PVDF cast films to 10%, 20% and 40% RH. Their developed model assumed that the system did not reach the binodal boundary when exposed to 10% RH, and thus, the membrane formed was dense. However, the morphology changed to cellular-like and lacy at 20% and 40% RH, respectively. This was due to the increase in vapor absorption with the increase in RH degree and the system crossed the spinodal boundary with 40% RH exposure [144].

On the other hand, Park et al. showed that increasing RH from 70% to 90% decreased pore sizes for a PS/NMP/water system. They proposed that lower RH implied slower phase separation and more time for pore growth [145]. A comparable observation was made by Caquineau et al. for their work with polyetherimide under various RH values. An increase in the number of pores with RH accompanied by a decrease in pore size was observed. They highlighted that at high RH, large amounts of nuclei were created. Afterwards, a rapid increase in solution viscosity took place, and this hindered nuclei growth [142].

Similarly, the CA/acetone system of Atinkaya et al showed a higher rate of pre-precipitation of polymer with the increase of RH degree from 25% RH to 50% RH. The results implied that this RH increase led to a more asymmetric structure with higher porosity and smaller pore sizes. Experiments conducted under forced convection with air blowing over the membrane resulted in a completely dense non-porous structure. They indicated that the forced convection under 40% RH did not induce phase separation. It is worth mentioning that neither the air flow rate nor the direction of the blowing air was mentioned. In addition, the time allowed under forced convection was not stated and the cast film was left in air to precipitate (i.e. VIPS/EIPS process) [146].

Tsia et al. tested the effect of exposure to humid air during the passage of a hollow fiber membrane through the air-gap. It was found that with increasing the air-gap length (i.e. exposure time), the macrovoid formation near the outer surface disappeared, reappeared and disappeared once more. The formation of macrovoids was a result of the instantaneous demixing in the coagulation bath. Yet, when the exposure to humid air increased with increasing the air-gap distance, the cast solution formed a surface gel layer which inhibited macrovoid formation in the immersion precipitation step. Upon further increasing the gap distance, the polymer gel had enough time for relaxation allowing instantaneous demixing to take place in the coagulation bath. Consequently, the macrovoids reappeared. Further increase in the gap distance induced full phase separation before the hollow fiber solution reached the coagulation bath. As the phase separation process in the air-gap was not instantaneous, macrovoid formation was inhibited [147]. As the RH value increased, the distance required to re-suppress macrovoid formation became shorter. In other words, increasing RH resulted in the rapid induction of phase separation in the air gap. Based on the mass variation curves, the calculated fluxes of water intake were 4.4×10^{-7}, 2.5×10^{-6}, and 4.8×10^{-6} $gcm^{-2}s^{-1}$ for relative humidity of 30%, 70%, and 90%, respectively. They also measured the mass exchange by determining the mass variation of the cast solution with

time. It depicted that initially, water vapor uptake dominated the NMP evaporation for the PS/NMP system. They investigated the effect of vapor absorption and concluded that at short exposure time, solvent evaporation could be neglected especially in case of low vapor pressure solvents such as NMP (boiling point 202 ^{0}C). This agrees with other results already reported in the literature [148]. As the exposure time to humid air never exceeded 20 seconds (with the longest air-gap distance), the solvent evaporation influence was neglected [147].

Gao et al. showed that by a combined VIPS/LIPS process the brominated polyphenylene oxide (BPPO)/NMP/water system could successfully produce membranes with optimized high flux and high rejection. At RH of 60%, they tested exposure times from 0.5 to 3 minutes. It was observed that the flux increased consistently with the exposure time. They used ATR-FTIR to monitor the water absorption and the possible solvent evaporation. The ATR-FTIR spectra showed that the longer the exposure to humid air, the higher was the vapor absorbed by the cast film. They also found that as the rate of vapor inflow was higher than solvent outflow, the formation of surface localized high concentration was inhibited. Accordingly, the vapor inflow increased with increasing the exposure time. This in turns allowed nuclei of polymer-lean phase to grow further with longer exposure, resulting in membranes with higher flux values [149]. In addition, increasing the RH increased the membrane hydraulic permeability. As the NMP evaporation rate was higher at lower RH exposures, the evaporation created higher surface concentration of the polymer, which in turn created a dense layer upon immersion precipitation. This dense layer delayed the demixing in the inner structure and resulted in membranes with smaller pores. Using only a VIPS process, they illustrated that the thermodynamic rate limiting step was the slow diffusion of vapor into the cast film. Thus, the concentration profile across the cast film thickness was nearly flat. Therefore, the membrane formed had an isotropic cross section morphology. In case of VIPS, the decrease in the RH (60 to 30%) increased the pore sizes. This was explained by the fact that phase separation proceeded slowly which allowed time for nuclei growth and coalescence.

In 2008, Menut et al. investigated the phenomena of liquid layer formation on the top surface under a VIPS process. The Poly(ether-imide) (PEI)/NMP system was used under controlled humidity condition (0 to 55% RH). Raman spectroscopy was used to evaluate the film thickness and the PEI/NMP ratio. It was found that under dry conditions (0% RH), the thickness decreased steadily with time owing to NMP evaporation. On the contrary, at 50% RH the results showed initial decrease in film thickness, an increase until 1 hour exposure, then further decrease. This reflected three consecutive steps of initial film shrinkage, higher rate of water vapor absorption, then the evaporation of NMP and water, respectively [150]. Furthermore, they found that the surface liquid layer was formed only after the film started to contract. The high mass ratio of NMP/PEI at the surface liquid layer was the reason for this observation. Such film shrinkage took place only when phase separation was initiated. For instance, at 50% RH, as phase separation started after approximately 4 minutes, no

obvious shrinkage or surface liquid layer was observed before this period of time. The water accumulated on the surface started to attract NMP from the bulk through percolation. As the surface layer was diluted, it caused a delayed gelation of surface polymer and enabled the formation of closed cells, and hence, a skin layer was formed [150].

Bouyer et al. experiments showed a decrease in pore size with increasing the PEI/NMP ratio for a system undergoing VIPS process. Their experiments showed that the decrease of RH from 75% to 43% had a significant influence on the pore size near the solution-air interface. The phase separation onset for their system was at 5 wt% water concentration in the cast solution. Thus, at 75% RH, the system started the phase separation much faster and resulted in a low polymer concentration profile near the air interface. On the contrary, at 43% RH, the thermodynamic equilibrium between vapor absorption and solvent evaporation was reached at water concentration of 4 wt% (after 350 seconds at 40^0C). In other words, the system reached equilibrium between air and cast film before phase separation was induced [151]. The driving force for water absorption was strongly reduced at the state of equilibrium, and solvent evaporation predominated. As the NMP started to evaporate, the polymer concentration near the interface increased resulting in smaller pores near the top surface. They postulated that if the mass transfer is to be governed by convective air laminar flow, the absorbed water at state of thermodynamic equilibrium would start to evaporate as long as phase inversion was not initiated. This evaporation would be concomitant to solvent evaporation and based on their respective evaporation rates, the solution might stay in the homogenous region. The minimum RH to induce solvent demixing was 27% RH. Below this value, water absorbed by the system was too low to induce phase separation [151].

G. Effect of Convection

Some of the physically meaningful mechanisms for membrane skin formation were proposed by Pinnau et al. under a combined EIPS/LIPS process. They stated that the formation of ultrathin skin has four main underlying factors, namely:

- The cast solution has to be of a ternary system with the solvent vapor pressure higher than the non-solvent.
- Cast solution composition should be as close to the binodal boundary as possible.
- During the evaporation process and before liquid quenching, the solvent evaporation should be assisted with a convective gas flow across the cast membrane.
- The LIPS step should take place using a strong non-solvent.

They proposed that low convective dry gas speeds would enhance solvent removal at the cast film interface allowing the system composition to reach the metastable region. Higher speeds would move the composition further to the unstable region initiating SD process. As the polymer content in their system was more than 10 vol%, the composition was well

above the critical point. Consequently, the NG process took place through the nucleation of a polymer-lean phase (i.e. non-solvent nuclei) before the system reached the unstable state. Although the NG followed by SD is well known to produce membrane with nodular structure, they ascribed the top skin layer formation to the surface tension exerted by non-solvent nuclei created at NG period [152]. This tension arose from the curvature of the interstitial polymer-lean nuclei which could maximally apply a capillary pressure of 4.1×10^7 dynes/cm^2 based on Young-Laplace equation for complete wetting [153]. The capillary pressure exerted by the non-solvent nuclei is opposed by the polymer-rich phase modulus which is dependent on polymer vol%. The nodules calescence would only take place if the capillary pressure of the interstitial polymer-lean phase exceeded the polymer-rich phase modulus. Upon solvent evaporation, if the composition reached PS concentration of 50 – 70 vol% at the top layer, polymer-rich phase would have a modulus larger than the capillary pressure. As a consequence, nodules coalescence will fail and top layer would have pores with various sizes.

In contrast to the effect of surface tension, Ismail et al. demonstrated that the dramatic increase in top layer polymer vol% might also create a skin layer. They tested the effect of applying forced convection using nitrogen to a cast film with a flow rate of 4 Lmin^{-1}. They found that the forced convection increased the rate of solvent evaporation leading to the migration of more solvent from the inner cast film layers. After a while, a skin layer was formed as the polymer concentration per unit volume of cast film was dramatically increased due to solvent loss. Further to that, the skin layer thickness increased with increasing the residence time under forced convection [154].

Yip et al., comparing systems with various miscibility gaps, illustrated that a PS/NMP/water system had one of the lowest miscibility gaps, which reflected the higher probability for phase inversion to take place at lower polymer concentrations. They also reckoned that for NMP and DMF solvent evaporation were negligible and systems with such solvents would continue to absorb water vapor. The model results showed that phase separation was not likely to occur at a RH < 50%., as the calculations showed an induction time of more than 24 hours [155]. They tested the effect of forced convection with air velocities ranging from 50 to 2000 cm/s. It was seen that increasing the air speed increased the evaporation rate at 98% RH, and hence, the phase separation was induced earlier. Times taken for solution precipitation were 60 seconds and 19 seconds for 50 and 2000 cm/s air speeds, respectively. Furthermore, the high air speed of 2000 cm/s created thinner skin as compared to membranes subjected to lower air speeds. The simulation showed that time elapsed until induction of precipitation was directly proportional to initial film thickness and initial polymer concentration. The increase in polymer concentration caused a decrease in water uptake by the system, which prolonged the time to reach precipitation. In addition, the critical humidity was lower for systems with larger miscibility gaps.

Likewise, Khare et al. showed that the mass transfer could dramatically increase up to 10 folds with humid air blowing across the membrane. They proposed a model to evaluate the mass transfer of water vapor to a cast film made of PES/PVP/NMP/water. They specifically chose PES as it has a high glass transition temperature of ca 220 ^{0}C. Based on an earlier work by Caquineau et al. discussed above, the NMP evaporation under 70% RH became significant only after 3 hrs (NMP vapor pressure is <1 mmHg) [142]. Thus, the influence of NMP evaporation was neglected in the proposed model as the exposure time was limited to a few minutes. They assumed that under quiescent conditions, the mass transfer of vapor was only affected by the degree of vapor diffusion [156].

Khare et al. concentration profiles showed a steep increase of NMP concentration at the cast film-air interface. However, the minimum concentration of NMP was a few µm below the top surface. In contrast, the polymer concentration was at its minimum value at the interface affected by the dilution caused by NMP migration to the top. They systematically increased the mass transfer by circulating air in the humidity chamber. Hence, the Reynolds number and mass-transfer Nusslet numbers increased. Consequently, the cloud point was reached in 1 second when solution of 15 wt% PES was subjected to a mass transfer coefficient of 0.0027 $kgm^{-2}s^{-1}$. They also demonstrated that the amount of water required for the system to reach the cloud point decreased with the increase in PES concentration. As the PVP concentration increased, the top surface dilution was higher because NMP and water have higher affinities to PVP than PES. At low mass transfer rates (low convection force), the cast solution whole cross section reached the cloud point. While at forced convection condition, the top layer reached the cloud point long before any changes took place at the sublayers of the cast film. Accordingly, the bulk morphology would be mainly controlled by the coagulation bath conditions and cast solution viscosity [156].

As a conclusion, the VIPS process is an outstanding technique to tailor and manipulate the membrane morphology. Indeed, the number of process parameters and the influence of each variation is the reason for the great potential of the VIPS process. Albeit this is advantageous, it is complicated to precisely point out the effect of each individual parameter on membrane final morphology when there are multiple interacting variables. More specifically, when VIPS is combined with LIPS, it is still unclear which process dominates the phase separation due to the rapid interactive changes that take place. Thus more work is needed to ameliorate our understanding of this combined process.

2.2 Thin film nanocomposite membranes

When the Loeb-sourirajan membrane was developed, it was generally acknowledged that having a dense-thin skin layer on top of highly porous support is advantageous for separation processes. Afterwards, the concept of interfacial polymerization started back in 1965 when Morgan introduced the viability of polymerization process to take place at the interface between aqueous and organic solutions of monomers [157]. More promising results were demonstrated by Cadotte et al. using modified interfacial polymerization

technique (IP) to optimize polymerization process on the porous substrate [158]. However, market interests in the typical asymmetric membrane was still high, as it is fabricated in a one step process and could better withstand high chlorine content feed solutions [159]. TFC membranes key feature that make them competitive to asymmetric desalination membranes is that each layer could be tailored independently from the other. Membranes with high salt removal, high hydraulic permeability, mechanical strength and compression resistance could be fabricated based on application requirements.

Optimization for the active layer includes selectivity, chlorine and fouling resistance. On the other hand, the support layer plays a major role in solution flow resistance and compression resistance. Nevertheless, more efforts have been devoted for the polyamide active layer development as compared to the support layer. Recently, increased attention occurred to the effect of sub-layer on the overall process.

2.2.1 Influence of support layer morphology

The support layer notably affects the hydraulic permeability of TFC membranes. The water withdrawal to the membrane matrix increases with the support layer hydrophilicity, and thus, the overall membrane flux increases. Yet, with too high hydrophilicity, the PA layer attachment to the substrate is weakened. The most common polymer used for support membrane is PES. The feasibility of modulating the pore size of PES membranes renders these an attractive option for TFC support [160]. The support layer structure must compromise between having pore sizes large enough to avoid additional resistance to water flow and small enough to allow a smooth gradient in pore diameter from the selective skin to the support layer inner structure.

Additionally, the support layer has a large contribution to fouling resistance, firstly, through the support layer surface properties which affect roughness and PA layer thickness, and secondly, with the possible clogging of the support layer inner pores when accessed by small foulants that escape the top active layer. Both implications have a high relevance to fouling reversibility and resistance [161]. Furthermore, isotropic support layers add depth filtration properties to the TFC.

To improve solute selectivity, researchers tried to increase the active layer stability and integrity by modifying the support membrane. One approach used by Oh et al. was to fabricate the polyamide layer on the polyacrylonitrate using NaOH that created ionic bonds between the two layers, hence increasing stability [162]. Singh et al., on the other hand, studied the influence of the support pore sizes on PA stability [163]. They found that the membrane with smaller pore diameters was more efficient in rejecting solutes. They attributed their findings to the increase in the active layer thickness with the decrease in pore sizes due to the lower penetration of the PA layer into the substrate.

Gosh and his coworkers comprehensively studied the influence of supports with different pore sizes (30 to 70 nm), different degree of hydrophilicity and surface roughness on the

formed PA layer [164]. Based on the proposed mechanism of PA layer formation, both permeability and surface roughness increased with support layer pore diameters for hydrophilic membranes. Conversely, for hydrophobic membrane supports, the small pore diameter was almost impermeable. Still, the increase in pore diameter of the support layer allowed the enhancement of permeability of the TFC. TFC membranes made with hydrophobic supports had intermediate surface roughness.

Other researchers improved the support membrane's performance through additives. Fathizadah et al. used PVP and PEG with PES membranes to increase hydrophilicity [165]. In this respect, the additives introduced hydroxyl and ether groups, which allowed additional hydrogen bonding with the PA. This in turns increased the PA layer stability and integrity. Another approach was undertaken by Pendergast et al. where zeolite-A was added to both layers [166]. Their results showed enhancement of solute rejection and permeability. Zeolite composite support also showed minimal flux reduction after compaction, as compared to pristine PSF support. Furthermore, Cho et al. used carboxilated PSF to increase polymer intrinsic wettability [167]. Similarly, Wang et al. used PES blended with sulfonated PSF that successfully increased overall flux [168].

Han et al. tested the addition of sulfonated poly (ether ketone) (SPEK) to PSF cast solution to prepare more hydrophilic and sponge-like supports [169]. Their results demonstrated that the sponge-like morphology increased the membrane mechanical strength. They tested the mechanical strength with respect to elongation at break of the membrane. The increased SPEK content increased the overall TFC membrane flux due to increased support membrane hydrophilicity.

Chung et al. compared a commercial isotropic PVDF support with anisotropic support of PES blended with sulfonated polysulfone (SPSF) [168]. Their results concluded that the PA layer could not form an intact film on the PVDF substrate with 100 nm pore diameter. This is due to the relatively large pore diameter which could not effectively support the PA. Accordingly, PES/SPSF asymmetric support was more efficient for TFC membrane formation.

Another approach for support layer enhancement is through the addition of inorganic NPs. Sotto et al. showed the effect of TiO_2 NPs addition to PES support membrane at NP concentration up to 0.5 wt% [161]. They illustrated that as the NPs concentration increased, the hydrophilicity and flux increased. This suggested that a possible enhancement strategy for TFNC membranes would be the incorporation of NPs in the support layer.

2.2.2 Synthesis of TFC active layer

The process of IP typically comprises the addition of an aqueous solution of aliphatic or aromatic diamine to an organic solution of reactive acid chloride. The most commonly used monomers for IP are m-phenylenediamine (MPD) and trimesoyl chloride (TMC). This system was found to form the most successful PA for TFC membranes [170]. Many literature reports showed the superiority of TFC membranes based on a MPD/TMC PA layer. However,

the reported performances show significant variations: for instance, permeability ranged from 9.4 L/m.hr [171] to 82 L/m.hr [172] with rejection ranging from 95% [173] to 98.4% [174] to NaCl solution. On the other hand, comparable commercial membranes from Hydranautics [175], General Electric [176] and Dow FilmTec [177] show permeability values of more than 40 LMH and rejections higher than 99.5%.

Soroush et al. studied the effect of the reaction time and curing temperature on microporous PES supports [178]. They used 2 wt% MPD aqueous solution and 0.1 wt% TMC in n-hexane. They demonstrated that increasing the reaction time from 15 sec to 180 sec, flux and surface roughness consistently decreased, whereas salt rejection increased. A similar effect was shown by Sotto et al. [161].

Zhang et al. investigated the effect of interfacial polymerization method on the final PA film stability. They investigated different parameters including: method of aqueous and organic solution application on support membrane surface, and curing time of the TFC membrane after the process and prior to testing [179]. Membrane clamping in a glass frame was found to be the best method to spare monomer solutions consumption. However, taping the membrane on a glass plate trapped the hexane vapor on the underside of the membrane and resulted in some lateral tension. Thus a uniform PA layer was difficult to form. They also found that 8 minutes curing time was optimal for cross linking and longer curing times initiated the shrinkage of the PA layer leading to layer defects.

Ghosh et al. evaluated the addition of Camphor sulphonic acid (CSA) and triethylamine (TEA) [174]. TEA is known as an acylation catalyst that acts by removing hydrogen halide formed during amide bond formation to avoid possible acid hydrolysis of the amide bond during the curing process [180]. Furthermore, the CSA was used as a wetting agent that increased the amine solution absorption by the support membrane [181]. They compared different organic solvents and found that with n-hexane the TFC formed had the highest permeability, rejection and comparably lowest surface roughness. This was attributed to the combined diffusivity and solubility of the MPD from the aqueous solution to the organic solvent. In the formation of the PA layer, two monomer solutions come in contact together and the polymerization takes place at the interface. However, the amine monomer has to diffuse to the organic solution of the acid chloride as the acid chloride has relatively poor solubility in aqueous solution. Accordingly, the amine monomer concentration in aqueous solution is usually higher than the acid chloride in the organic solution in order to induce partitioning of the amine monomer. The diffusion of the amine monomer to the organic solution is influenced by the organic solvent viscosity, surface tension and amine monomer solubility in the organic solvent. These parameters showed good compromise when n-hexane was the organic solvent and the amine monomer was MPD; therefore, an intact thin PA layer was formed.

Chapter 3

Theoretical Background

Chapter 3 : Theoretical Background

This chapter aims at highlighting the basic principles of the instrumental analytical and characterization techniques used in the conducted research work. Therefore, scanning electron microscopy (SEM), capillary flow porometer (CFP), particle size analyzer, surface charge analyzer and contact angle tool will be briefly discussed.

3.1. Scanning electron microscopy

The scanning electron microscopy (SEM) is one of the most versatile techniques used for imaging of micro and nano features with high resolution. The benefits offered that the SEM holds over light microscopy are based on using a high energy electron beam instead of a light source. Thus, it achieves high resolution relying on the short wavelength of the electric beam. In 1930's, the viability of using the electron beam, positioning the detector and signal amplification was established. Since then, various developments to the instrument have been addressed to achieve higher resolution reaching 1nm by the modern SEM systems [182].

The electron beam targeted at the specimen creates various interactions that generate charged particles and photons. Once the generated species are detected, the out coming signal is amplified to generate an image. The interaction between the primary electrons and specimen undergoes two major processes, either elastic or inelastic scattering. Elastic scattering takes place when primary electron hit an atomic nucleus or outer-shell electron losing negligible energy. As a result, the primary electron is deflected and if the deflection angle is higher than 90^0, the electron is then called a back scattered electron (BSE). On the other hand, the collision might result in a significant energy loss, which is transferred to a sample electron called secondary electron (SE). The SE is then set in motion to either leave the sample or scatter. If the SE comes from an inner orbital, it leaves an electron hole. The electron hole is then filled by an outer orbital electron and the energy difference is released in the form of X-ray or electron ejection (Auger electron) [183].

As different generated electrons have different energies, they have different emission depths. The SE and Auger electrons have relatively low energies and thus small mean-free paths in the sample and typically generated from smaller depths. In addition, the generated particles and photons have different relevance in application, for instance, BSE and SE are used for imaging whereas Auger electrons and X-ray are used to collect information about sample composition.

The depth at which this cascade of interactions take place is dependent on the sample electron density expressed in its atomic number, the beam energy controlled by potential difference across the vacuum column and the incident beam angle. Hence, the interaction depth increases with the increase in beam energy or the decrease in the sample electron density.

As SEs are emitted from a smaller depth, they are very sensitive to the topography of the sample, and hence, most widely used in imaging. The SEs also have a smaller mean free path, therefore generate better resolution images. The ratio between the number of SEs emitted and the incident electrons is known as SE emission coefficient (SEEC). Gold for instance has a SEEC of 0.2 which creates relatively higher number of SEs per incident beam electrons. Thus, it is prefed as a coating material for nonconductive samples. On the other hand, BSEs can give information about the composition and the topography of the sample. Yet, BSEs are preferred in samples with smooth surfaces as some surface features can cause shadowing and the image may then show some artifacts. The BSEs generation is higher with samples of high atomic number. Those samples have highly positive nucleus; accordingly, incident electrons are more likely to bounce back with a large deflection angle [184].

The instrument has a beam column containing electron gun, condenser lenses, objective lens and apertures. The beam column is responsible for beam emission and focusing. The machine also contains sample stage and signal processing system connected to the detectors. The beam column, detectors and sample stage are suited in a vacuum chamber as shown in Figure 3.1.

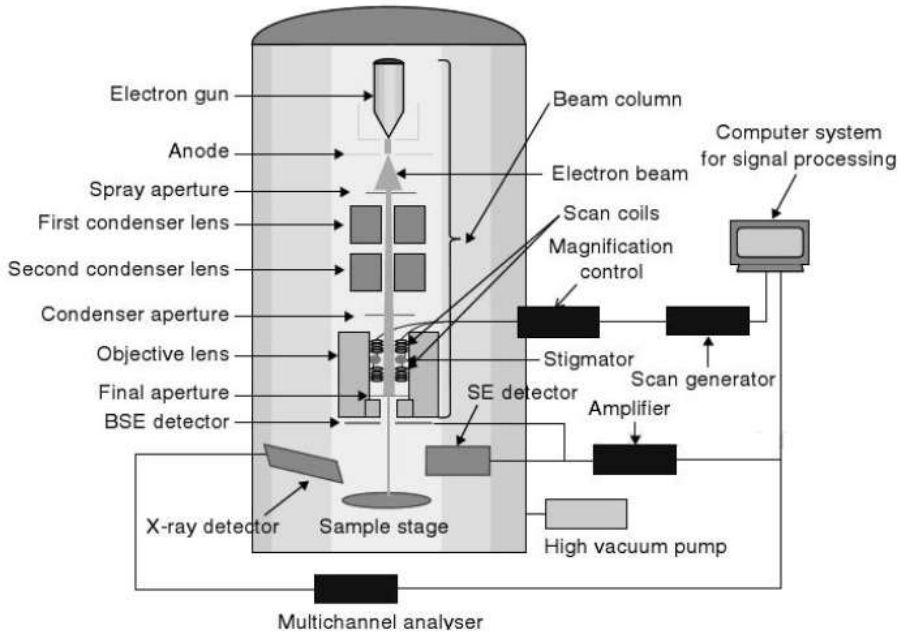

Figure 3.1: Schematic presentation of SEM [184]

There are three main types of electron guns, namely, the thermionic, lanthanum hexaboride (LaB_6) and field emission (FEG). The thermionic generates an electron beam through heating the cathodic filament. On the other hand, with the FEG, electrons are extracted from a tungsten single-crystal tip (radius less than 100 nm) using a strong electric field. Vacuum is required to avoid incident electrons scattering upon interaction with gases atoms. Although, FEG gives better resolution, it requires an ultra-high vacuum to assure that the tip is free of contaminants and oxide [184].

After beam generation, the electron beam passes through electronic lenses to demagnify the beam and focus it on the specimen. Once incident electrons reach the samples it interacts with sample atoms and loses its energy. Afterwards, charge starts to accumulate in the sample if not discharged to a ground. Accordingly, nonconductive samples are usually coated with platinum, gold-palladium or carbon to allow discharging. In this study, samples are polymeric; hence, all samples were sputter-coated to allow better imaging.

3.2. Capillary flow porometer

Capillary flow porometer (CFP) is a technique used to measure an approximation of the pore diameter of porous materials. It depends on the gas flow/liquid displacement method to evaluate the pores structure. The gas flows through the porous sample before and after wetting. The flow rate is determined against an increasing pressure using rotameter. The difference in the flow rate before and after wetting stands for the resistance of the wetting solution to the pressure applied. This resistance decreases as the pore diameter increases. Accordingly, the software calculates the pore diameter from the resistance of dewetting process considering the wetting liquid surface tension. Although, this is a straightforward measurement for cylindrical pores, irregular pores are also expressed in diameter equivalent to a cylindrical pore with similar perimeter to area ratio [185].

A critical element in the CFP technique is the choice of a suitable wetting liquid. The liquid has to possess low surface tension, so as to spontaneously wet the pores. The required pressure for purging the liquid from the pores can be expressed by the following equation:

Equation 3:
$$P = \frac{4\,\gamma(\cos\theta)}{d}$$

where P is the pressure required to displace the liquid, γ is the liquid/solid surface tension, θ is the contact angle and d is the pore diameter.

According to the previous equation, the wetting liquid in the largest pores would be purged at the lowest pressure. However, as the pores are practically tortuous, liquid is only purged when the pressure is high enough to displace it from the most constricted section of the pore structure. Yet, the results are considered satisfactory in water applications; as the most constricted area of the pore structure has the major influence in flow resistance. Thus, regardless of the pore opening at the membrane surface, the results represent the empirical population of each pore diameter (constricted area diameter), which is considered as the average pore diameter for each membrane for a comparative overview.

3.3. Surface charge analyzer

Membrane surface charge originates either from a surface functional group or the adsorption of charged species. Membrane surfaces that lack dissociating functional groups can acquire surface charges based on Stern's theory of preferential ion adsorption. The adsorption creates an electric double layer on the solid surface. Thus, upon the flow of a pressure-driven neutral solution a charge transport takes place by the transfer of the

surface adsorbed ions. Consequently, a current is created which is known as the streaming current. Adsorption of water on the surface takes place competitively with ions adsorption. Accordingly, membranes of higher hydrophilicities are expected to have lower zeta potential [186].

The potential could then be calculated using Helmholtz-Smoluchowski equation:

Equation 4: $$U_{str} = \frac{\epsilon_{rs}\epsilon_0\zeta}{\eta K_L}\Delta P$$

Where, U_{str} is the streaming potential, ϵ_{rs} is the relative permittivity of the liquid, ϵ_0 is the electrical permittivity of vacuum, ζ is the zeta potential, ΔP is the pressure difference, K_L is the specific conductivity of the liquid and η is the liquid dynamic viscosity [187].

The instrument measures the electric field generated by the flow of KCl liquid in a gap with the gap walls comprising the solid sample. The flow pressure is fixed while the current is measured against an increasing PH.

3.4. Particle size analyzer

The basic principle of the particle size analyzer is the dynamic light scattering (DLS) process. When light encounter a particle of a size larger than its wavelength, light scatters from different positions on the particle creating an angular distribution of scattering. On the other hand, if light hits a particle with a size smaller than the incident light wavelength, the particle will act as a point source of scattered light. However, small particles are not stationary in the solution and undergo a random movement known as Brownian motion. This random motion brings about two major influences on the scattered light, which are the change in frequency and phase. Leon Brillouin was the first to predict a pair of shifts in scattered light frequency causing what is known as Brillouin doublets. However, these doublets were hard to experimentally observe due to their small shifts from the main light frequency.

On the contrary, phase changes due to Brownian motion were found to be more reliable. As the particle undergoes small displacements in a liquid, the scattered light from a monochromatic source changes its phase when detected from a fixed position. Although it is difficult to measure the light phase changes, it is relatively easier to record the superposition and interference of the scattered light. These constructive and destructive interferences of the scattered monochromatic light change the intensity which is easily detected and analyzed. Thus, an algorithm called autocorrelation was developed to evaluate the scattered light in a time domain. Using autocorrelation, the degree by which the function changes with time relates to the movement of particles in the solution. This motion is referred to as the diffusion coefficient is dependent on the particle size according to Stokes-Einstein equation as follows [183]:

Equation 5: $$D = \frac{KT}{6\pi\eta R}$$

Where D is the diffusion coefficient, K is the Boltzmann constant, T is the temperature in degree kelvin, R is the particle radius and η is the liquid viscosity.

A DLS apparatus has a laser source, photo detector, sample container and photo correlation electronics as shown Figure 3.2. The laser provides monochromatic light with minimum noise and high coherence wavelength. The detector should be sensitive enough to determine even the slightest scattering of the laser light. On the other hand, if the laser is quite powerful, a filter should be added to avoid detector saturation with the scattered light and would then be able to determine scattering fluctuations. The two main types of laser sources are gas and semiconductor diode lasers. He-Ne gas laser is used for high scattering samples; while for low scattering samples a more powerful laser may be required, such as Argon laser [183].

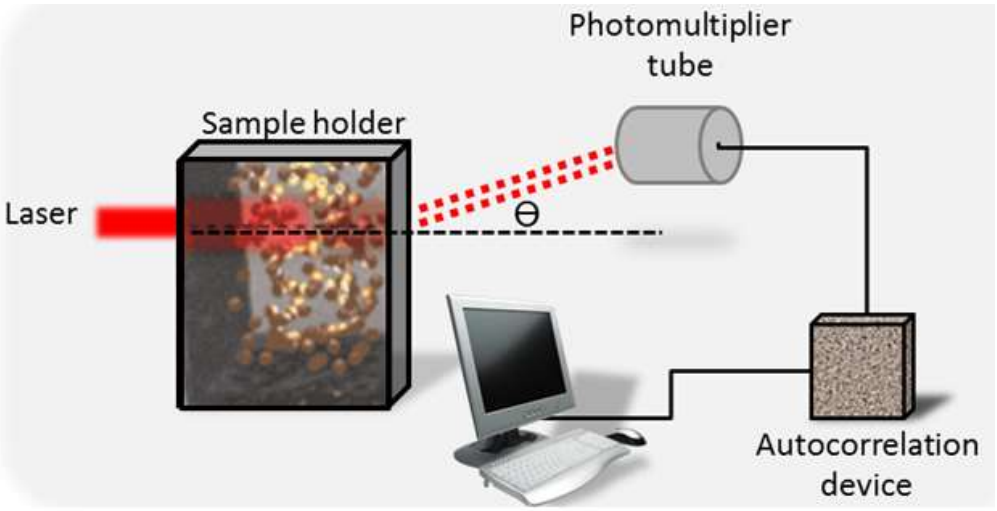

Figure 3.2: Schematic presentation of DLS device

The photodetector is typically a photomultiplier tube. The tube consists of a window to allow photons to enter a vacuum sealed tube and photocathode made of a thin photoelectrical material that generates electrons upon encountering an incident photon. Inside the vacuum tube, the generated electrons are accelerated to dynode which generates secondary electrons multiplying the incident electrons from the photocathode. The process continues hitting consecutive dynodes until the secondary electrons finally reach the anode with amplified signal. Finally, the signals are transmitted to the autocorrelation electronics to process the data [188].

3.5. Contact angle measurement

Membrane interfacial contact angle plays a key role in evaluating the membrane efficiency. It provides valuable information about degree of biocompatibility, coating efficiency for coated membranes, quality of adhesion, and degree of wetting in water applications [189].

Even more, with proper interpretation, the contact angle could drive conclusions about the membrane surface chemistry considering polar and non-polar surface functional groups. Although it is referred to as the simplest approach to evaluate surface free energy, it requires effort to precisely evaluate solid surfaces due to the possible reorientation of surface groups when contacted with a liquid [190].

There are two thermodynamic equilibrium states, namely, complete wetting and partial wetting. Complete wetting occurs when liquid forms a thin layer upon contacting with solid surface (contact angle = 0). On the contrary, the liquid forms a drop shape on the solid surface with partial wetting state (contact angle > 0). The drop shape is generally governed by two contradictory forces which are the interfacial tension and gravity. Interfacial tension tends to make a spherical drop, while gravity acts toward flattening the liquid on the solid surface. The final drop shape could be described by Laplace equation as follows:

Equation 6: $$\Delta P = \gamma \left(\frac{1}{R_1} + \frac{1}{R_2} \right)$$

Where, ΔP is the pressure difference at the interface, γ is the liquid interfacial tension and R_1, R_2 are the two radii of the drop curvature as shown in Figure 3.3.

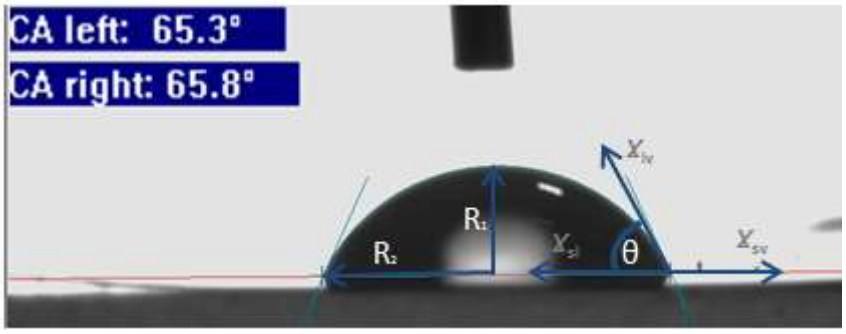

Figure 3.3: Representation of Young's equation for contact angle

However, three interfacial forces interact when a drop is settled on a solid surface corresponding to three interfacial tension expressions; which are, the solid-liquid (γ_{sl}), solid-vapor (γ_{sv}) and liquid-vapor (γ_{lv}) [191]. The equilibrium between the three tensions determines the contact angle (θ_e) using Young's equation [192]:

Equation 7: $$cos\ \theta_e = \frac{\gamma_{sv} - \gamma_{sl}}{\gamma_{lv}}$$

According to Young and Laplace equations, the contact angle determines the degree of wettability of solid surfaces. Thus the instrument uses a straight forward procedure to determine the angle of contact between the drop and the solid surface. Firstly, a precise drop volume is dropped on the solid surface. Then a video camera captures the drop at a microscale. The operator afterwards adjusts the baseline at the interface between the drop and the solid. Consequently, using the ellipse equation, the software proposes an imaginary

circle and calculates the contact angle by drawing tangents to both sides of the drop. The contact angle is the average between the angles at both sides of the drop.

There are two main approaches in determining surface contact angle: the sessile drop and captive bubble. As the contact angle is in principle the outcome of competing interfacial forces between different phases, the difference between the two methods is in the type of droplet phase and the surrounding phase, as shown in Figure 3.4. In the sessile drop method, a liquid droplet is settled on the surface where the surrounding is typically air. On the other hand, the captive bubble method uses air droplet subjected to the surface which is submerged in a liquid.

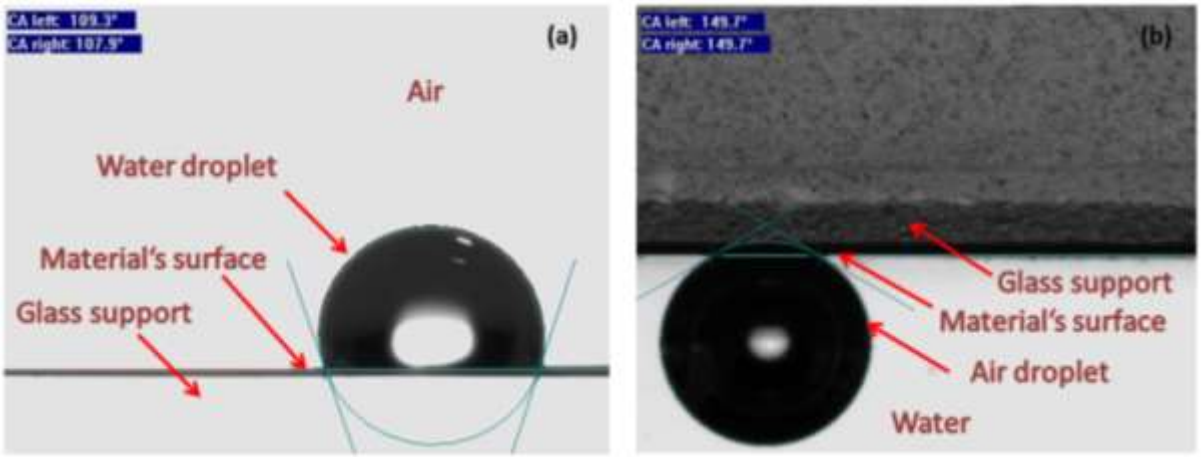

Figure 3.4: Images showing the adjusted baseline, imaginary circle and the tangents drawn to calculate the contact angle using sessile drop method (a) and captive bubble method (b)

Chapter 4

Materials and Methods

Chapter 4 : Materials and Methods

4.1. Materials and supplies

PES powder (Ultrason® E 6020 p) purchased from BASF (Germany) was dried at 70°C for 6 hours prior to use. N-methyl-2-pyrrolidone (NMP) purchased from Merck (Darmstadt, Germany) was used as solvent while the non-solvent was Triethylene glycol (TEG) purchased from Arcos (Geel, Belgium). The pore forming hydrophilic additive Pluronic® PE6400 (MW∼2900 g/mol) was obtained from BASF (Ludwigshafen, Germany). Nitrogen gas purchased from Messer Griesheim GmbH (Krefeld, Germany) was of ultrahigh purity. Filtration tests were conducted using latex beads polystyrene (LB3) with mean particle size of 300 nm purchased from Sigma–Aldrich. Materials for nanoparticles (NPs) surface modification purchased from Sigma-Aldrich were ϒ-aminopropyl triethoxysilane (purity ≥98%) and absolute ethanol (purity ≥99.8%). Titanium dioxide (TiO_2) powder purchased from Sigma-Aldrich with a mean particle size of ≤ 25 nm.

Chemicals for polyamide formation included N,N-Diethylethanamine (TEA) purchased from Merck-Millipore (purity ≥99%), and D(+)-10-Camphorsulfonic acid (purity ≥99%), m-Phenylenediamine (purity ≥99%) and 1,3,5-Benzenetricarboxylic acid chloride (purity ≥98%) from ACROS Organic, as well as, anhydrous hexane (purity ≥95%) from Sigma-Aldrich.

4.2. Membrane fabrication

The work was conducted at Prof. Mathias Ulbricht laboratories in the department of Technical Chemistry, Universität Duisburg-Essen, Germany. Other experiments took place at Prof. Ramadan's laboratory in the department of chemistry, The American University in Cairo and Ass. Prof. Khalil's laboratory in the department of physics at Fayoum university.

4.2.1. Equipment used:

Deionized water used throughout the study was generated from Milli-Q system from Millipore (Burlington, MA, USA). An ultrasonic homogenizer for NPs dispersion was Sonoplus® HD 3200 (Bandeline, Germany). Flowmeter to measure the air flow rate ALMEMO® 2590 (Ahlborn, Germany). Humidifier used to adjust chamber humidity was Nordmann steam humidifier (model RC4/DC4, Nordmann Engineering AG, Basel, Switzerland). Electro-kinetic analyzer to measure membrane surface charge was SurPASS (Anton Paar GmbH, Austria). Dead-end stirred cells used for permeability measurements were (Amicon cells model 8010, Millipore Corporation). The NMR spectrum obtained at 300MHz with DRX 300 (Bruker) using Spinworks 4© (Version 4.1.0.0, University of Manitoba). SEM micrographs generated from Quanta 400 FEG environmental scanning electron microscope at standard high vacuum conditions after sample sputtering using K 550 sputter coater (Emitech, UK). Capillary Flow Porometer for pore size measurements was CFP-34RTG8A-X-6-L4 (PMI Inc. Ithaca, NY, USA). Contact angle measurements were conducted using OCA 15 Plus from (Dataphysics GmbH, Filderstadt, Germany). Stabisizer®

was the particle size analyzer from Particle Metrix, Germany. The rheometer used was TruGap™ rheometer model Physica MCR 301 (Anton Paar, Germany).

4.2.2. Cast solution preparation

Dope solution was prepared by the sequential addition of solvent/non-solvent at the desired quantities, followed by Plu. After 30 min of mixing on a magnetic stirrer at 200 rpm, PES was added in portions with stirring at 200 rpm till completely dissolved (clear solution). The solution was left to release air bubbles for 3 hours before proceeding with casting.

4.2.3. Nanoparticles addition

To incorporate TiO_2 NPs, at first surface modification was performed to enhance their dispersion in the cast solution. The 3 gm of TiO_2 was added to a solution of 0.1 gm ɣ-aminopropyl triethoxysilane in 100 ml ethanol. The solution was stirred at 200 rpm for 1.5 h at 60 ^{0}C. Afterwards, the solution was centrifuged and powder was washed with distilled water twice and dried at 70 ^{0}C for 2 h. Powder was then added to the cast solution in a mixing flask and dispersed using ultrasonic horn with amplitude of 70% for 10 min using the ultrasonic homogenizer.

Cast solutions of different compositions were prepared as summarized in Table 4.1.

Table 4.1: Cast solutions composition and their respective codes

PES (wt%)	NMP (wt%)	TEG (wt%)	Plu® (wt%)	TiO_2 NPs (wt%)	Solution code
10	30	55	5	-	$P_{10}T_{55}Pl_5$
10	90	-	-	-	$P_{10}T_{90}Pl_0$
10	85	-	5	-	$P_{10}T_0Pl_5$
10	30	60	-	-	$P_{10}T_{60}Pl_0$
11	30	55	4	-	$P_{11}T_{55}Pl_4$
13	30	55	2	-	$P_{13}T_{55}Pl_2$
15	30	55	-	-	$P_{15}T_{55}Pl_0$
15	30	54	1	-	$P_{15}T_{54}Pl_1$
15	30	50	5	-	$P_{15}T_{50}Pl_5$
15	40	45	-	-	$P_{15}T_{45}Pl_0$
15	60	25	-	-	$P_{15}T_{60}Pl_0$
15	30	54.99	-	0.01	$P_{15}T_{54.99}N_{0.01}$
15	30	54.95	-	0.05	$P_{15}T_{54.95}N_{0.05}$
15	30	54.9	-	0.1	$P_{15}T_{54.9}N_{0.1}$
15	30	54.5	-	0.5	$P_{15}T_{54.5}N_{0.5}$
15	30	54	-	1	$P_{15}T_{54}N_1$

4.2.4. Support layer synthesis

Casting was conducted with in-house built equipment, computer-controlled for casting speed which was maintained at 70 mm/sec. A casting knife with 200 µm gap was used for casting the dope solution onto a glass substrate. The casting knife was fixed and the glass plate moved against the knife. This was placed within a closed chamber with computer-controlled humidity conditions. Humidity was adjusted to 30%, 55%, 60% or 80% RH (±3%) under two convection conditions. The convection was controlled by pumping dry air into the humidity chamber. Casting was thus conducted either under free or forced convection referring to the dry-air flow rate in the chamber as listed in Table 4.2.

Table 4.2: Free and Forced convection conditions based on air flow rate

	Average flow rate (m/s)	Volume exchange rate (m^3/h)	Chamber volume exchange rate (cycles/min)
Free convection (C_f)	0.68	1.8	0.97
Forced convection (C_0)	2.62	12	6.45

The flow rate was measured using the flowmeter which was connected to a probe that ends with a small fan. The fan was subjected for 2 minutes to the vapor outlets of the chamber shown in Figure 4.1 to obtain the average flow rate. The outlets have a total area of 145 cm^2 and the fan diameter was 7 cm. Thus, volume exchange rate was calculated as the total air volume escaping the chamber per hour. Subsequently, we calculated the number of air cycles where the total chamber volume was exchanged per minute.

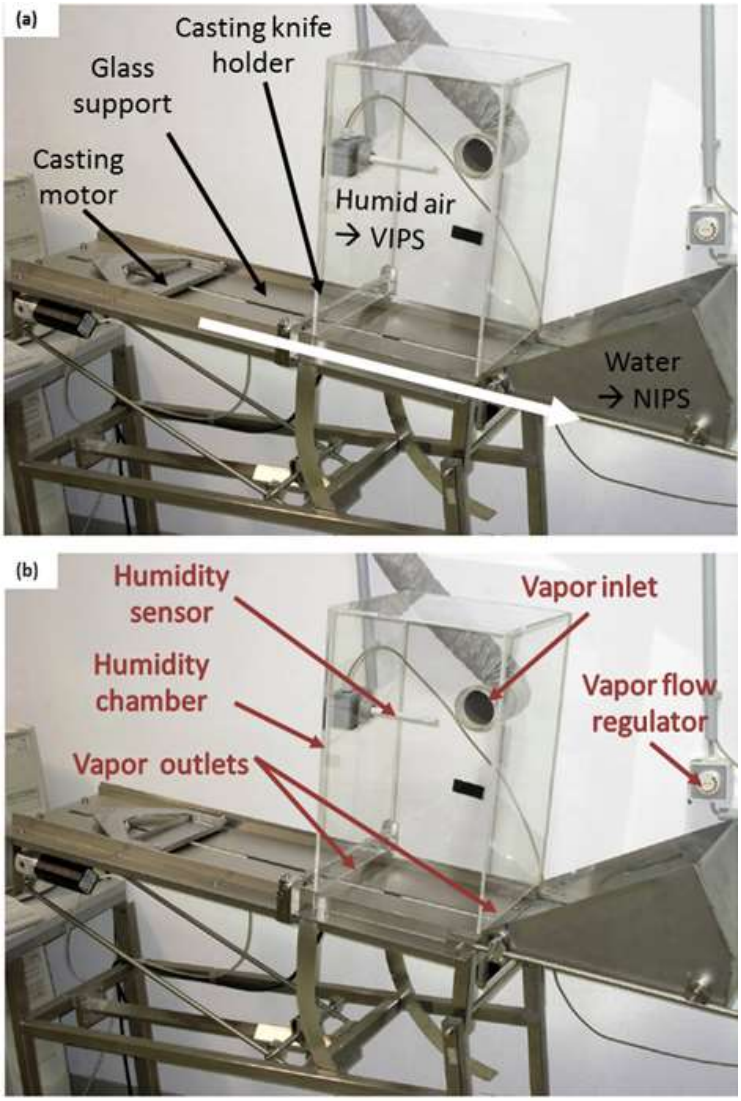

Figure 4.1: Casting tool with arrows showing the casting process (a) and vapor controlling system (b)

After the determined exposure time, the nascent membrane is drawn to the non-solvent water bath kept at room temperature for final precipitation. After 1 hour, membranes were transferred to another water bath at room temperature and stored overnight in a new water bath to ensure washing out of solvent. For testing and characterization, samples were taken from the middle of the formed membrane, and reported data represent the average of at least 5 samples per sheet and at least 3 membrane sheets per data point.

Samples were coded after their respective cast solution and fabrication conditions. Letters (P), (T), (Pl) and (N) stand for PES, TEG, Pluronic and nanoparticles, respectively; and were subscripted with the concentration used in weight percentage. Also, letters (H) and (C) were subscripted with humidity degree and convection conditions, respectively. As the convection conditions were either forced or free, the (C) code was subscripted with (f) for forced or (0) for free convection. Samples are listed in Table 4.3.

Table 4.3: List of cast solutions, fabrication parameters and corresponding membrane codes

Solution code	%RH [a]	Convection condition	Sample code	Exposure time
$P_{10}T_{55}Pl_5$	30	Forced	$P_{10}T_{55}Pl_5$-$H_{30}C_f$	1 and 5 min
	55	Forced	$P_{10}T_{55}Pl_5$-$H_{55}C_f$	3 min
	80	Forced	$P_{10}T_{55}Pl_5$-$H_{80}C_f$	1 and 5 min
$P_{10}T_0Pl_0$	30	Forced	$P_{10}T_0Pl_0$-$H_{30}C_f$	1 and 5 min
	55	Forced	$P_{10}T_0Pl_0$-$H_{55}C_f$	3 min
	80	Forced	$P_{10}T_0Pl_0$-$H_{80}C_f$	5 min
$P_{10}T_0Pl_5$	55	Forced	$P_{10}T_0Pl_5$-$H_{55}C_f$	3 min
$P_{10}T_{60}Pl_0$	30	Forced	$P_{10}T_{60}Pl_0$-$H_{30}C_f$	1 and 5 min
	55	Forced	$P_{10}T_{60}Pl_0$-$H_{55}C_f$	3 min
	80	Forced	$P_{10}T_{60}Pl_0$-$H_{80}C_f$	1 and 5 min
$P_{11}T_{55}Pl_4$	Ambient	Free	$P_{11}T_{55}Pl_4$-$H_{60}C_0$	1 min
	30	Forced	$P_{11}T_{55}Pl_4$-$H_{30}C_f$	1 min
	80	Forced	$P_{11}T_{55}Pl_4$-$H_{80}C_f$	1 min
$P_{13}T_{55}Pl_2$	Ambient	Free	$P_{13}T_{55}Pl_2$-$H_{60}C_0$	1 min
	30	Forced	$P_{13}T_{55}Pl_2$-$H_{30}C_f$	1 min
	80	Forced	$P_{13}T_{55}Pl_2$-$H_{80}C_f$	1 min
$P_{15}T_{55}Pl_0$	Ambient	Free	$P_{15}T_{55}Pl_0$-$H_{60}C_0$	1 min
	30	Free	$P_{15}T_{55}Pl_0$-$H_{30}C_0$	1 min
		Forced	$P_{15}T_{55}Pl_0$-$H_{30}C_f$	1 min
	60	Free	$P_{15}T_{55}Pl_0$-$H_{60}C_0$	1 min
		Forced	$P_{15}T_{55}Pl_0$-$H_{60}C_f$	1 min
	80	Free	$P_{15}T_{55}Pl_0$-$H_{80}C_0$	1 min
		Forced	$P_{15}T_{55}Pl_0$-$H_{80}C_f$	1 min
$P_{15}T_{54}Pl_1$	30	Free	$P_{15}T_{54}Pl_1$-$H_{30}C_0$	1 min
		Forced	$P_{15}T_{54}Pl_1$-$H_{30}C_f$	1 min
	60	Free	$P_{15}T_{54}Pl_1$-$H_{60}C_0$	1 min
		Forced	$P_{15}T_{54}Pl_1$-$H_{60}C_f$	1 min
	80	Free	$P_{15}T_{54}Pl_1$-$H_{80}C_0$	1 min
		Forced	$P_{15}T_{54}Pl_1$-$H_{80}C_f$	1 min
$P_{15}T_{50}Pl_5$	30	Free	$P_{15}T_{50}Pl_5$-$H_{30}C_0$	1 min
		Forced	$P_{15}T_{50}Pl_5$-$H_{30}C_f$	1 min
	60	Free	$P_{15}T_{50}Pl_5$-$H_{60}C_0$	1 min
		Forced	$P_{15}T_{50}Pl_5$-$H_{60}C_f$	1 min
	80	Free	$P_{15}T_{50}Pl_5$-$H_{80}C_0$	1 min
		Forced	$P_{15}T_{50}Pl_5$-$H_{80}C_f$	1 min
$P_{15}T_{45}Pl_0$	30	Free	$P_{15}T_{45}Pl_0$-$H_{30}C_0$	1 min
		Forced	$P_{15}T_{45}Pl_0$-$H_{30}C_f$	1 min
	80	Free	$P_{15}T_{45}Pl_0$-$H_{80}C_0$	1 min
		Forced	$P_{15}T_{45}Pl_0$-$H_{80}C_f$	1 min
$P_{15}T_{60}Pl_0$	30	Free	$P_{15}T_{60}Pl_0$-$H_{30}C_0$	1 min
		Forced	$P_{15}T_{60}Pl_0$-$H_{30}C_f$	1 min
	80	Free	$P_{15}T_{60}Pl_0$-$H_{80}C_0$	1 min

		Forced	$P_{15}T_{60}Pl_0$-$H_{80}C_f$	1 min
$P_{15}T_{54.99}N_{0..01}$	30	Free	$P_{15}T_{54.99}N_{0.01}$-$H_{30}C_0$	20 sec
	80	Forced	$P_{15}T_{54.99}N_{0.01}$-$H_{80}C_f$	1 min
$P_{15}T_{54.95}N_{0.05}$	30	Free	$P_{15}T_{54.95}N_{0.05}$-$H_{30}C_0$	20 sec
$P_{15}T_{54.9}N_{0.1}$	30	Free	$P_{15}T_{54.9}N_{0.1}$-$H_{30}C_0$	1 min and 20 sec
$P_{15}T_{54.5}N_{0.5}$	30	Free	$P_{15}T_{54.5}N_{0.5}$-$H_{30}C_0$	20 sec
$P_{15}T_{54}N_1$	30	Free	$P_{15}T_{54}N_1$-$H_{30}C_0$	1 min and 20 sec

[a] *All values of the percentage relative humidity (RH) are approximated where the system adjusted had a narrow range of (+/- 4%)to stabilize the condition.*

4.2.5. Polyamide active-layer synthesis

The PA layer was prepared using interfacial polymerization (IP) process. Firstly, the membrane was fixed in a home-designed glass frame with paper clips to allow exclusive application of aqueous and organic monomers' solutions to the membrane surface as shown in Figure 4.2. Samples of support membrane were 25 cm in diameter with application area of 23 cm in diameter. Aqueous solution of 2 g MPD, 4 g Camphor sulfonic acid and 2 g Triethanolamine in 100 ml water was poured on the application area and left for 5 minutes. During this period, the aqueous solution and monomers were allowed to diffuse through the top layer of the support membrane to insure that proper quantity of monomer would be available for the IP reaction.

Figure 4.2: Glass frame used for PA application on support membranes

Afterwards, the solution was decanted from the frame and the frame was flipped over for 5 min (lag period). During the lag period the membrane surface starts to dry-up through draining the extra aqueous solution. Following that, the organic solution of 0.1 gm TMC in 100 ml n-Hexane was added to the application area and left for 10 seconds, during which the IP reaction takes place. Then, the extra organic solution was decanted from the application area and the newly formed TFC sample was dried in the oven at 75 ^{0}C for 10 min. It is important to mention that TMC was firstly liquefied using oil bath at 70 ^{0}C for 10 minutes prior to the preparation of the organic solution. This recipe was adapted from earlier work of Elsherbiny et al. [193].

4.3. Characterization

4.3.1. Cast solution viscosity

Cast solution viscosity was measured using a rheometer. The rheometer used was TruGap™ rheometer model Physica MCR 301 (Anton Paar, Germany). The viscosity was determined using conical probe (CP 25-2) 24.98 mm in diameter and angle of 2.002^0 at a shear rate of 125 s^{-1} against an increasing temperature from 20 to 40 ^{0}C.

4.3.2. Particle size analysis

Particle size analysis was done using dynamic light scattering technology (Stabisizer® from Particle Metrix, Germany). The mean particle size of LB3 beads were measured using a solution of 100 ppm concentration in deionized water. On the other hand, TiO_2 NPs were examined using the cast solution containing the TiO_2 after sonication to test the dispersion quality.

4.3.3. Membrane hydrophilicity

Contact angle system was used with the captive bubble module. Membrane samples were flipped over and fixed in a glass water container filled with MilliQ water at room temperature. An air bubble was then injected from a high precision micro syringe with bubble volume of 3 µl. Ellipse equation was used to calculate the contact angle. For each membrane sample at least 6 contact angle values, measured at different surface locations, were averaged.

For evaluating bulk hydrophilicity, wettability tests were done where the time needed for a 5 µl water droplet to disappear was recorded. Once the droplet reaches the membrane surface, the OCA software starts tracking the decrease in contact angle values continuously until the droplet completely diffuses into membrane pores. The contact angles are then drawn against time elapsed, giving an indication for membrane wettability. In order to compare different membrane samples, the decreasing contact angle values were normalized to the initial value and then curves were recreated and shown as wettability curves where curve slope represents a comparative overview of the degree of wettability.

4.3.4. Membrane cross-sectional morphology

Membranes top surface and cross-section images were taken by the SEM. For reducing the charging effect, membranes were sputtered using sputter coater with gold/palladium (0.5 to 1 minute). For the cross-sectional morphology, membranes were broken under liquid nitrogen prior to sputtering to maintain the integral cross-section morphology.

4.3.5. Membrane pore size distribution and porosity

Using a Capillary Flow Porometer, 25 mm of membrane samples were tested for the mean pore size and pore size distribution using the “dry up-wet up” model. This model entails measuring dry air flow at increasing transmembrane pressure (up to 7 bar) before and after membrane pores wetting with 1,1,2,3,3,3-hexafluoropropene (“Galwick”, PMI surface

tension 16 dyne/cm). The mean flow pore diameter data points are the average of at least 3 membrane samples.

Membrane porosity was calculated using the following Equation 8:

Equation 8: $$\varepsilon = 100 - \frac{100\,m}{l.A.\rho_{PES}}$$

Where Ɛ is the membrane porosity (%), *l,* the membrane thickness (m), A, the membrane area (m^2), m, the membrane mass (Kg), and ρ_{PES}, is the polymer density (Kg/m^3). In our study PES was used and ρ_{PES}=1400 Kg/m^3.

4.3.6. Membrane surface charge (streaming potential)

Membrane surface zeta potential was measured using an electro-kinetic analyzer. Two samples (20 mm x 10 mm) from each membrane were fitted with a gap cell set at 100 µm. The samples were rinsed twice using MilliQ water for 480 seconds at 100 mbar pressure. Afterwards, samples were rinsed with 1 mM KCl prior to measurement run. Measurements were conducted using 1 mM KCl, whereas, 0.1 M HCl and 0.1 M NaOH solutions were used to adjust the pH for conductometric titration. The electro-kinetic analyzer used the resultant streaming current to calculate surface zeta potential using Helmholtz–Smoluchowski model. All represented points for membrane surface charge are averaged data of 2 measurements for each membrane.

4.3.7. Membrane composition

The membrane final content of the hydrophilic additive (Pluronic ®) was validated using H^1NMR. A sample of the dried membrane was dissolved in deuterated dimethyl sulfoxide (d-DMSO), and then the NMR spectrum obtained at 300MHz. The content of Plu® was estimated by normalizing the integrated peaks corresponding to the PEG repeating unit (4H) in Plu® to that of the peaks corresponding to PES (8H). As such the mass content of the Plu® could be estimated. Peak integration was carried out using Spinworks 4© (Version 4.1.0.0, University of Manitoba).

4.4. Membrane testing

4.4.1. Hydraulic permeability

Flux measurements were undertaken with a dead-end stirred Amicon cell. A reservoir of 1450 ml was connected to the cell and pressurized by nitrogen gas. Membranes were firstly compacted at 1 bar for 0.5 hour till a stable flux was obtained. The flux was then measured at different pressures from (0.2 bar-1 bar) and the average of 3 measurements for at least 5 samples per membrane sheet was taken as to calculate the permeability value. Deionized water was used for all experiments.

4.4.2. Microfiltration performance

To elucidate the microfiltration performance, runs were conducted under isothermal and isobaric conditions. Membrane samples of 4.15 cm^2 tested surface (25 mm in diameter)

were fitted in the dead-end stirred cell with magnetic stirrer at 400 rpm at 0.2 ± 0.02 bar to minimize the effect of concentration polarization. Initial membrane hydraulic permeability was calculated as the volume of pure water passing through the membrane per unit membrane area, time and transmembrane pressure, expressed in (L/m^2.hr.bar). Polystyrene latex beads were used as a model microfiltration solute reported in literature [194,195,196]. The average bead diameter is 300 nm. Using 100 ppm solution of LB3 beads in deionized water, the permeate was collected for 2 minutes at 5 minutes intervals for calculating the relative flux reduction (RFR) over a total period of one hour. RFR was calculated according to Equation 9.

Equation 9: $$RFR\ \% = 100 - \frac{Ja \times 100}{\mathrm{Jo}}$$

Where J_0 is the initial flux and J_a is the flux after interval of filtration.

Considering the flux recovery, the membrane initial flux was measured at a transmembrane pressure of 0.2±0.01 bar, then; the membrane was allowed to permeate 25 ml of 100 ppm LB3 solution. Afterwards, membrane samples were cleaned externally by immersion in 20 ml of MilliQ water and shaking at 100 rpm for 2 hours. The internal cleaning was conducted by backwashing the membrane with MilliQ water at 1 bar for a period of 10 minutes. Then the water flux was measured as the recovery value. Recovery percentage (R_c %) was calculated using the following equation:

Equation 10: $$Rc\% = 100 - \frac{Ja \times 100}{\mathrm{Jo}}$$

Where J_0 is the initial flux and J_a is the flux after cleaning.

4.4.3. Compaction resistance

Samples of the support membrane were compacted using dead-end stirred amicon cell. The hydraulic permeability was measured at increasing pressure of 0.2, 0.4, 0.8, 1 and 1.2 bar for 2 minutes per each transmembrane pressure to measure the average initial flux (J_0). Then the samples were left at 1.2 bar for 1 hour followed by another hydraulic permeability measurement for 2 min indicating the flow after compaction (J_c). Afterwards, the pressure was released back to 0.2 bar and hydraulic permeability was measured for 2 min period (J_r). Loss due to compaction calculated as the percentage difference between initial flux (J_0) and flux after compaction (J_c). Afterwards, percentage difference between flux after pressure release (J_r) and initial flux (J_0) was the degree of recovery.

4.4.4. TFNC performance

Samples of 23 cm in diameter of TFC samples were tested in a dead-end RO cell of stainless steel. Experiments were run under pressure difference of 15±0.2 bar. First 2 ml of the permeate solution were discarded to avoid dilution effect, followed by collection of 10 ml for flux and rejection measurement. The TFC flux was calculated as per the time taken to collect 10 ml of the permeate solution. The feed solution of 2000 NaCl was used with the

initial conductivity of approximately 3.7 ms/cm. Conductance was then measured using conductometer and the difference between feed and permeate conductance reflected the salt rejection (%). For each flux and rejection data point at least 3 TFC membranes were tested and results were averaged.

Chapter 5

Results and Discussion

Chapter 5 : Results and Discussion

This chapter presents the results for enhancing the support layer of TFNC membranes by controlling the support layer morphology. The targeted morphology ought to have an isotropic cross section with surface pore size small enough to efficiently substitute the conventional support layers in stabilizing the thin active film of PA.

5.1. TFNC support-membrane

In this section the results on the variation of the different fabrication parameters for the VIPS/LIPS process are reported. The effect of each parameter on the properties and features of the support-membrane is reported. Following this, the combined effect of the different parameters for tailoring the support-membrane structure of different cast solution compositions is presented and discussed.

5.1.1. Cast solution composition

Starting with $P_{10}T_0Pl_0$-$H_{55}C_f$ for 3 min exposure, the formed membrane had an asymmetric cross section with hydraulic permeability of approximately 2,268 L/m^2.hr.bar. To achieve an isotropic cross-section membrane, one approach was to add non-solvent to the cast solution. Thus, 60 wt% of TEG were incorporated and the membrane $P_{10}T_{60}Pl_0$-$H_{55}C_f$ showed an isotropic cross-section with an increase in permeability reaching 15,132 L/m^2.hr.bar (as seen in Figure 5.1).

Another approach adopted was the addition of a hydrophilic pore forming additive. When 5 wt% Plu® 6400 was added, the hydraulic permeability of the membrane increased to 39,809 L/m^2.hr.bar for $P_{10}T_0Pl_5$-$H_{55}C_f$ sample that preserved the isotropic cross-section morphology as seen in Figure 5.2. The reason for such an increase in the hydraulic permeability can be explained in light of the thermodynamic behavior of the cast solution. The addition of the non-solvent TEG decreased the solution stability and it was easier for the solution to reach the metastable state when exposed to humidity. Once the solution reached the metastable state, NG process took place. Similar behavior has been reported in the literature where non-solvent addition decreased the solution stability and allowed more time for NG [109,110,111]. On the contrary, when the non-solvent was not included in the cast solution, the water vapor absorbed by the solution during the exposure time of 3 minutes was not enough to induce metastable state. Thus, the solution was still at the homogenous state and was merely influenced by the coagulation bath kinetics. Accordingly, $P_{10}T_0Pl_0$-$H_{55}C_f$ membrane had anisotropic cross-section due to the instantaneous liquid-liquid demixing. The average pore diameters of the asymmetric $P_{10}T_0Pl_0$-$H_{55}C_f$ samples were not determined due to equipment limitations.

On the other hand, the addition of Plu® increased the solution hygroscopicity and the rate of absorbing water vapor from the surroundings [90,91]. This facilitated the induction of metastable state and more water vapor was absorbed as compared to the $P_{10}T_{60}Pl_0$-$H_{55}C_f$. As a consequence, the nuclei grew larger and the membrane with Plu® showed higher permeability. To validate this explanation, the membrane average pore diameter was

analyzed. The $P_{10}T_0Pl_5$-$H_{55}C_f$ samples showed an average pore diameter of 430 (±30) nm compared to 340 (±20) nm for $P_{10}T_{60}Pl_0$-$H_{55}C_f$ samples.

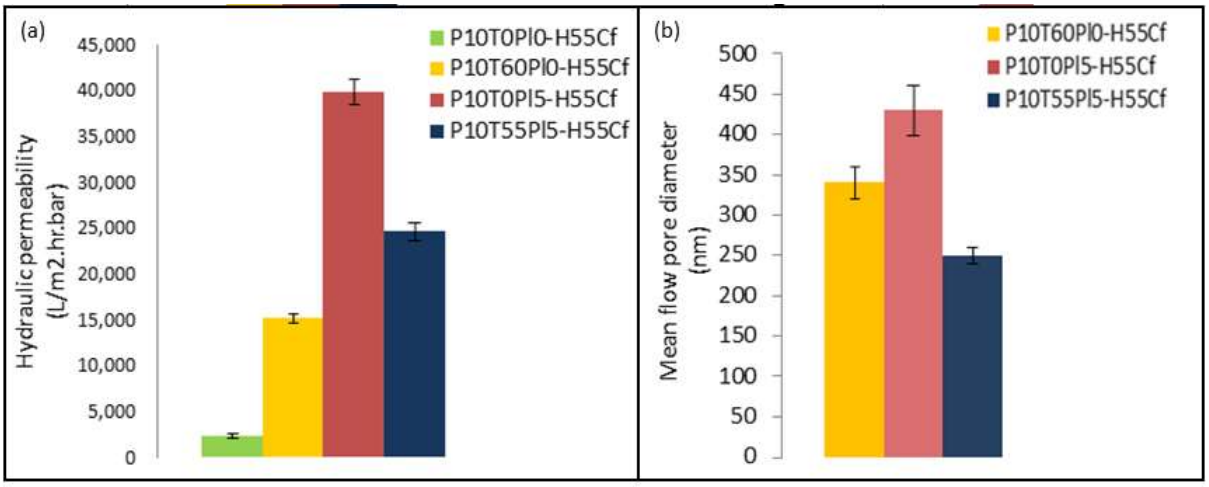

Figure 5.1: Hydraulic permeability of samples with different solution composition (a) and their respective mean flow pore diameter (b)

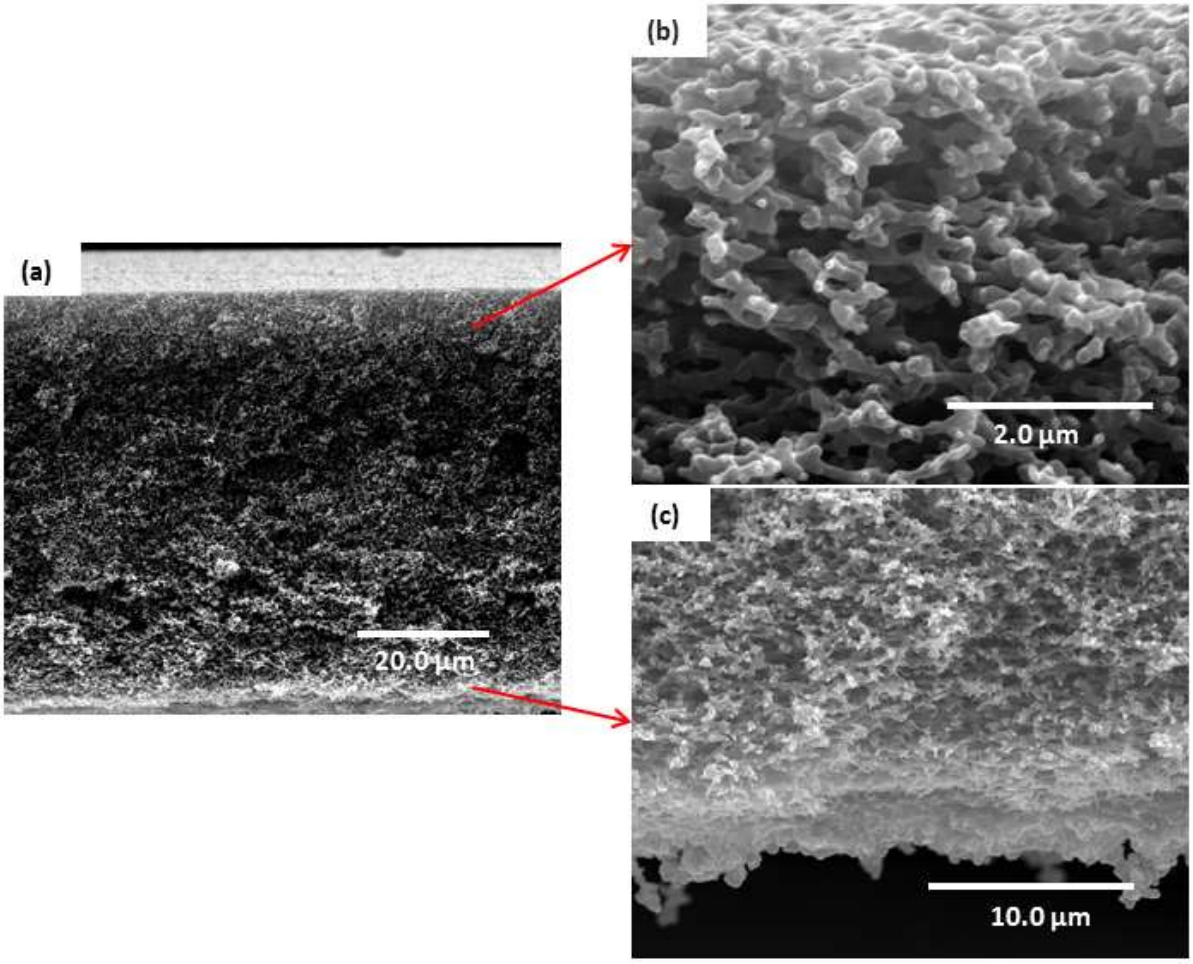

Figure 5.2: SEM micrographs for $P_{10}T_0Pl_5$-$H_{55}C_f$ membrane cross section (a), cross section near the top (b) and cross section near the bottom (c)

The permeability increased in Plu containing samples was due to the increase in the pore diameter and the membrane hydrophilicity. Accordingly, $P_{10}T_{55}Pl_5$ cast solution was prepared and fabricated at the same conditions to test the combined effect of adding non-solvent and hydrophilic additive. The average pore diameter was 250 nm whereas the membrane hydraulic permeability was 24,554 L/m^2.hr.bar, with maintaining the isotropic cross-section. Similar observations were recorded by Susanto et al [94]. The non-solvent addition increased the solution viscosity which hindered nuclei growth [110,111,112]. That explains the reduction in hydraulic permeability compared to the solution $P_{10}T_0Pl_5$-$H_{55}C_f$ as seen in Figure 5.1. The viscosity increase is advantageous in our study as it hinders the rapid shift of solution thermodynamic state and permit better understanding of the effect of other parameters to be studied. Hence, this composition was chosen for further tailoring of membrane features.

A. Polymer content

Polymer content of the cast solution was increased gradually to decrease the membrane average pore diameter in order to create more efficient TFNC support membrane. PES and Plu constituted 15 wt% of the solution. Accordingly, the increase in the polymer concentration was compensated by a decrease in the Plu concentration to maintain the 15 wt%. The polymer concentration was increased from 10 wt% to 11, 13 and 15 wt% along with the reduction of Plu concentration from 5 to 4, 2 and zero wt%. The humidity applied to the system was 30% RH for 1 minute exposure time. As shown in Figure 5.3, the results showed a consistent decrease in hydraulic permeability with correspondence to the decrease in membrane average pore diameter. The solution stability decreased with the increase in the PES concentration which was reported repeatedly in the literature [74, 76]. This should have facilitated the induction of the metastable condition, as the initial composition was closer to the binodal boundary (i.e. less stable). In this case, the earlier induction of the metastable state should result in membranes with larger mean flow pore diameter, because longer time was available for nuclei growth. However, the results here indicate that the increase in solution viscosity resisted vapor absorption and dominated the influence of the decreased stability. In consequence, the increase in PES concentration decreased the polymer-lean nuclei growth. Similar observations to the effect of increased viscosity with polymer concentration have been reported [79,82]. As the solution viscosity increases exponentially with polymer concentration [78], the influence of decreased stability was not significant.

Although Lee et al. results showed no influence of increased polymer concentration on vapor uptake by the solution, the cast solution they tested was PSf/NMP which had relatively lower viscosity than the one tested in our experiment [76]. On the contrary, Sua et al. findings agreed with our observations. They showed that SD took place with 10 wt% PS solution indicating rapid shift of the composition to the unstable state, while 20 wt% solution reached the metastable condition and NG took place. The 20 wt% solution had a higher viscosity which allowed the slow transformation from stable state to metastable

state. Also, they stated that the 20 wt% solution had a wider gap between binodal and spinodal boundaries [78]. In our study, the reason for the dominance of the viscosity effect was the presence of TEG in the solutions prepared. The viscosity increase with non-solvent addition was repeatedly reported in literature [109,110,111,112]. More specifically, TEG addition and its influence on viscosity was also reported [114,115,94]. TEG along with high polymer content acted synergistically to increase viscosity and show its significance. Even more, the presence of higher polymer content per unit volume of the solution offers a straightforward explanation to the inverse relation between polymer concentration and average pore diameter [154].

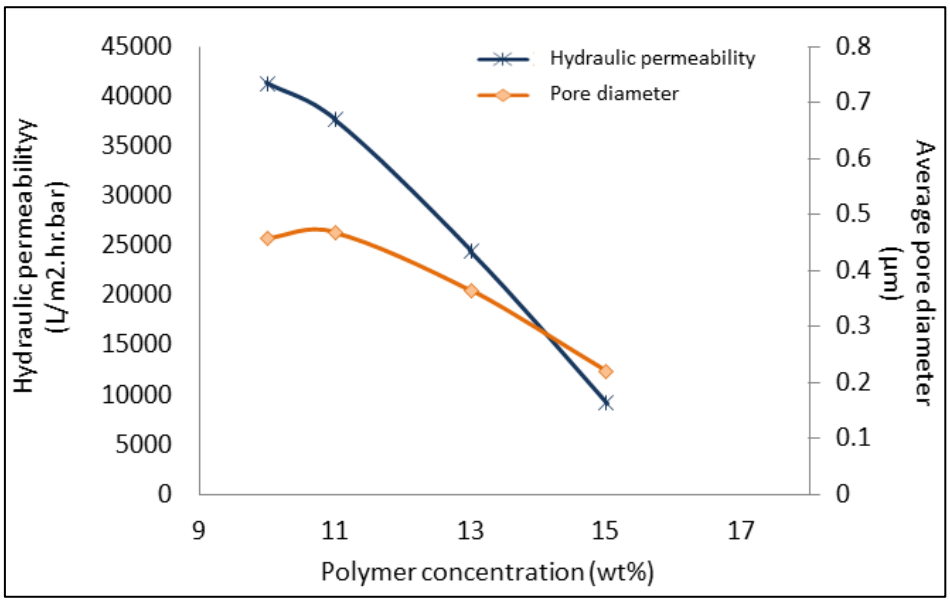

Figure 5.3: Effect of increasing polymer content on the hydraulic permeability and average pore diameter

The relation between the decrease in the pore diameter and permeability loss did not show a linear relationship. In other words, with the decrease in the pore diameter a higher extent of reduction in the hydraulic permeability was observed. Accordingly, to compensate the permeability loss while preserving the small pore diameter, we needed to increase the membrane hydrophilicity.

B. Hydrophilic additive

After successfully decreasing the pore diameter by increasing the polymer content, another approach to improve the membrane quality is to increase its hydrophilicity. The ideal improvement aligned with the purpose of our study is to increase the membrane hydrophilicity while maintaining the relatively small pore diameter which is critical for the membrane to be an efficient TFNC support layer. However, hydrophilic additives typically act as pore formers by increasing the cast solution hygroscopicity. Thus, they increase the water vapor absorption, allowing the polymer-lean nuclei to grow faster when the cast solution reaches the metastable region, leading to a membrane with larger pores.

Results in this study demonstrated that the addition of Plu in 1 wt% to $P_{15}T_{55}Pl_0$ solution increased the hydraulic permeability of $P_{15}T_{54}Pl_1$-$H_{80}C_f$ membrane by 33.8% compared to $P_{15}T_{55}Pl_0$-$H_{80}C_f$. However, the further increase of Plu to 5 wt% in $P_{15}T_{50}Pl_5$-$H_{80}C_f$ showed only a slight increase in the hydraulic permeability by 2.3% as compared to $P_{15}T_{54}Pl_1$-$H_{80}C_f$ membranes. In addition, the pore size distribution showed a slight increase in the average pore diameter from 200 to 219 for $P_{15}T_{54}Pl_1$-$H_{80}C_f$ and $P_{15}T_{50}Pl_5$-$H_{80}C_f$, respectively as shown in Table 5.1.

Table 5.1: Various cast solutions viscosity and their respective membranes hydraulic permeability, mean flow pore diameter and Plu content in the final membrane matrix.

Cast solution	μ (*Pa.S*) at 20 ^{0}C	t_e (min)	% RH (±4%)	J_w ($L/m^2.hr.bar$)	Mean flow pore diameter (*nm*)	Plu/PES (wt%)
$P_{10}T_0Pl_0$	n.d.[a]	1	30	1,705	n.d.	n.d.
		5		5.864	78(±15)	n.d.
$P_{10}T_{60}Pl_0$	n.d.	1	30	40,948	508(±35)	n.d.
		5		31,007	448(±36)	n.d.
		1	80	17,422	235(±13)	n.d.
		5		16,360	202(±18)	n.d.
$P_{10}T_{55}Pl_5$	0.495	1	30	37,782	621(±47)	3.46
		5		31,665	496(±33)	3.85
		1	80	16,065	351(±29)	4.80
		5		15,469	273(±16)	4.65
$P_{13}T_{55}Pl_2$	3.68	1	30	24,454	425(±54)	3.47
		1	80	8,099	181(±12)	3.9
$P_{15}T_{55}Pl_0$	5.53	1	30	10,410	304(±25)	*n.d.*
		1	60	5,958	183(±27)	*n.d.*
		1	80	4,643	130(±14)	*n.d.*
$P_{15}T_{54}Pl_1$	6.33	1	30	4,348	168(±8)	2.70
		1	60	7,512	242(±23)	1.77
		1	80	6,165	200(±20)	1.49
$P_{15}T_{50}Pl_5$	8.60	1	30	5,044	182(±11)	6.83
		1	60	9,628	253(±24)	5.22
		1	80	6,308	219(±13)	6.02
$P_{15}T_{45}Pl_0$	4.13	1	30	1,585	n.d.	*n.d.*
		1	80	2,418	229(±34)	*n.d.*
$P_{15}T_{25}Pl_0$	1.83	1	30	1,754	n.d.	*n.d.*
		1	80	6,761	n.d.	n.d.

[a] *n.d. stands for not determined values.*

This unexpected low contribution of the increased Plu content at 5 wt% can be ascribed to the increased solution viscosity. This viscosity increase counteracted the influence of hygroscopicity enhancement upon Plu addition. Similar contradiction on the effect of polymeric hydrophilic additive incorporation on the kinetic behavior of a cast solution has been reported in the literature. Whereas some researchers reported an increase in the water vapor absorption [90, 101, 102], others have clearly stated that viscosity hindrance to vapor absorption was the dominating effect [94, 105]. Although, both factors have opposing effects on the final pore diameter, it can be seen from the results in Table 5.1 that the dominating factor is concentration dependent. As shown in Figure 5.4, the addition of 1 wt% Plu had a relatively low influence on the solution viscosity in respect to the influence of 5 wt% addition. At room temperature (20 ^{0}C), the viscosity increased by 14.47% and 55.52% for $P_{15}T_{54}Pl_1$ and $P_{15}T_{50}Pl_5$ solutions, respectively. Accordingly, the increased viscosity hindrance to pore growth and significant opposition to the effect of increased hygroscopicity was more prominent in the case of 5 wt% Plu. However, further insight to the thermodynamic influence of the interplaying factors will be comprehensively discussed later in this chapter.

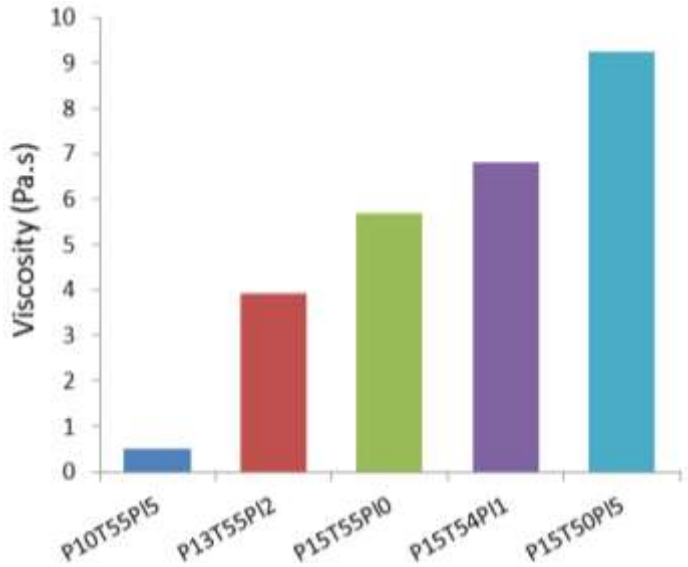

Figure 5.4: Viscosity curves for cast solutions with various composition at room temperature (20 ^{0}C)

5.1.2. Changing fabrication parameters

A. Effect of RH exposure time

Increasing the exposure of a cast solution to water vapor has various effects on the final membrane based on the state of the solution at the end of the short exposure time. For example:

1- If the solution stayed in the homogenous state at the end of the short exposure time, increasing the exposure would allow the solution to cross the binodal

boundary moving into its metastable state; thus, the pore diameter would increase as the NG started to take place.

2- If the solution crossed the binodal boundary at the end of the short exposure, longer exposure will permit longer time to NG process; hence, more nuclei will coalesce to form larger ones. Accordingly, membrane final pore diameter will significantly increase.
3- If the cast solution was close to the spinodal boundary or crossed it by the end of the short time of exposure, the increase in the exposure time would majorly allow the polymer-rich domain undergoing SD to further vitrify and thicken. This thickening would decrease the final membrane pore diameter.

Experiments showed that increasing the exposure time from 1 to 5 minutes increased the hydraulic permeability of $P_{10}T_0Pl_0$-$H_{30}C_f$ membrane from 1705 to 5864 L/m^2.hr.bar as presented in Table 5.1. This agreed with the earlier observation of the asymmetric morphology for $P_{10}T_0Pl_0$-$H_{30}C_f$ exposed for 1 minute, which indicated that the solution did not cross the binodal boundary during the 1 minute exposure period. However, when the period was extended to 5 minutes along with the low viscosity of the solution, the absorbed water vapor induced the metastable condition to the cast film. As a consequence, NG process took place and the cross-section morphology changed from anisotropic to isotropic.

On the contrary, the solutions $P_{10}T_{60}Pl_0$ and $P_{10}T_{55}Pl_5$ are less stable due to higher non-solvent content, thus, showed a decrease in the average pore diameter when exposure to 30% RH was increased from 1 to 5 minutes (see Table 5.1). As mentioned earlier, both solutions under the stated conditions resulted in membranes with isotropic cross-section, indicating that the process of NG took place even at short exposure of one minute. Subsequently, the increase in exposure time shifted the solution composition to the unstable region and as the polymer vitrification started, the polymer domain kept thickening and pore diameter was reduced in comparison to the 1 minute exposure samples.

In the literature, some researchers reported that increasing the RH exposure time increased the pore diameter [139, 149]. However, others demonstrated that the increase in exposure time decreased the pore diameter [141, 145]. This leads us to conclude that the effect of increasing the RH exposure time is dependent on the solution state during the extended exposure as expressed earlier. Generally, increasing the exposure time allows more vapor to be introduced to the solution. This further vapor absorption in our study induced state of instability, and hence, reduced the pore diameter due to polymer-rich phase thickening. This was observed from the decrease in the mean flow pore diameter and hydraulic permeability of $P_{10}T_{60}Pl_0$ and $P_{10}T_{55}Pl_5$ membranes when exposure extended to 5 minutes at either 30% or 80% RH exposure (Table 5.1).

Differently, at 80% RH $P_{10}T_{60}Pl_0$ and $P_{10}T_{55}Pl_5$ solutions did not show significant change when exposure time increased from 1 to 5 minutes. This observation strongly agrees with the

explanation above. As the RH increased to 80%, the kinetics of the process were considerably faster specially as the viscosities of these solutions are relatively low compared to other compositions in this study (as shown in Table 5.1). The process of crossing the metastable region and inducing SD took place at a rate which was high enough to complete precipitation. In consequence, neither the pore diameter nor the hydraulic permeability showed a significant difference for either solutions with an increasing exposure time. In other words, after inducing SD the process kept thickening the polymer domain reaching a point of almost complete polymer precipitation and further increase in the exposure time showed only a minor difference in the average pore diameter.

Similar observation was reported by Chen et al. when membranes were exposed to 95% RH, the increase in exposure time beyond 2 minutes resulted in further polymer-rich phase coarsening. Hence, membrane average pore diameter decreased [139]. Also, Sun et al. reported that the effect of polymer-rich phase thickening took place at high RH values (70% to 90%) [141]. On the contrary, at RH values below 70%, the increase in exposure time increased the final pore diameter. Those reports agree to our explanation that thickening takes place after polymer coagulation when SD is induced. Caquineau et al. proposed another explanation to this phenomenon. They claimed that at high RH values, nucleation is rapidly induced. The high number of nuclei created, caused an increase in cast solution viscosity and hindered the nuclei growth [142].

As aforementioned, the increase in exposure time has a complex influence on the final membrane average pore diameter more specifically with solutions of low viscosity as the solution thermodynamic state shift could be rapid to an extent that the influence of other parameters becomes insignificant. In addition, long exposure times may hide the minor influences of other parameters of interest in our study. Consequently, experiments aimed to study other parameters were all set under 1 minute exposure time. Furthermore, the investigations reported in the following sections were conducted using solutions with relatively higher viscosities (based on solution composition) to facilitate the demonstration of the effects of other parameters on phase separation kinetics.

B. Effect of RH degree

Generally, the increase in vapor concentration increases the chemical potential for the vapor to diffuse to the cast solution based on Nernst-Einstein law of diffusion [197]. It is then expected that the RH degree would change the membrane permeability and pore diameter due to the impacts on the phase separation kinetics. In this respect, a schematic representation in Figure 5.5 shows the main factors affecting the phase separation kinetics. These factors will serve as the key elements explaining the various changes in membrane morphology under different exposure conditions. Additionally, all membrane samples discussed in this section showed an isotropic sponge-like cross-section morphology which indicated that the composition stayed for a period of time in the metastable region.

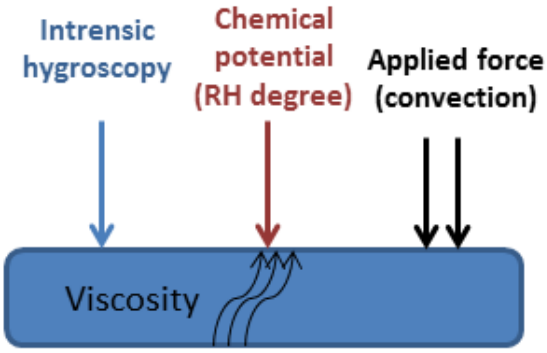

Figure 5.5: Schematic representation of factors affecting VIPS process kinetics

At the early stages of our study, the effect of increasing RH degree was consistent. Samples of $P_{10}T_{60}Pl_0$ and $P_{10}T_{55}Pl_5$ showed a decrease in the hydraulic permeability and the average pore diameter with increasing the RH degree represented in Table 5.1. The hydraulic permeability for membranes of $P_{10}T_{60}Pl_0$ decreased from 40,948 to 17,422 L/m^2.hr.bar with the RH increase from 30% to 80% under 1 minute exposure; respectively. Similarly, $P_{10}T_{55}Pl_5$ samples showed a decrease from 37,782 to 16,065 L/m^2.hr.bar. Both solutions represented a permeability loss of approximately 57.5 %. This loss was attributed to the rapid induction of the unstable state and polymer-rich phase thickening during the SD process.

Likewise, samples with higher PES concentrations of cast solutions $P_{11}T_{55}Pl_4$, $P_{13}T_{55}Pl_2$ and $P_{15}T_{55}Pl_0$ showed a consistent decrease in hydraulic permeability with the RH increase as seen in Figure 5.6. However, the percentage loss in permeability leveled-off. For example the loss in permeability for $P_{11}T_{55}Pl_4$ and $P_{13}T_{55}Pl_2$ membrane samples were 40% and 33%, respectively. These values are lower than the 57.5% loss for $P_{10}T_{60}Pl_0$ and $P_{10}T_{55}Pl_5$ samples as shown in Table 5.1. This is due to the effect of increased viscosity with the moderate increase in polymer concentration that hindered the vapor diffusion to the cast solution. This hindrance affected the rate of inducing the unstable state with the increased RH in the relatively high viscous solutions $P_{11}T_{55}Pl_4$ and $P_{13}T_{55}Pl_2$. Thus, increasing the RH degree from 30% to 80% did not show the same magnitude of permeability loss as compared to the solutions with lower viscosity.

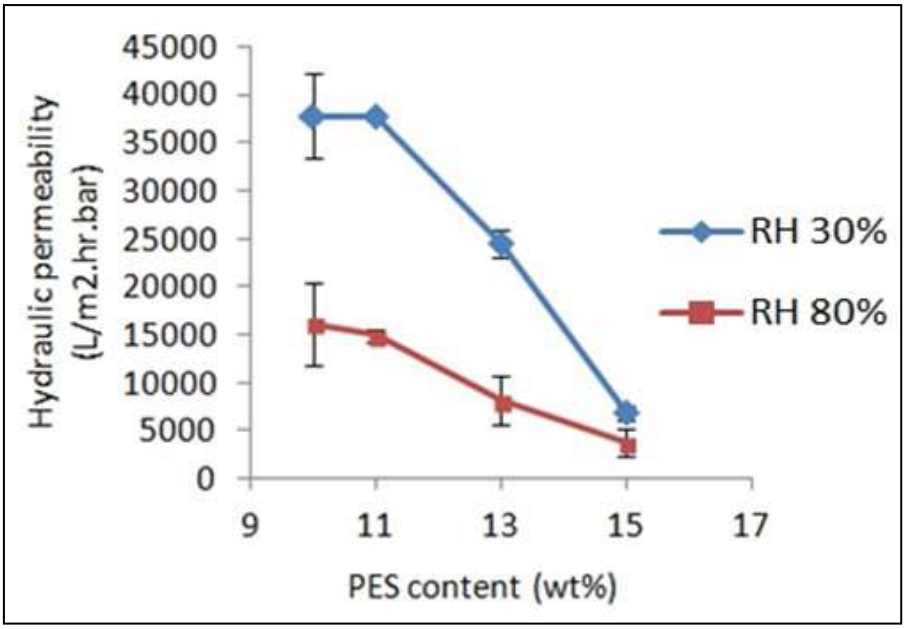

Figure 5.6: Effect of increasing RH degree at 1 minute exposure for solutions of increasing polymer content

On the contrary, the further increase in solution viscosity by increasing PES concentration to 15 wt% ($P_{15}T_{55}Pl_0$ solution) showed higher percentage permeability loss (44%). $P_{15}T_{55}Pl_0$ solution has higher viscosity and less stability compared to $P_{11}T_{55}Pl_4$ and $P_{13}T_{55}Pl_2$ solutions. Although the viscosity barrier hindered the vapor diffusion and was expected to decrease the rate of inducing the unstable state, the solution starting point in the ternary phase diagram was closer to the binodal boundary due to the higher polymer content [74,76]. Consequently, the increase in RH had a more prominent effect on the time spent in the metastable region and unstable state was reached at a shorter exposure period when compared to $P_{11}T_{55}Pl_4$ and $P_{13}T_{55}Pl_2$ solutions. Accordingly, polymer thickening was more extensive in $P_{15}T_{55}Pl_0$ solution and concluded to a higher permeability loss.

As explained before, the addition of Plu to the $P_{15}T_{55}Pl_0$ cast solution increased both the hygroscopic property and the viscosity of the solution. Figure 5.7 shows the effect of increasing RH degree on solutions of increasing Plu content. At 80% RH, the Plu addition at 1 wt% increased the hydraulic permeability but the effect was less significant with further Plu addition. This was ascribed to the dominating influence of viscosity with 5 wt% Plu. To further verify this observation, the solutions $P_{15}T_{54}Pl_1$ and $P_{15}T_{50}Pl_5$ were tested with 60% RH for 1 minute exposure. The permeability increased by 26% for $P_{15}T_{54}Pl_1$-$H_{60}C_f$ and 61.5% for $P_{15}T_{50}Pl_5$-$H_{60}C_f$ as compared to membranes without Plu ($P_{15}T_{55}Pl_0$-$H_{60}C_f$). Likewise were the thermodynamic state shifts for solutions when tested at 80% RH.

In contrast, $P_{15}T_{54}Pl_1$ and $P_{15}T_{50}Pl_5$ solutions behaved differently at 30% RH. At first, $P_{15}T_{54}Pl_1$-$H_{30}C_f$ membrane samples showed a significant reduction in the hydraulic permeability as compared to $P_{15}T_{55}Pl_0$-$H_{30}C_f$ reaching 4,348 L/m^2.hr.bar (see Table 5.1). This reduction is due to the effect of increased viscosity, which hindered the vapor absorption.

The hindrance to vapor absorption prolonged the time taken by the solution to reach the metastable state. Accordingly, the time remaining from the exposure period for NG process was much shorter. However, as stated above, this behavior was nullified when the solution was exposed to 60% or 80% RH. This suggested that at low chemical potential for vapor to diffuse to the cast film (i.e low RH of 30%), the effect of the increased viscosity was more significant. The effect of the vapor chemical potential on the vapor absorption rate has been reported previously [139-150]. Although there is a wide agreement on the increase of absorption rate with the RH value, the influence of this increase on the membrane morphology or pore diameter was not consistent in literature. This is because such influence is highly dependent on the cast solution thermodynamic state and its composition during the higher vapor absorption rate.

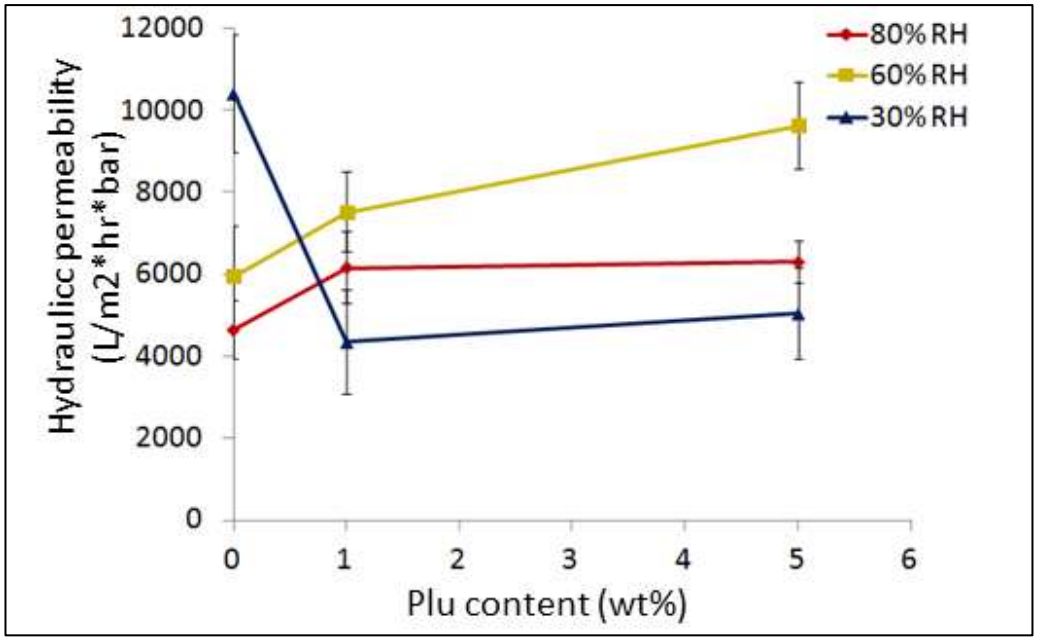

Figure 5.7: Effect of RH degree on cast solutions with increasing Pluronic content at 1 minute exposure time

Furthermore, the addition of more Plu (5 wt%) to the solution moderately increased the permeability for $P_{15}T_{50}Pl_5$-$H_{30}C_f$ compared to the membrane with 1 wt% Plu as shown in Table 5.1. The permeability increase is allegedly due to two factors affecting time permitted for NG process. The first is the decrease in the solution stability when more Plu was incorporated which has been reported in the literature with various polymeric hydrophilic additives [99,100]. The second factor is the increase in solution hygroscopicity with the Plu increase [94]. As the solution with 5 wt% Plu is less stable due to higher polymer content, the initial composition was closer to the binodal boundary. Meanwhile, the increased hygroscopicity of the solution increased the rate of vapor absorption. Both ended up shortening the time required for the induction of metastable state. All represented samples in Figure 5.7 had a fixed exposure time (1 minute) during the VIPS process. Consequently,

the time consumed in the metastable region was longer for $P_{15}T_{50}Pl_5$-$H_{30}C_f$ compared to that of $P_{15}T_{54}Pl_1$ and resulted in membrane with larger pore diameter.

SEM micrographs in Figure 5.8 showed that membranes had sponge-like cross-section. This observation validates our assumption that composition of different solutions entered the metastable region and NG process took place at some point during membrane preparation. The composition bath explained earlier with the contribution of various factors is summarized in Figure 5.9.

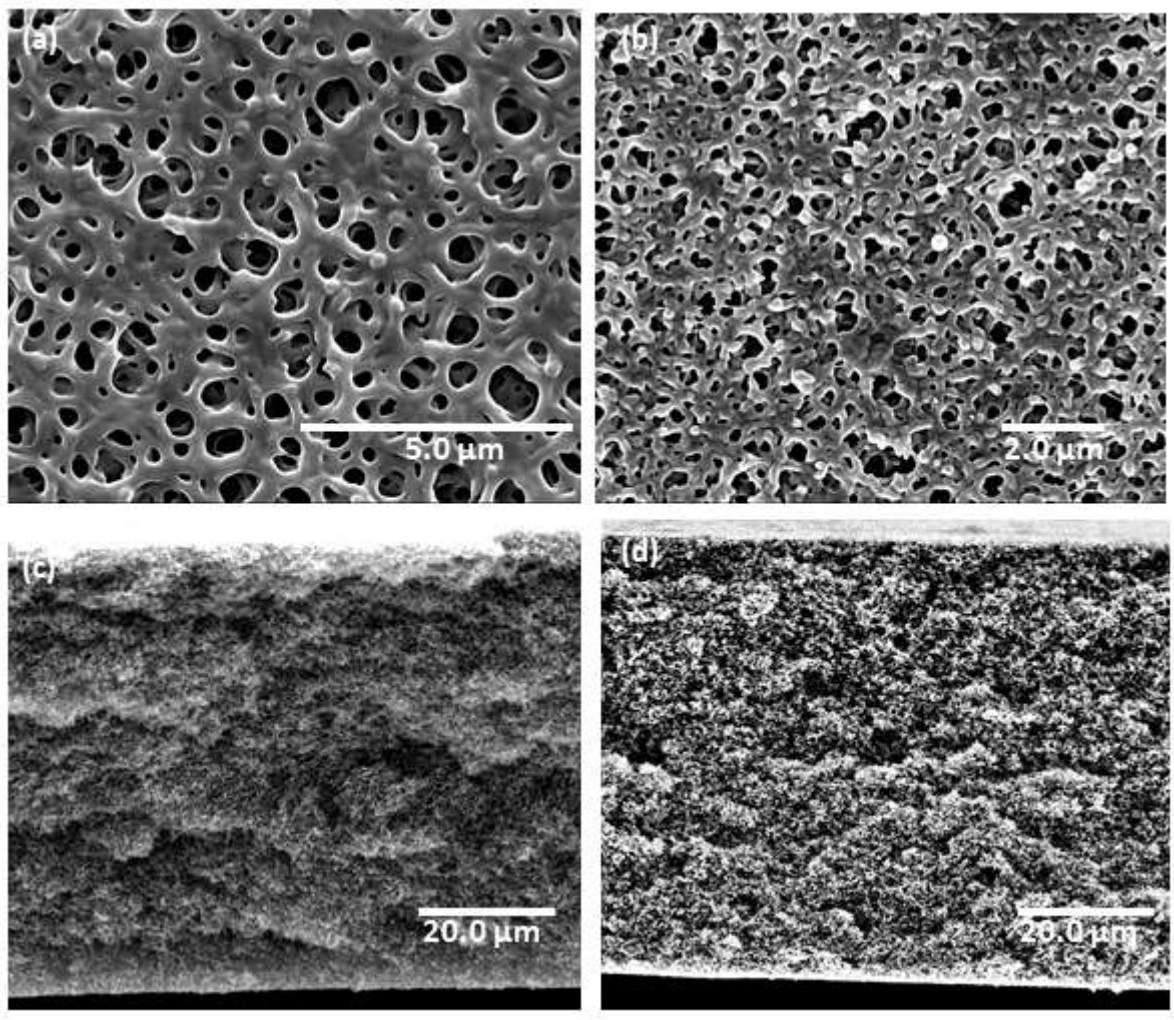

Figure 5.8: SEM micrographs of $P_{15}T_{55}Pl_0$-$H_{30}C_f$ (a, c) and $P_{15}T_{50}Pl_5$-$H_{80}C_f$ (b, d) representing top surface and cross-section, respectively

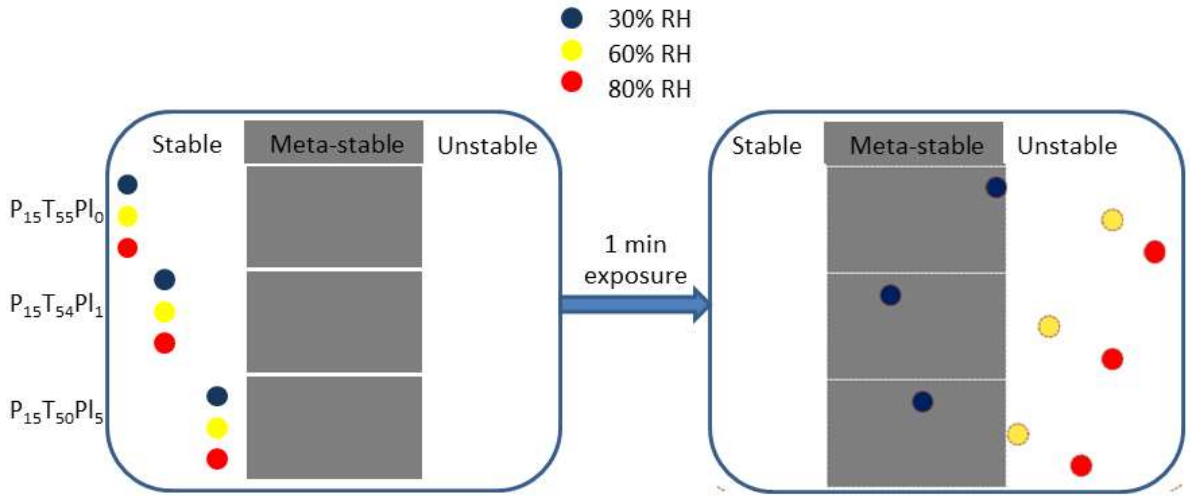

Figure 5.9: Schematic representation to the solutions thermodynamic behavior under forced convection condition

C. Effect of convection

Allowing free convection to preside over the process of non-solvent vapor absorption slowed down the process kinetics. A comparative schematic representation to the solutions thermodynamic behavior under free convection condition is shown in Figure 5.10.

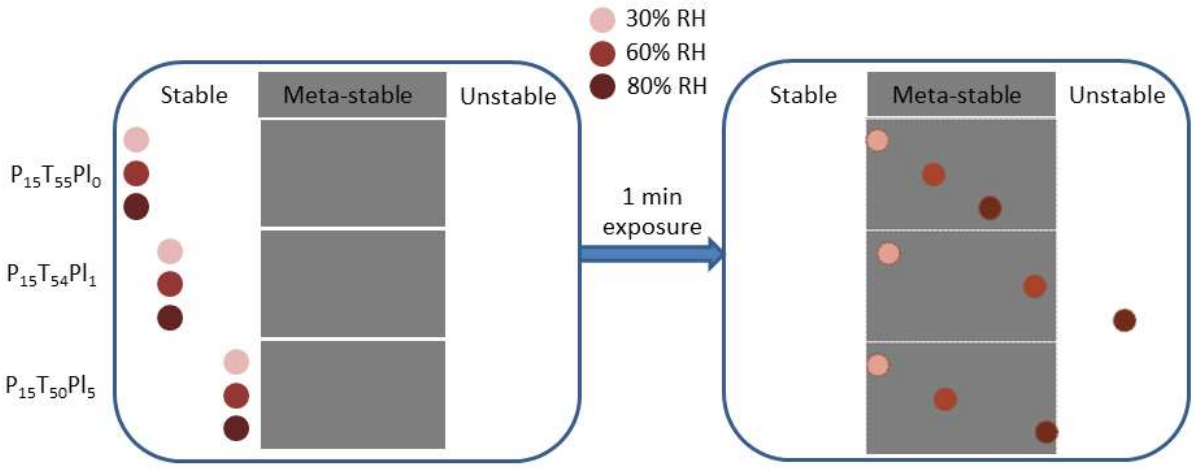

Figure 5.10: Schematic representation to the solutions thermodynamic behavior under free convection condition

As per the results demonstrated in Figure 5.11 (a), interestingly, at exposure to 30% RH for 1 minute under free convection condition, vapor absorbed by the dope solution $P_{15}T_{55}PI_0$ was not enough to render the system in the metastable region, but rather kept the cast film at the late homogenous stage of the ternary phase diagram. As the cast solution film was transferred to the water bath, the abrupt increase in non-solvent concentration of the exposed film surface induced the formation of the skin layer through the rapid liquid-liquid demixing kinetics. However, the underlying layers of the cast film were at the late homogenous stage. The rapid coagulation of the polymer at the top layer yielded a thin skin

layer which slowed down the further introduction of the non-solvent to the underlying layers. In consequence, the underlying layers were permitted more time to start NG as the non-solvent slow diffusion induced metastable condition. This resulted in a membrane with sponge-like cross-section, still, a skin layer at the top surface was developed as demonstrated in Figure 5.12 (d).

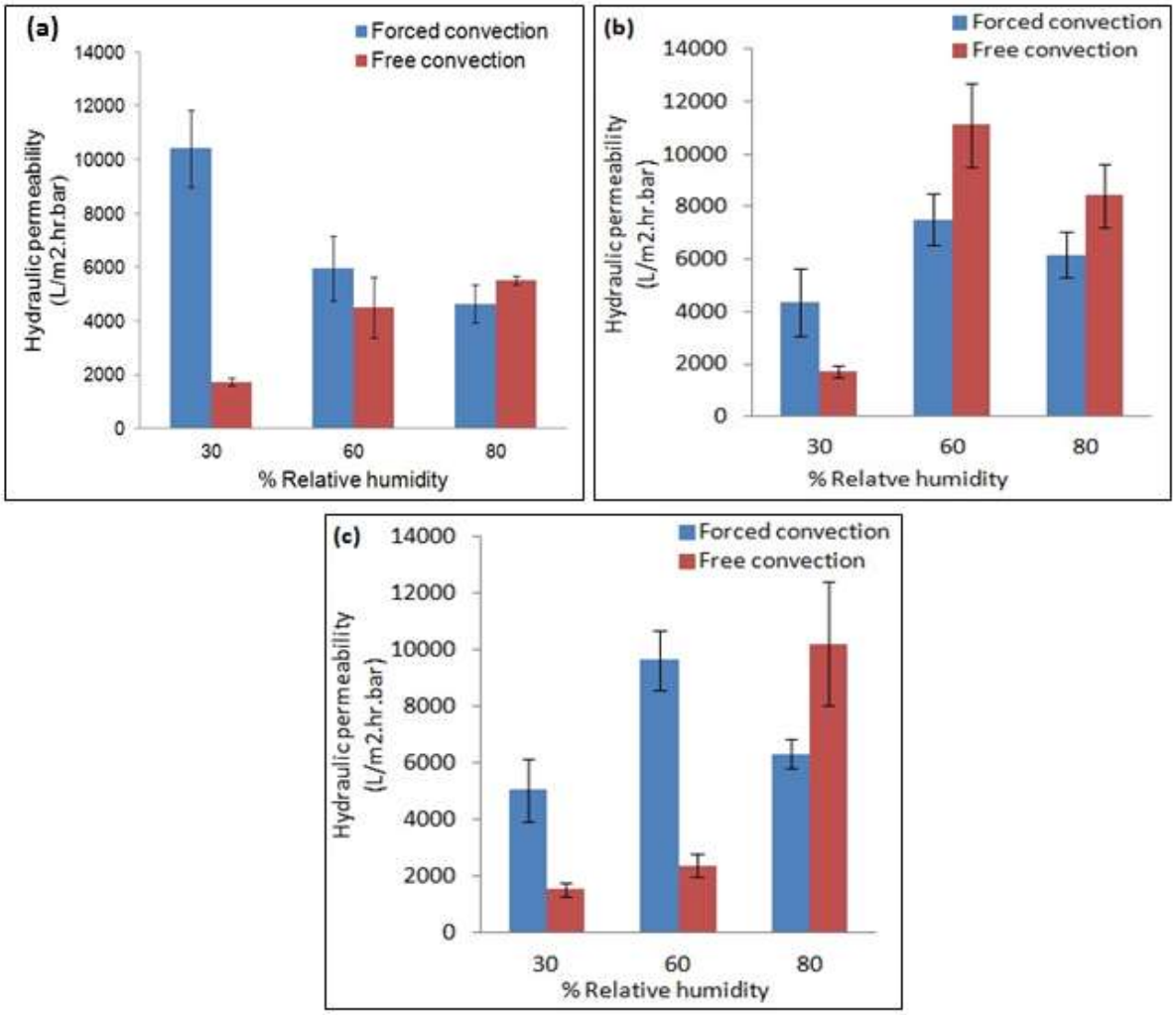

Figure 5.11: Free and forced convection effect on hydraulic permeability of membranes prepared by solutions (a) $P_{15}T_{55}Pl_0$, (b) $P_{15}T_{54}Pl_1$ and (c) $P_{15}T_{50}Pl_5$ at different % RH

The difference between the thermodynamic state at the cast solution interface and underlying layers was a result of using free convection instead of forced convection. Forced convection increases the mass transfer to the cast solution which was repeatedly reported in the literature [142,154,156]. Thus, at free convection condition, water vapor diffuses to the cast solution merely depending on the other two factors affecting vapor absorption, namely: chemical potential of the vapor [141,143,146,147,149] and the affinity of the cast solution [90,93,94]. When solution composition and RH value were fixed, the only factor influencing the vapor absorption then was the convection condition. Accordingly, diffusion is relatively slower with free convection when compared to that with forced convection.

This slow diffusion of vapor causes a high concentration gradient at the interface. The formation of liquid layer on top of the cast film has been reported by Menut et al. and Matsuyama et al.[143,144]. Also later observed and recorded by Lee et al. [76]. This liquid layer concentration gradient drives NMP from the underlying layers by percolation. The NMP migration from the underlying layers towards the interface has two influences. First, it decreases the stability of the underlying layers and shifts the composition at these depths towards the metastable state. Second, it dilutes the cast film at the interface and shifts its composition to more stable state. Accordingly, as a result of this redistribution of the solvent, the interface becomes more stable than the underlying layer. Following to that, the coagulation bath causes instantaneous demixing to the homogenous solution at the interface creating a skin layer. However, the underlying layers undergo NG and render the isotropic cross-section morphology. The final membrane structure then comprises a skin layer on the top surface and isotropic cross-section morphology. This structure hereinafter will be referred to as “semi-symmetric” cross-section morphology.

This phenomenon of NMP diffusion was previously presented in the literature where NMP diffusion to the cast solution surface was ascribed to two different influences. In the work of Caquineau et al. they proposed that NMP migration to the top of the cast film shifted the top layer to homogenous state [142]. On the other hand, Menut et al. stated that NMP diffusion was accompanied by the polymer dissolved in the solvent; hence, the polymer concentration was higher at the top layer. This higher polymer concentration was responsible for the skin layer formed in their study [150].

A similar effect took place with $P_{15}T_{54}Pl_1$-$H_{30}C_0$ and $P_{15}T_{50}Pl_5$-$H_{30}C_0$. Generally, the major difference between both solutions was the quantity of vapor absorbed during the exposure time to water vapor. This quantity of vapor determined the degree of the solution stability and how far is the solution from the binodal boundary at the end of exposure time.

This difference in the thermodynamic state was not noticeable when forced convection was used. Although the effect of forced convection was poorly reported in the literature, most researchers agree that the time for precipitation decreases with the increase of the convection flow rate. Some researchers related this effect to the increase of the non-solvent in-diffusion with the increase in convection flow rate [156]. Others related it to the increase in solvent evaporation rather than non-solvent absorption [154]. Both justifications are valid. Yet, in our study the solvent was NMP which is well known for its low vapor pressure. Accordingly, evaporation of NMP was considered negligible in many studies. Thus, considering our cast solution system, the effect of convection force mainly increased the diffusion of water vapor to the cast film. The increased rate of water vapor diffusion from the humidity chamber to the film was reflected as well on its diffusion along the whole cross section of the cast film. Accordingly, no major difference was noticed between the solution interface and its cross section when forced convection was used.

There were two interplaying effects as a result of increasing Plu content. The first is the increase in the solution degree of hygroscopicity which was more prominent in case of $P_{15}T_{54}Pl_1$ solution. Accordingly, the cast film absorbs higher quantity of water vapor compared to $P_{15}T_{55}Pl_0$. The solution then moved further towards the binodal boundary and became less stable. This decreased the severity of the abrupt exposure of the top layer to the non-solvent in the water bath. Accordingly, the skin layer formed is presumably more porous which was confirmed by the higher hydraulic permeability of $P_{15}T_{54}Pl_1$-$H_{30}C_0$ versus $P_{15}T_{55}Pl_0$-$H_{30}C_0$.

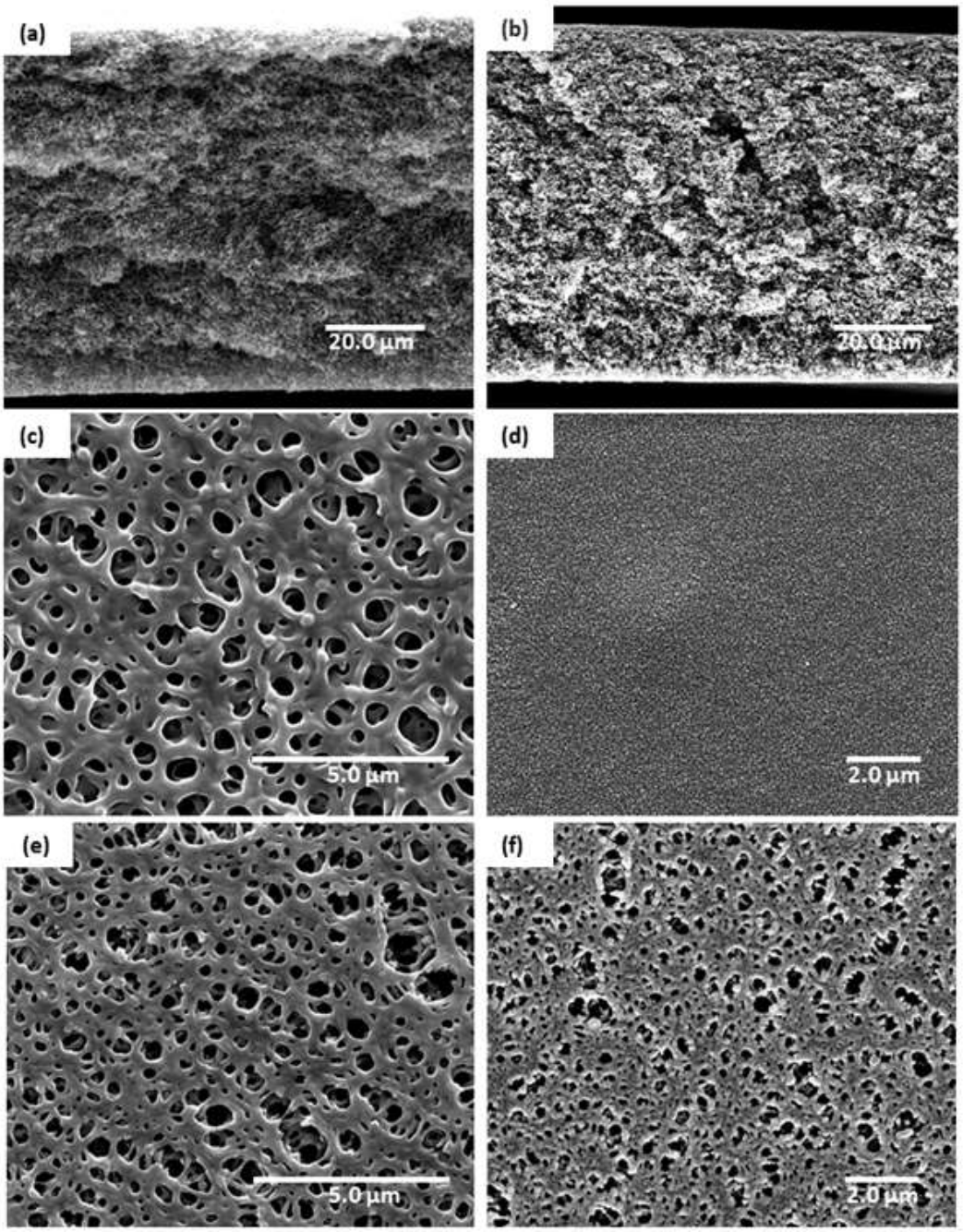

Figure 5.12: SEM micrographs of $P_{15}T_{55}Pl_0$-H_{30} membranes representing cross section, top and bottom surface at forced convection (a, c, e) and free convection (b, d, f), respectively

The second effect is the increase in solution viscosity which is demonstrated by $P_{15}T_{50}Pl_5$ solution. In case of the higher viscous solution of $P_{15}T_{50}Pl_5$, the hindrance to the vapor diffusion is higher. Following this, the immersion in the non-solvent water bath instantaneously created a skin layer. However, in this case the water diffusion through the cast film was much slower as it was resisted by both the increased viscosity and the skin layer formed. Subsequently, macrovoids near the bottom surface of the membrane were observed (as seen in Figure 5.13 (c)), indicating that time permitted for the polymer lean nuclei to coalesce was longer at the bottom layers.

On the other hand, increasing the relative humidity degree at exposure for $P_{15}T_{55}Pl_0$ from 30% to 60% or 80%, lead to a rapid crossing to the binodal boundary due to higher chemical potential driving higher rate of vapor absorption, and thus, more time was available for NG and for polymer-lean nuclei to coalesce. Accordingly, the hydraulic permeability increased with the increase of relative humidity which represents complete opposite trend to the effect of increased relative humidity under forced convection as shown in Figure 5.11 (a).

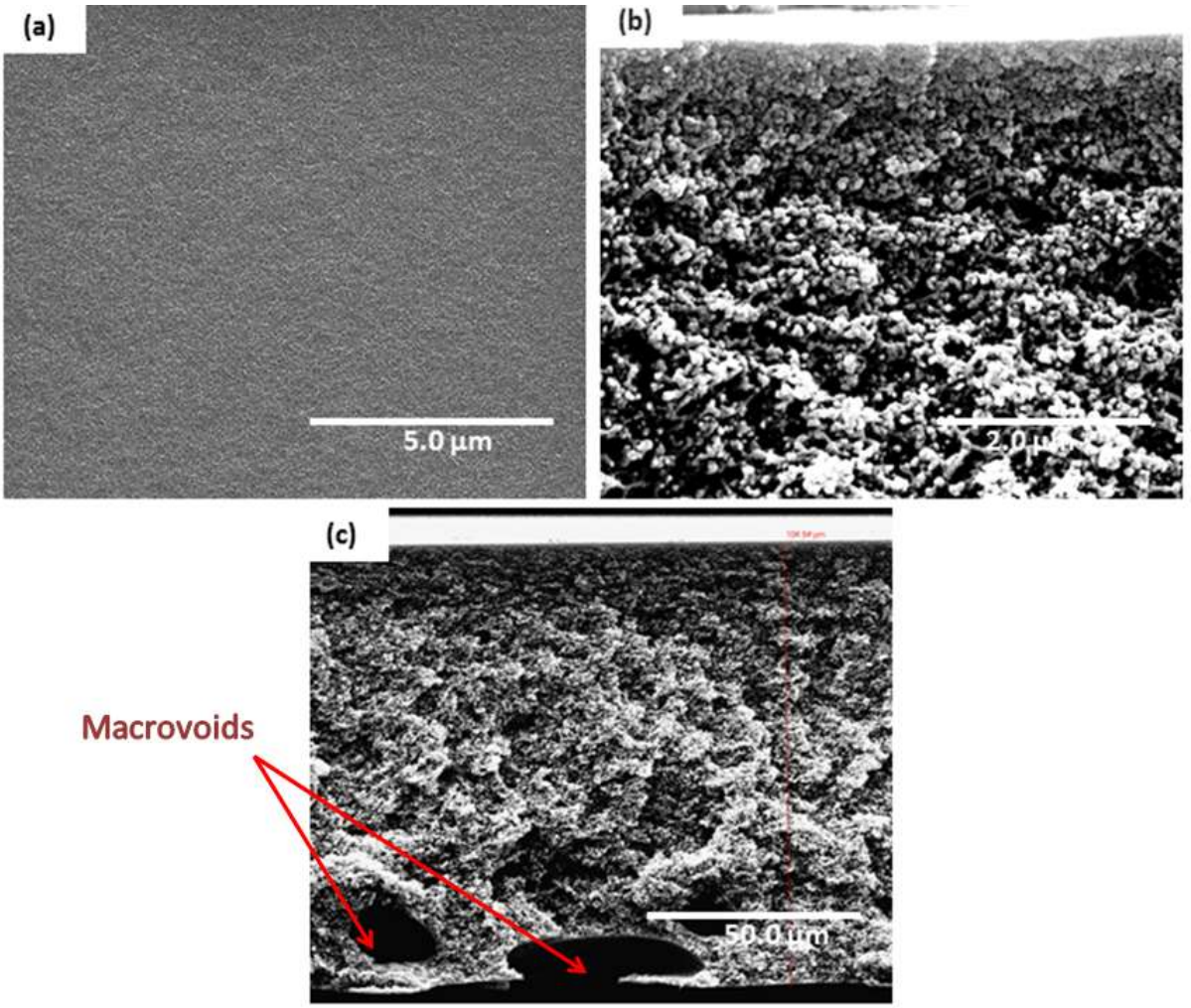

Figure 5.13: SEM micrographs of $P_{15}T_{50}Pl_5$-$H_{30}C_0$ samples showing top surface, cross-section near top surface and overall cross-section in a, b and c respectively

In case of $P_{15}T_{54}Pl_1$ solution, increasing the RH to 60% allowed enough water vapor to be imbibed by the dope solution and along the whole cross-section. The system was driven to cross the binodal boundary where NG took place, and, the process of absorption was slow enough allowing more time for polymer-lean phase to grow. Thus, this yielded larger pore diameters as compared to 30% RH exposure with free convection. Even more, pores were larger than those created when same dope solution was subjected to 60% RH under forced convection and demonstrated in the increase of hydraulic permeability (Figure 5.11 (b)). Because, when vapor was forced to diffuse into the cast film, considerably larger quantity of water was introduced inducing more rapid crossing of the metastable region and earlier induction of SD process. Instead, at free convection the solution stayed longer in the metastable region which reflected in the nuclei coalescence and the formation of larger pores. On the other hand, the exposure of $P_{15}T_{54}Pl_1$ solution to 80% RH under free convection, the vapor higher chemical potential drove the water into the dope solution faster and final membrane had smaller pore size and lower hydraulic permeability relative to that at 60% RH as shown in Figure 5.11 (b).

The solution viscosity increases with increasing Plu content. Accordingly, with the increased viscosity of $P_{15}T_{50}Pl_5$ cast solution, under free convection the viscosity barrier demonstrated a major hindrance to the effect of increasing the vapor chemical potential (as represented in Figure 5.5). Accordingly, only at 80% RH, the vapor chemical potential was high enough to overcome the viscosity barrier; hence, vapor absorption had significantly increased the hydraulic permeability as shown in Figure 5.11 (c). This indicates that the NG process took place for a longer time period only at 80% RH.

D. Validation of free versus forced convection effect:

To validate the effect of convection force, solutions with relatively higher stability were tested at the two extremes of humidity for 1 minute exposure time, that is to say, solutions with compositions that lies further away from the binodal boundary. Dope solutions of $P_{15}T_{45}Pl_0$ and $P_{15}T_{25}Pl_0$ were tested under both convection conditions. As seen in Figure 5.14, the effect of convection at 30% RH in the highly stable solution $P_{15}T_{25}Pl_0$ was not significant. As the solution has relatively low viscosity, vapor absorption was quite fast even under free convection condition. Thus, forcing vapor diffusion to the cast film through forced convection did not show a significant difference on the final membrane. However, as the solution viscosity increases in $P_{15}T_{45}Pl_0$ due to higher TEG content, the forced diffusion effect become more prominent. Interestingly, increasing the RH value led to the increase in the mean flow pore diameter, which is a reflection to the more non-solvent introduced to the system.

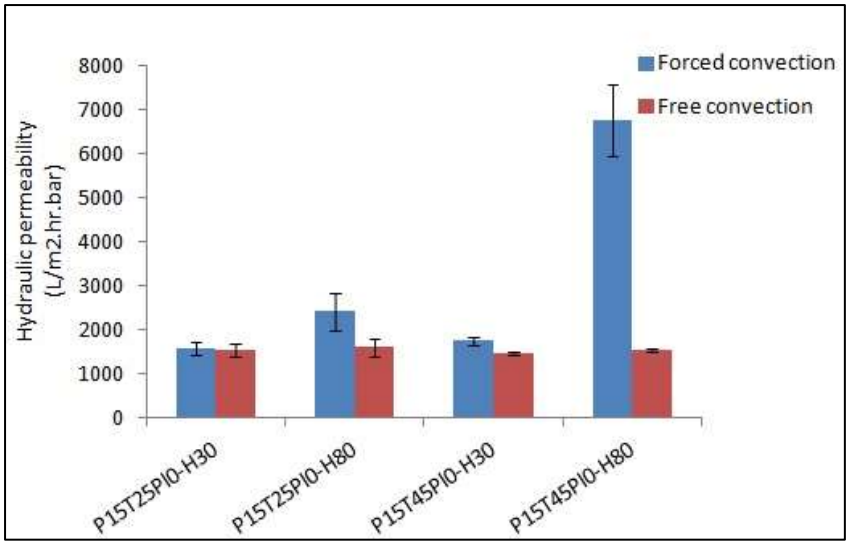

Figure 5.14: Free and forced convection effect on solutions with higher stability and lower viscosity at 30% and 80% RH

For solution $P_{15}T_{45}Pl_0$, the forced convection at 80% RH induced the state of metastability of the system, thus, nuclei formation and their coalescence took place and showed a significant increase in the hydraulic permeability as represented in Figure 5.14. The solution thermodynamic behavior during the exposure time of 1 minute is schematically represented in Figure 5.15.

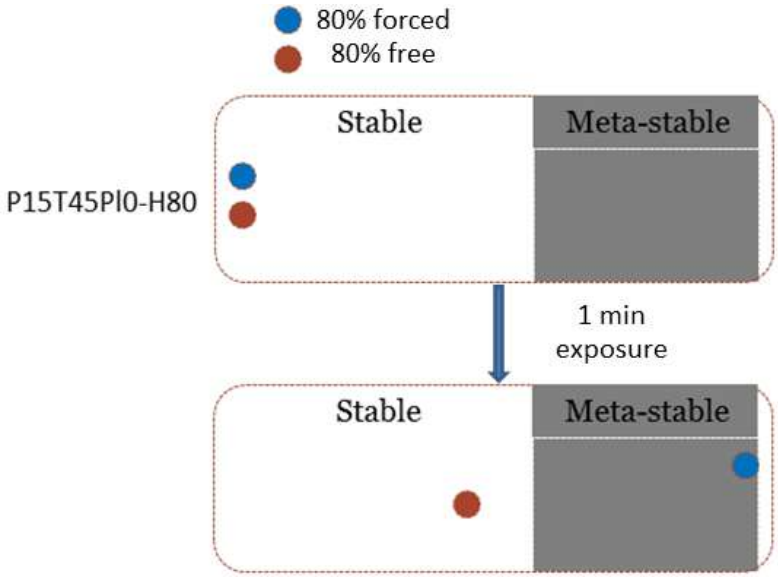

Figure 5.15: Effect of free and forced convection on $P_{15}T_{45}Pl_0$ cast solution under 80% RH

SEM micrographs in Figure 5.16 provide a clear example of the significance of convection force. As demonstrated, at 80% RH free convection created asymmetric membrane with underlying finger-like macrovoids while forced convection ended-up forming a symmetric structure. The complete shift in the cross section morphology from anisotropic to isotropic was only tailored by the convection condition. The anisotropic structure is typically crated

from the spontaneous phase inversion of homogenous solution at stable thermodynamic state. On the contrary, the isotropic sponge-like structure is an outcome of NG process which takes place only when the solution reaches the thermodynamic metastable state. Thus, these results demonstrate the influence of convection on the solution thermodynamic state during VIPS process. This illustration, along with the aforementioned experiments, provides evidence that the generalization of humidity exposure effect is irrelevant and mainly dependent on the solution composition and force of convection in VIPS process even at short exposure time.

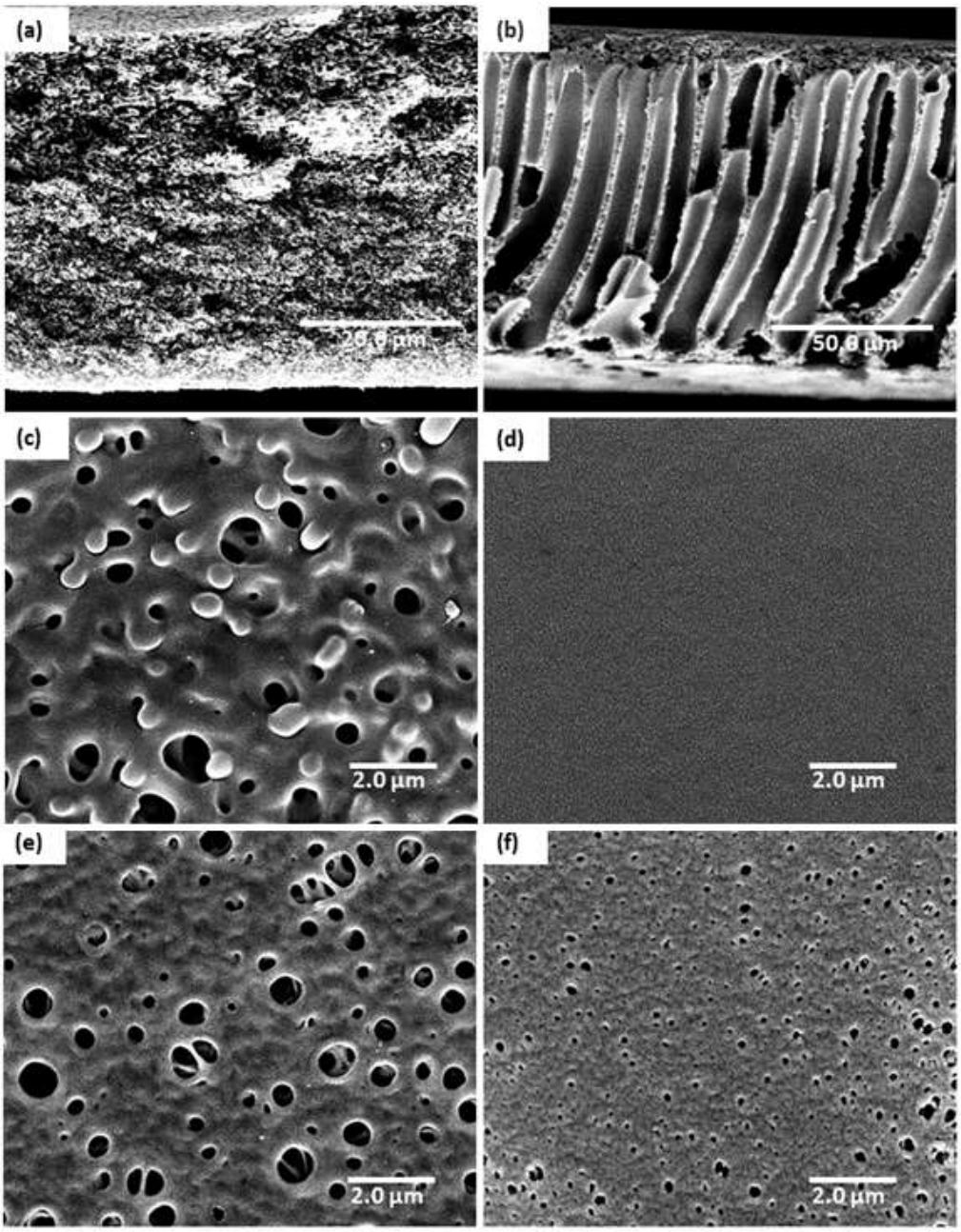

Figure 5.16: SEM micrographs for samples $P_{15}T_{45}Pl_0$-H_{80} representing cross section, top and bottom surface at forced convection (a, c, e) and free convection (b, d, f), respectively

5.1.3. Effect of Nanoparticles incorporation

Nanoparticles of TiO_2 were incorporated so as to compare their effect against that of Plu in improving the membrane performance by enhancing its hydraulic permeability and compaction resistance. Once the TiO_2 was added to the cast solution, the solution was sonicated to disperse the NPs. The particle size distribution for the solution was then measured. As shown in Figure 5.17, the solution with the unfunctionalized NPs resulted in aggregates with 859 nm in diameter. On the other hand, ɣ-aminopropyl triethoxysilane functionalized NPs were successful in producing a solution with better NPs dispersion where the mean size distribution was 66.3 nm. This better distribution was a result of decreased surface free energy as a result of surface functionalization; and hence, reduced particles aggregation [76]. Accordingly, the later preparation procedure was followed in preparing all cast solutions that included TiO_2 NPs.

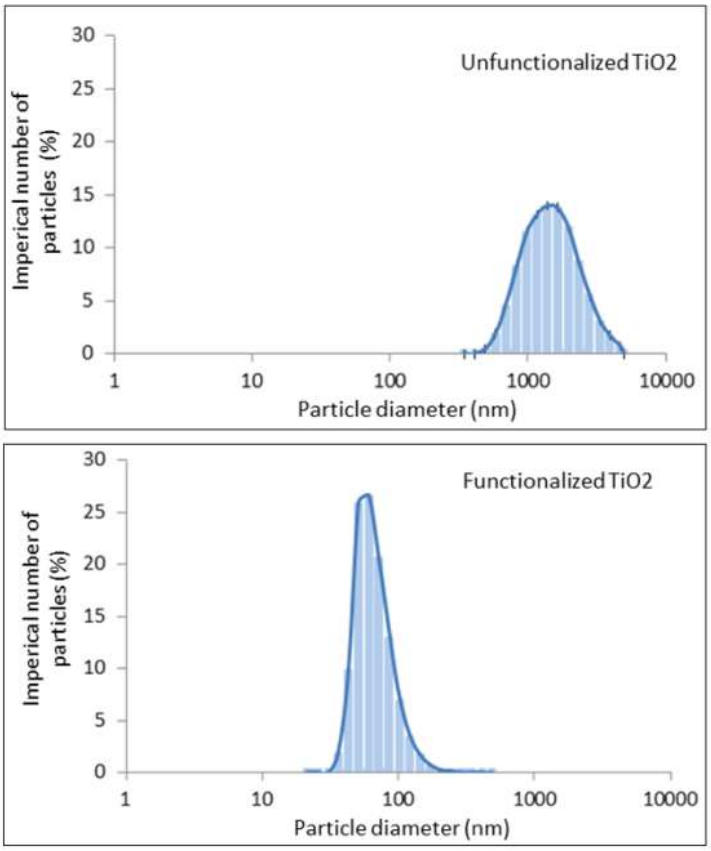

Figure 5.17: Particle size analysis for cast solution with unfunctionalized and functionalized NPs

To fabricate membranes with the favorable semi-symmetric structure, similar conditions to those applied to Plu-containing solutions were adopted. Accordingly, solutions with 0.1 and 1 wt% TiO_2 were exposed to 30% RH under free convection for 1 minute. Those two specific concentrations were chosen in order to have an overview over the general effect of NPs concentration. The resultant membranes showed isotropic cross-section morphology and not the semi-symmetric structure. The hydraulic permeability increased from 5,152 to 5,989

L/m^2.hr.bar for $P_{15}T_{54.9}N_{0.1}$-$H_{30}C_0$ and $P_{15}T_{54}N_1$-$H_{30}C_0$, respectively as represented in Table 5.2. The produced isotropic morphology (Figure 5.18) illustrates that the solutions have reached the metastable region where NG took place. On comparing the Plu-containing cast solution to NPs-containing cast solution of same concentration (1 wt%), the Plu-containing cast solution had semi-symmetric structure when exposed to same conditions. This means that NPs-containing cast solution stayed longer in the metastable region. The $P_{15}T_{54.9}N_1$ solution viscosity is higher than $P_{15}T_{54}Pl_1$ (8.19 Pa.s and 6.33 Pa.s, respectively). Consequently, it is reasonable to suggest that the affinity to absorb water vapor was higher with the inorganic NPs than that of Plu of same concentration.

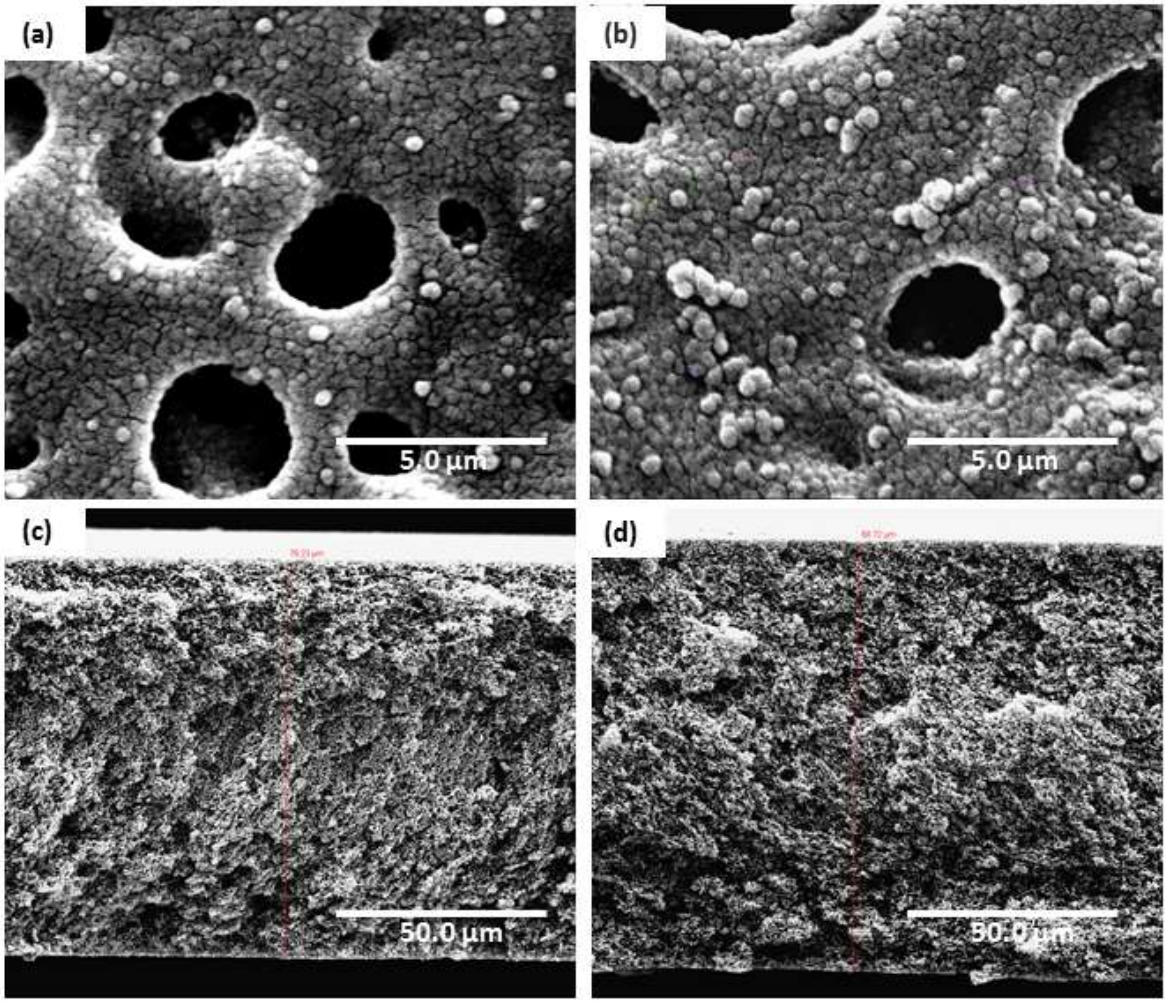

Figure 5.18: SEM micrographs of $P_{15}T_{54.9}N_{0.1}$-$H_{30}C_0$ and $P_{15}T_{54}N_1$-$H_{30}C_0$ showing top surface (a, b) and cross-section (c, d), respectively

One approach to achieve the semi-symmetric membrane morphology is to allow the cast solution to cross the binodal boundary at a late stage of the exposure time (i.e. just prior to LIPS process) as explained earlier. Thus, in order to achieve the semi-symmetric membrane morphology for NPs-containing cast solutions, the exposure time was decreased to 20 seconds. The reduction in the exposure time should allow the cast solution to absorb non-solvent from the surrounding vapor, yet, the absorbed vapor concentration would be small

enough not to permit long period of NG process. Successfully, with TiO_2 concentrations of 0.05 and 0.1 wt% the semi-symmetric morphology was achievable when exposure time was decreased to 20 seconds as shown in Figure 5.19. However, NPs at the top surface were not detected by imaging.

The hydraulic permeability increased with increasing the NPs content as seen in Figure 5.20. This increase was more significant when NPs concentration increased to 1 wt%. This observation could be ascribed to the membrane surface porosity and the absence of skin layer when NPs concentration increased to 0.5 and 1 wt%. Solutions containing 0.5 and 1 wt% TiO_2 resulted in isotropic membranes with sponge-like cross-section morphology. This morphology explains the increase in the hydraulic permeability with $P_{15}T_{54.5}N_{0.5}$ and $P_{15}T_{54}N_1$. In addition, for $P_{15}T_{54.5}N_{0.5}$ membrane samples, NPs scattered along the surface were observed in the SEM micrographs as shown in Figure 5.21 (c). Still, $P_{15}T_{54}N_1$-$H_{30}C_0$ samples had higher hydraulic permeability than $P_{15}T_{54.5}N_{0.5}$-$H_{30}C_0$ due to larger surface pore diameter (Figure 5.21 (d)) that was accompanied by the higher solution hygroscopicity due to the higher NPs content. Cast solutions with 0.5 and 1 wt% TiO_2 showed isotropic cross-section at 20 seconds exposure time. Further shortening of the exposure time was not practically possible, thus, only $P_{15}T_{54.95}N_{0.05}$-$H_{30}C_0$ and $P_{15}T_{54.9}N_{0.1}$-$H_{30}C_0$ membranes were used as TFNC support membranes as they showed the desirable semi-symmetric structure.

Table 5.2: Various cast solutions containing TiO_2 NPs viscosity and their respective membranes hydraulic permeability (J_w) at different exposure time (t_e) for 30% RH under free convection

Cast solution	Viscosity at 20 ^{0}C (*Pa.s*)	t_e 30% RH	J_w ($L/m^2.hr.bar$)
$P_{15}T_{54.95}N_{0.05}$	n.d.[a]	20 sec	1363 (±124)
$P_{15}T_{54.9}N_{0.1}$	6.53	1 min	5152(±566)
		20 sec	1939 (±398)
$P_{15}T_{54.5}N_{0.5}$	n.d.	20 sec	3273 (±135)
$P_{15}T_{54}N_1$	8.19	1 min	5989 (±712)
		20 sec	5375 (±123)

[a] *n.d. stands for not determined values.*

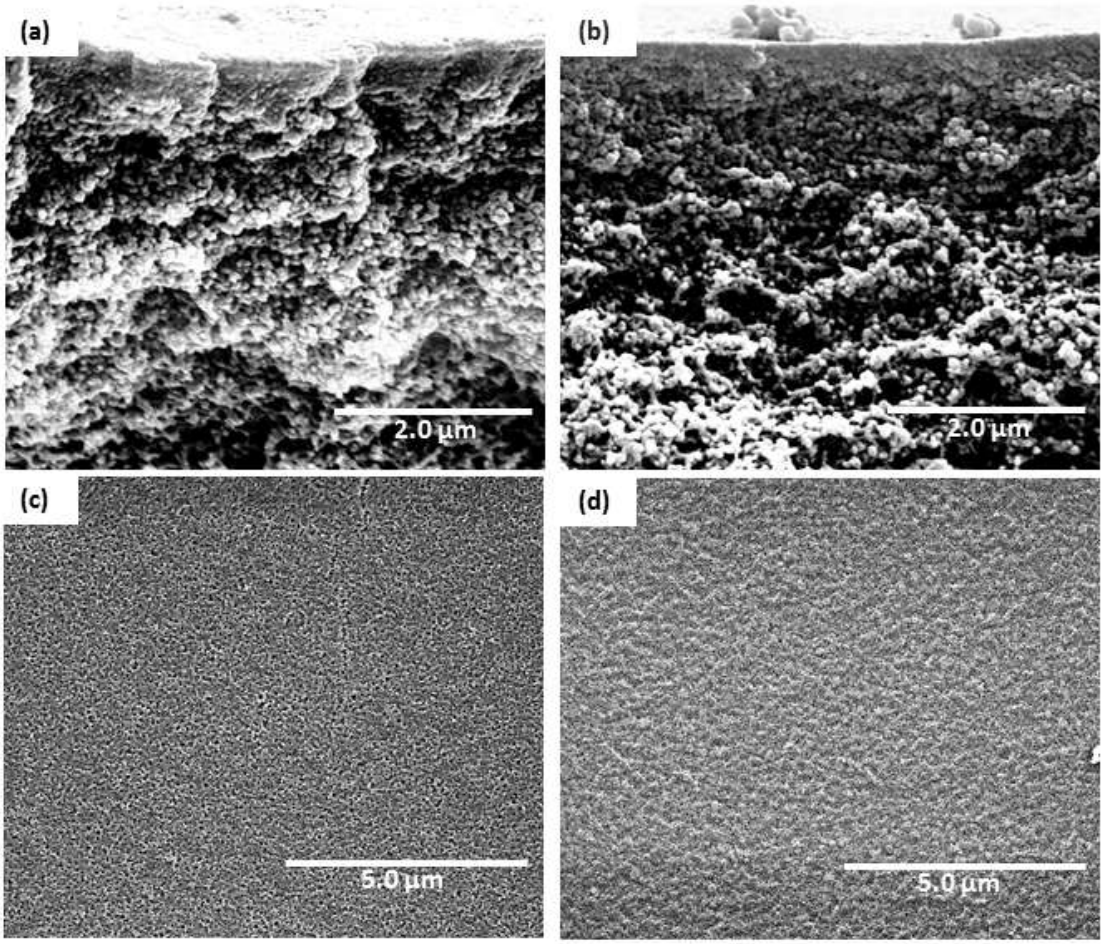

Figure 5.19: SEM micrographs of $P_{15}T_{54.95}N_{0.05}$-$H_{30}C_0$ and $P_{15}T_{54.9}N_{0.1}$-$H_{30}C_0$ representing cross-section (a, b) and top surface (c, d), respectively

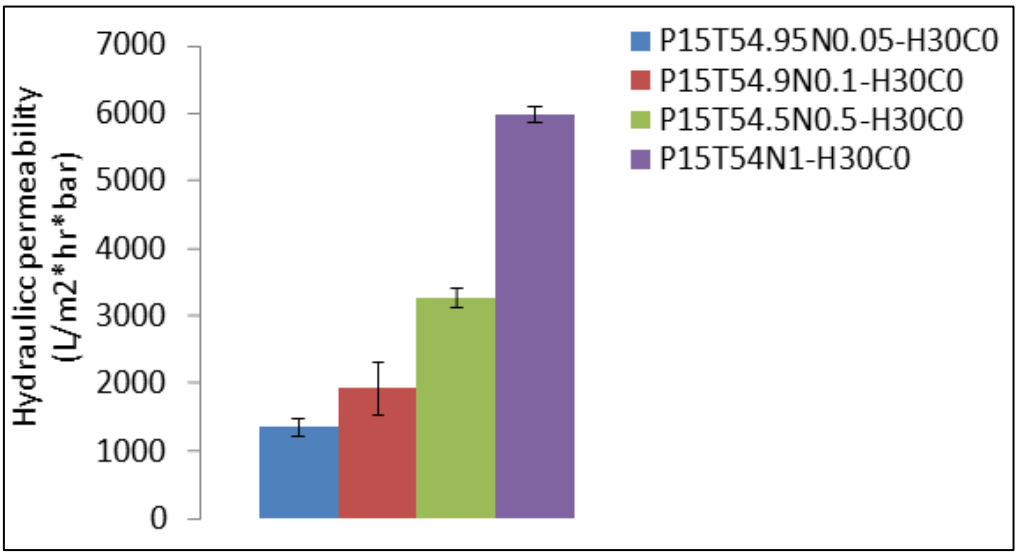

Figure 5.20: Hydraulic permeability of membranes with increasing NPs concentration

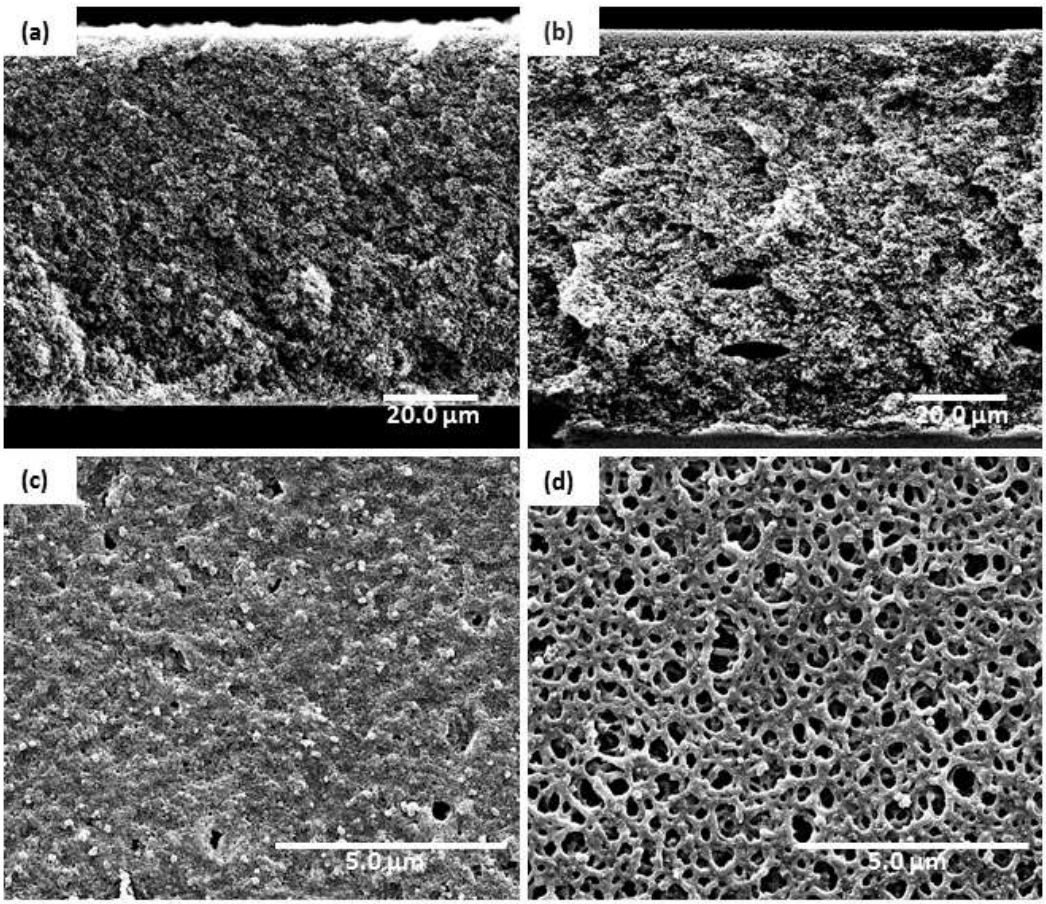

Figure 5.21: SEM micrographs of $P_{15}T_{54.5}N_{0.5}$-$H_{30}C_0$ and $P_{15}T_{54}N_1$-$H_{30}C_0$ representing cross-section (a, b) and top surface (c, d), respectively

5.2. TFNC support-membrane characterization

5.2.1. NMR Plu entrapment

H^1NMR analysis was used to quantify the Plu to PES weight% in the final membrane samples. As shown in Figure 5.22, the spectra had peaks appearing at ~1 ppm for methyl group, ~3.4 for methylene group and ~3.5 ppm for methyne group of the Plu. PES aromatic protons also appear in two split peaks from 7 to 8 ppm. Thus, the ratio between the integrated peaks at 1 ppm and 7-8 ppm was used to calculate the Plu to PES weight% in the final membrane.

As Plu is a water miscible polymer, it is expected to leach out of the membrane matrix in the non-solvent water bath during the LIPS step. However, this possible leaching is resisted by the Plu entanglement to the PES matrix. Accordingly, the wt% of Plu/PES increased with higher Plu entrapment which resulted from samples having smaller average pore diameter.

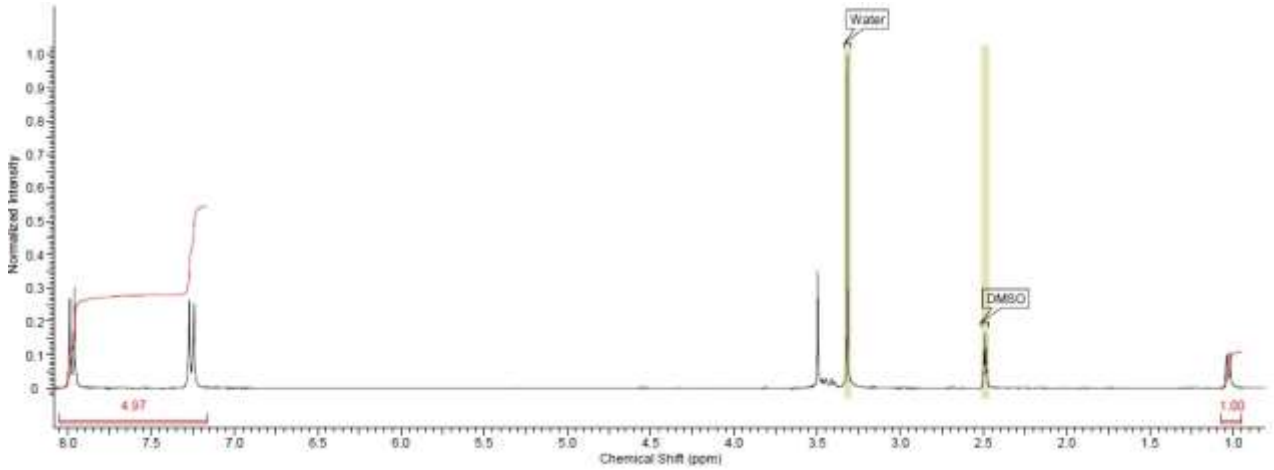

Figure 5.22: H^1NMR spectra for $P_{15}T_{50}Pl_5$-H_{80} with integrated peaks representative to (4H) of Plu® at ~1.1 ppm and (8H) of PES at ~7.2-8 ppm

Although the starting Plu/PES was 50 wt% in the cast solution $P_{10}T_{55}Pl_5$, Plu in the final membrane samples at 30% and 80% RH was around 34.6% and 47.96%, respectively. This change was due to Plu leaching, which decreased with the decrease in the average pore diameter. A similar behavior was observed when the Plu content in the dope solution increased. It was found that increasing the Plu/PES in the dope solution from $P_{15}T_{54}Pl_1$ to $P_{15}T_{50}Pl_5$ (i.e. from 6.67% to 33.33%) increased the final Plu/PES from ≈1.5% to 6%, respectively. This indicated higher fraction leaching for the $P_{15}T_{50}Pl_5$-$H_{80}C_f$ sample attributed to larger average pore diameter, and hence, lower entrapment. Similar observations relating the average pore diameter to Plu ratio was found when solutions of the same composition were subjected to different RH degrees as represented in Table 5.3. A comparable observation has been reported previously by Ulbricht et al. [94].

Table 5.3: Measured %Plu/PES based on H-NMR results for various membrane samples and the respective samples pore diameter

Composition	%RH	Mean flow pore diameter (nm)	(%Plu/PES)
$P_{10}T_{55}Pl_5$	30	621	3.46
	80	351	4.80
$P_{13}T_{55}Pl_2$	30	425	3.47
	80	181	3.90
$P_{15}T_{54}Pl_1$	30	168	2.7
	60	242	1.77
	80	200	1.49
$P_{15}T_{50}Pl_5$	30	182	6.83
	60	253	5.22
	80	219	6.02

5.2.2. Hydrophilicity:

A. Surface hydrophilicity

Surface hydrophilicity was evaluated for samples with increasing Plu concentration using captive bubble method. Figure 5.23 presents images for $P_{15}T_{55}Pl_0$-$H_{60}C_f$ and $P_{15}T_{54}Pl_1$-$H_{60}C_f$ showing the significant change in contact angle decreasing from 61^0 to 44^0, respectively. Unexpectedly, the further increase of Plu to 5wt% in $P_{15}T_{54}Pl_5$-$H_{60}C_f$ increased the contact angle to 58^0, thus indicating a decrease of surface hydrophilicity. This observation might be explained in light of the different orientation the Plu building blocks may attain.

As Plu consists of hydrophilic and hydrophobic blocks of PEG and PPG, respectively, the orientation that blocks adopt reflects in the membrane surface hydrophilicity. During the process of combined VIPS/LIPS, firstly the PPG blocks orient to the dope solution/air interface resulting in a hydrophobic surface. On the other hand, in the coagulation bath reorientation takes place and hydrophilic PEG blocks start to protrude to the polymer/water interface increasing the surface hydrophilicity. Using advanced spectroscopy, Shi et al. observed the different conformations of Plu®127 in PES model films [198]. Similarly, Suk et al. and Ulbricht et al. observed the same behavior of Plu blocks under VIPS process [199, 94]. Understanding this, it is reasonable that the increase in dope solution viscosity would hinder such reorientation. Accordingly, solution $P_{15}T_{54}Pl_5$ brought more hydrophobic groups to the surface, those groups were harder to reorient due to the increased viscosity compared to $P_{15}T_{54}Pl_1$ solution under similar conditions of 60% RH. As a consequence, $P_{15}T_{54}Pl_5$-$H_{60}C_f$ samples had higher contact angle than $P_{15}T_{54}Pl_1$-$H_{60}C_f$.

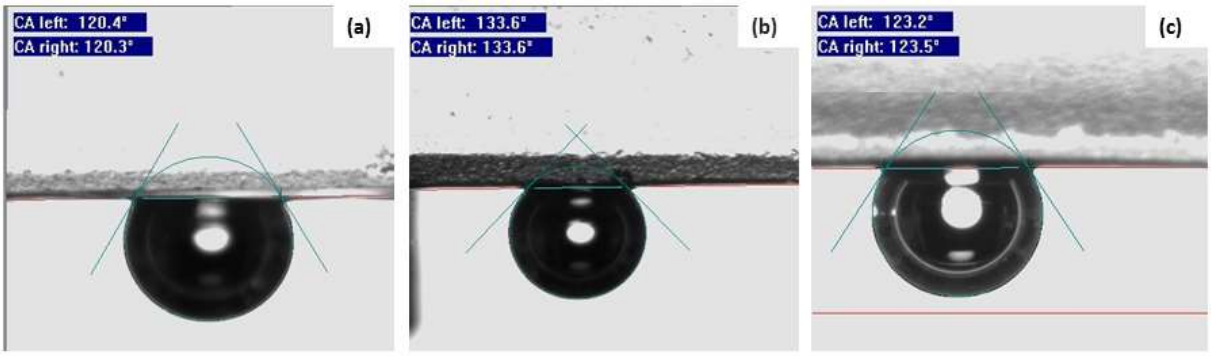

Figure 5.23: Contact angle images for (a) $P_{15}T_{55}Pl_0$, (b) $P_{15}T_{54}Pl_1$ and (c) $P_{15}T_{54}Pl_5$ samples exposed to 60% RH using captive bubble method

On the contrary was the behavior at 30% RH under forced convection. In this case vapor mass transfer to the cast film was higher, as formerly explained. This created higher chemical potential for the hydrophilic affinity of Plu, hence, Plu subjected its PEG hydrophilic moiety to polymer/vapor interface during the VIPS process. Followed by coagulation in the non-solvent bath, the membrane matrix fixed the blended Plu with this favorable orientation. Thus, increasing Plu up to 5wt%, regardless of the viscosity barrier, was successful in inducing more surface hydrophilicity compared to 1wt% addition. This is due to

the higher availability of hydrophilic moieties with the higher Plu concentration. Correspondingly, the contact angle was reduced from 52^0 to 41^0 for $P_{15}T_{54}Pl_1$-$H_{30}C_f$ and $P_{15}T_{50}Pl_5$-$H_{30}C_f$. Similar behavior was observed at 80% RH as shown in Figure 5.24.

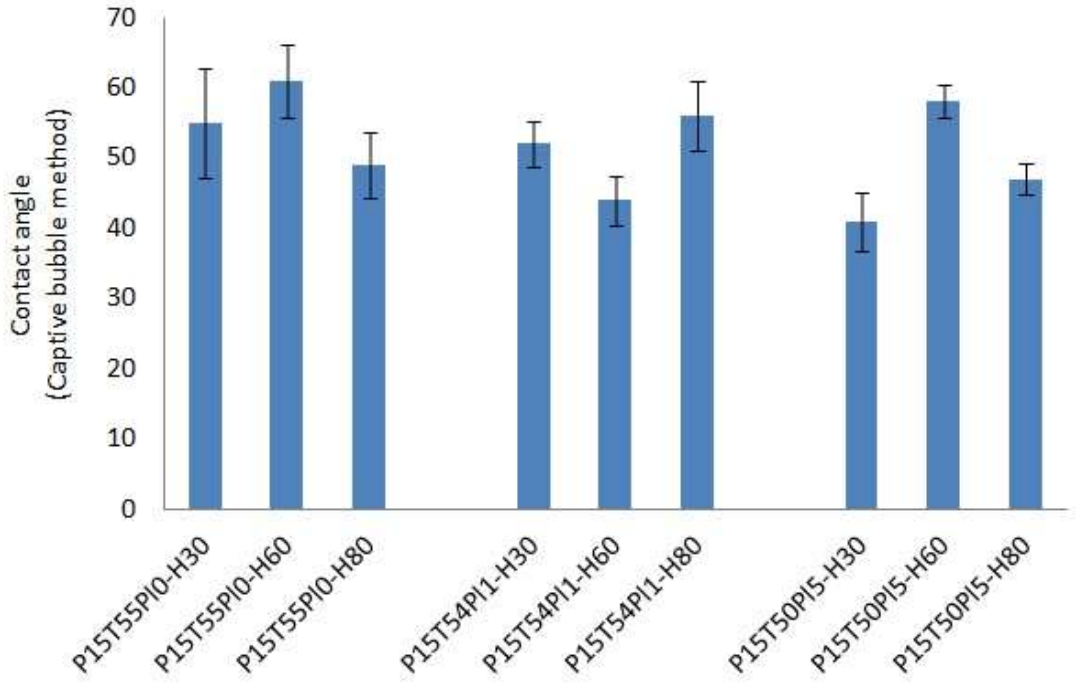

Figure 5.24: Contact angle for various membranes under RH of 30%, 60% and 80%

B. Bulk hydrophilicity:

Wettability measurements showed total agreement with Plu content calculated from NMR charts. As shown in Figure 5.25, the curves slopes show the rate of water droplet diffusion through the membrane. As seen, increasing Plu content generally increased the slope negative value. Furthermore, comparing samples of the same composition but prepared under different conditions illustrated the difference in Plu entrapment. Furthermore, comparing the wettability of $P_{15}T_{55}Pl_0$ solution under different conditions of RH value showed inverse proportionality of wettability with pore size (Figure 5.25 (a)). This suggests that the capillary effect of smaller pore diameters increases the wettability. More interestingly, membranes with smaller average pore diameter had higher Plu entrapment (as explained earlier). Hence, membranes with smaller pore diameter had higher wettability because capillarity acted synergistically with the higher Plu entrapment as per the results shown in Figure 5.25 (b and c).

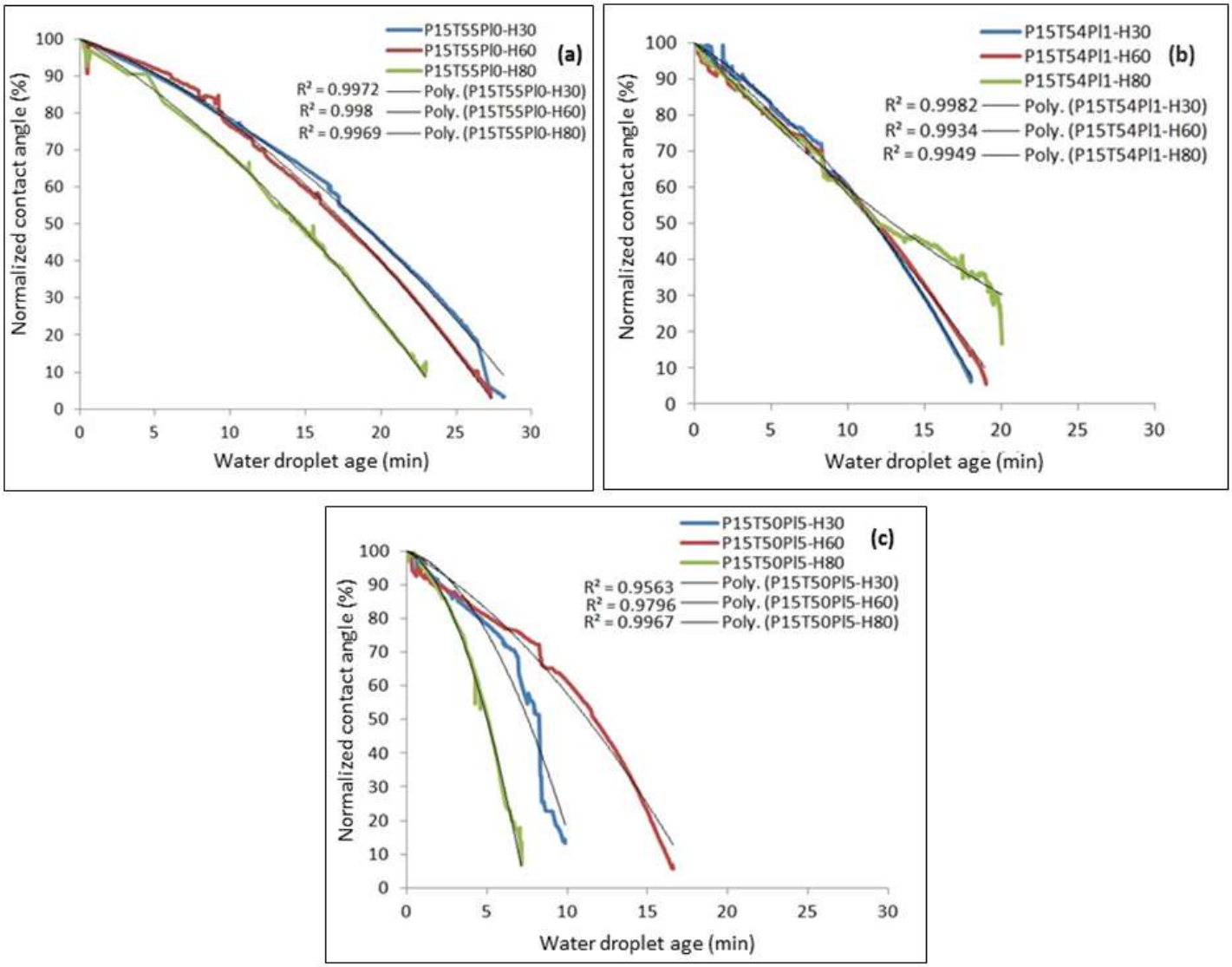

Figure 5.25: Wettability curves under various %RH exposure for (a) $P_{15}T_{55}Pl_0$ (b) $P_{15}T_{55}Pl_1$ (c) $P_{15}T_{55}Pl_5$

In order to compare the induced hydrophilicity effect of NPs, wettability experiments were conducted with samples with different amounts of incorporated TiO_2 NPs. Results shown in Figure 5.26 demonstrated that wettability increased with increasing NPs concentration in the cast solution. Yet, membrane formed with 1 wt% TiO_2 showed the lowest wettability. This observation supports the suggested pore blocking effect with high NPs concentration as discussed above and reported in literature [37,38]. It is important to note that the wettability behavior increased with the increase of NPs regardless of the membrane cross section morphology which is different from the behavior showed when Plu was the additive used.

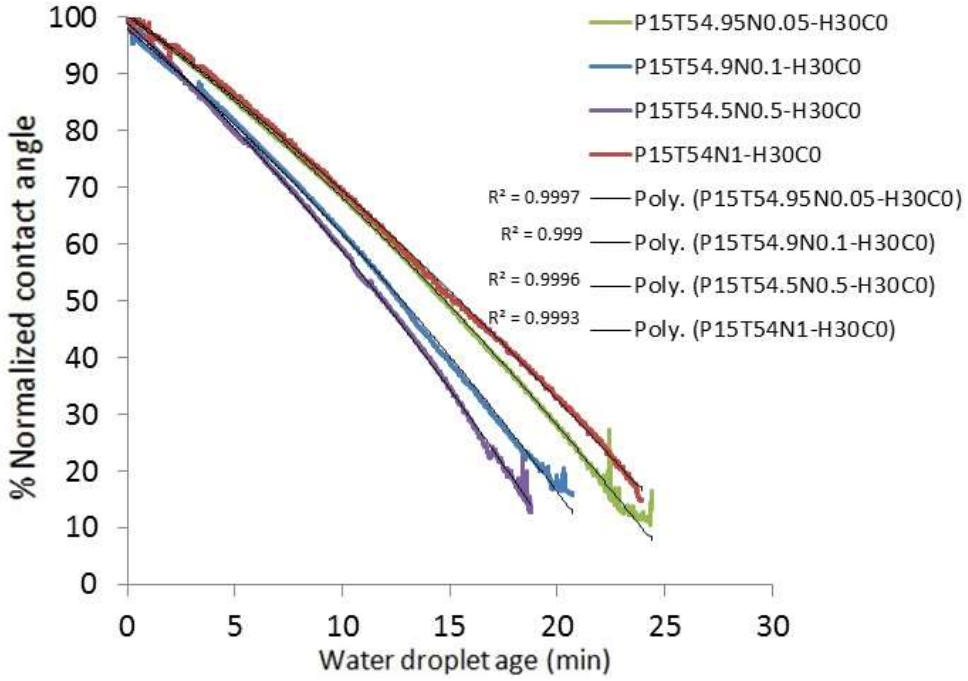

Figure 5.26: Wettability curves of membranes with increasing NPs concentration

On the other hand, with comparing membranes with different structures, interestingly semi-symmetric morphologies showed the highest wettability. As illustrated in Figure 5.27, the isotropic morphology showed lower wettability relative to the anisotropic membrane of same composition. The lowered wettability is intuitive as the water droplet is supposed to wet the surface pores first before starting to diffuse through the cross section. Accordingly, the isotropic surface pores filled with air hinders this wetting, counter to the effect of anisotropic structure skin surface. Also, isotropic structure with the incorporated NPs showed better wettability compared to the membranes of nascent composition.

On the other hand, the semi-symmetric membranes had superior wettability as compared to both the anisotropic and the isotropic membranes of the same composition. The semi-symmetric membrane had better wettability than the isotropic structure for the same reason explained in the preceding paragraph which is the better surface wetting. Although semi-symmetric and asymmetric membranes have skin layer, semi-symmetric membrane showed better wettability. The difference in wettability is then attributed to the inner membrane structure. The semi-symmetric structure has interconnected porous morphology in the cross section below the skin layer. This interconnectivity facilitated the diffusion of water through the membrane. On the contrary, the asymmetric structure has thicker skin layer and air filled macrovoids, and both resist wettability.

The highest permeability was for the semi-symmetric structure with the highest Plu content as shown in Figure 5.27. The $P_{15}T_{50}Pl_5$-$H_{30}C_0$ membrane held many privileges for increasing wettability. It acquired the preferable thin skin layer and the interconnected porous

structure. Besides, the higher entrapment of Plu in the dense skin layer increased the surface hydrophilicity.

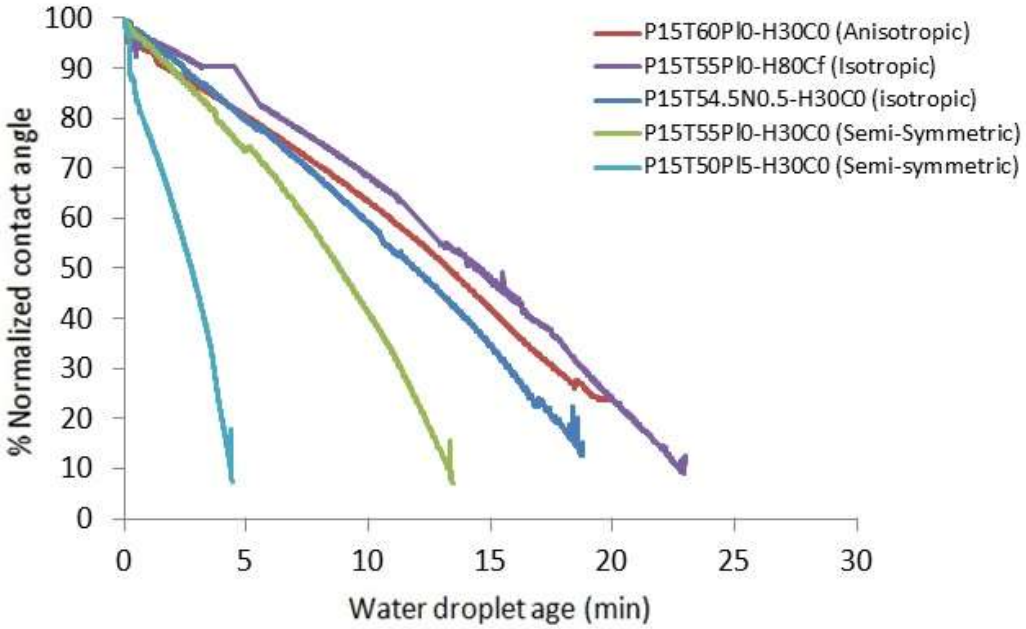

Figure 5.27: Wettability curves of membranes having different morphologies

5.2.3. Porosity

Membrane porosity was calculated in percentage pore volume to sample total volume using Equation 8 and the data presented in Table 5.4. The average porosity of samples of different cast solution composition showed an increase with the increase in Plu concentration. All membrane samples with no Plu content produced at different RH degrees had an average porosity of 62%. By adding 1 wt% Plu to the cast solution, the pore volume reached 76% and was further increased to 80% with 5 wt% Plu. This agrees with the general trend of the membrane hydraulic permeability. As the Plu concentration increased the total polymer-lean phase volume increased; thus, the final pore volume increased. Accordingly, this observation substantiated the effect of Plu in increasing the vapor absorption by its hygroscopic effect.

Table 5.4: Thickness (*L*), area (*A*), mass (*m*) and calculated porosity (ε) for different membranes samples of 12.5 mm radius and total area (*A*) of 490.65 x10^{-6} m^2.

Conditions	*L* x10^{-5} (m)	*m* x10^{-4} *(Kg)*	ε (%)
$P_{15}T_{55}Pl_0$	6	12.69	62.22
$P_{15}T_{54}Pl_1$	6.9	11.35	76.06
$P_{15}T_{50}Pl_5$	8	14.37	79.69

5.2.4. Membrane surface charge

Membrane surface charge measurements showed a shift of the zeta-potential to a more negative value with increasing Plu content (seen in Figure 5.28). This observation supports the explanation provided earlier for the availability of Plu groups on the membrane surface and their influence on increasing the membrane hydrophilicity by increasing its surface charge density.

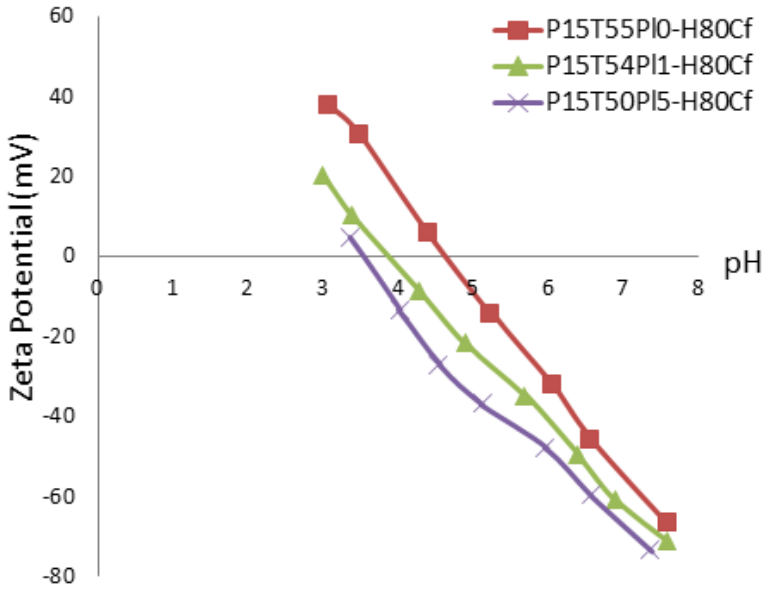

Figure 5.28: Membrane surface charge for samples of increasing Plu concentration

5.3. TFNC support-membrane testing

5.3.1. Microfiltration fouling

In Figure 5.29, samples exposed to humidity under forced convection were investigated for the effect of membrane morphology on RFR% under microfiltration processes using polystyrene beads (LB3) with an average particle diameter of 297.1 nm (represented in Figure 5.30). $P_{15}T_{55}Pl_0$-$H_{30}C_f$ membranes had the highest reduction in flux after 60 min of filtration reaching ≈18% of the initial value. This agreed with the large average pore size of this membrane as compared to others. Thus, LB3 preferentially accumulates on top-of or inside the membrane surface pores. As a consequence, flux recovery was the lowest due to the accumulation inside the membrane matrix and the LB3 entrapment seemed irreversible under the adopted cleaning procedure. The SEM image in Figure 5.31 provides a visualization of LB3 aggregates in the cross section near to the membrane top surface of $P_{15}T_{55}Pl_0$-$H_{30}C_f$. Increasing the RH degree of exposure decreased the pore size, and as well, the percent reduction in flux.

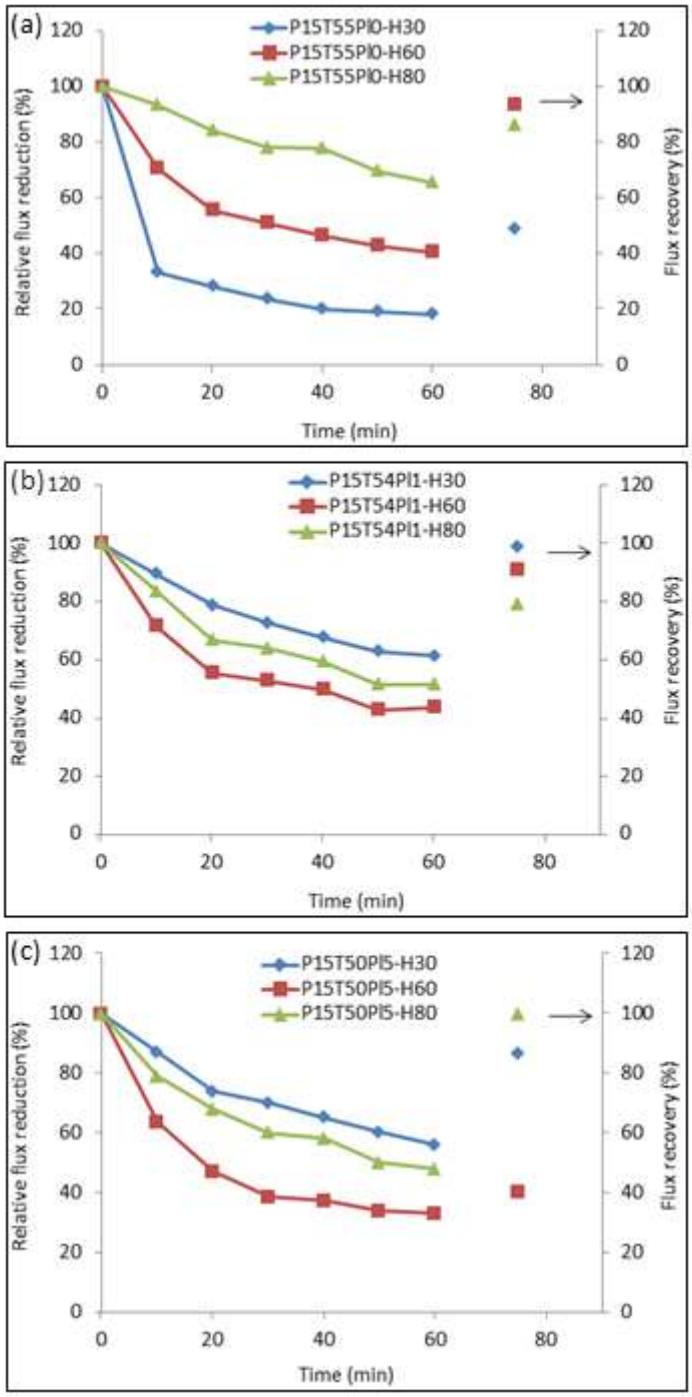

Figure 5.29: RFR % and recovery % using LB3 on membrane samples of (a) $P_{15}T_{55}Pl_0$, (b) $P_{15}T_{54}Pl_1$ and (c) $P_{15}T_{50}Pl_5$ at different RH exposure

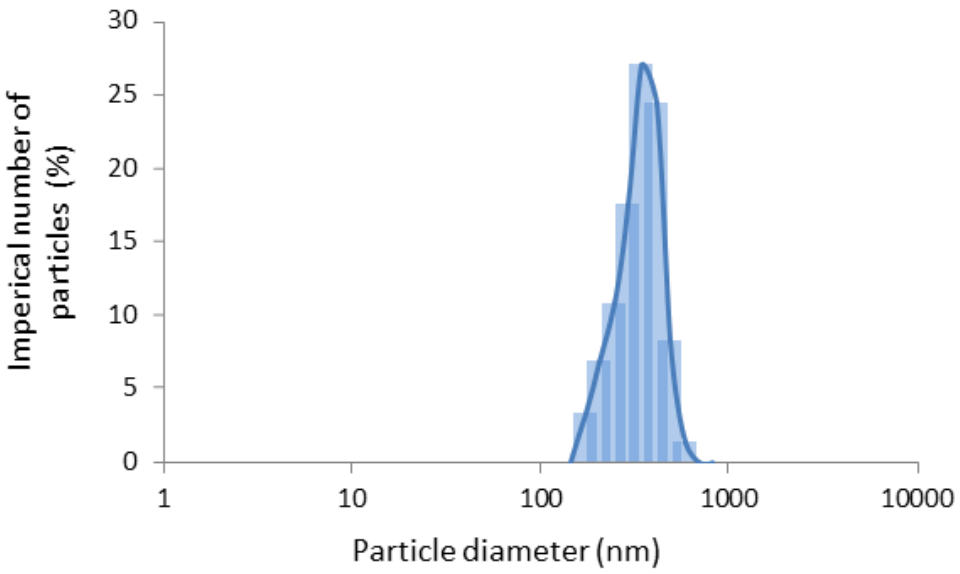

Figure 5.30: Particle size distribution result of 100 ppm LB3 solution

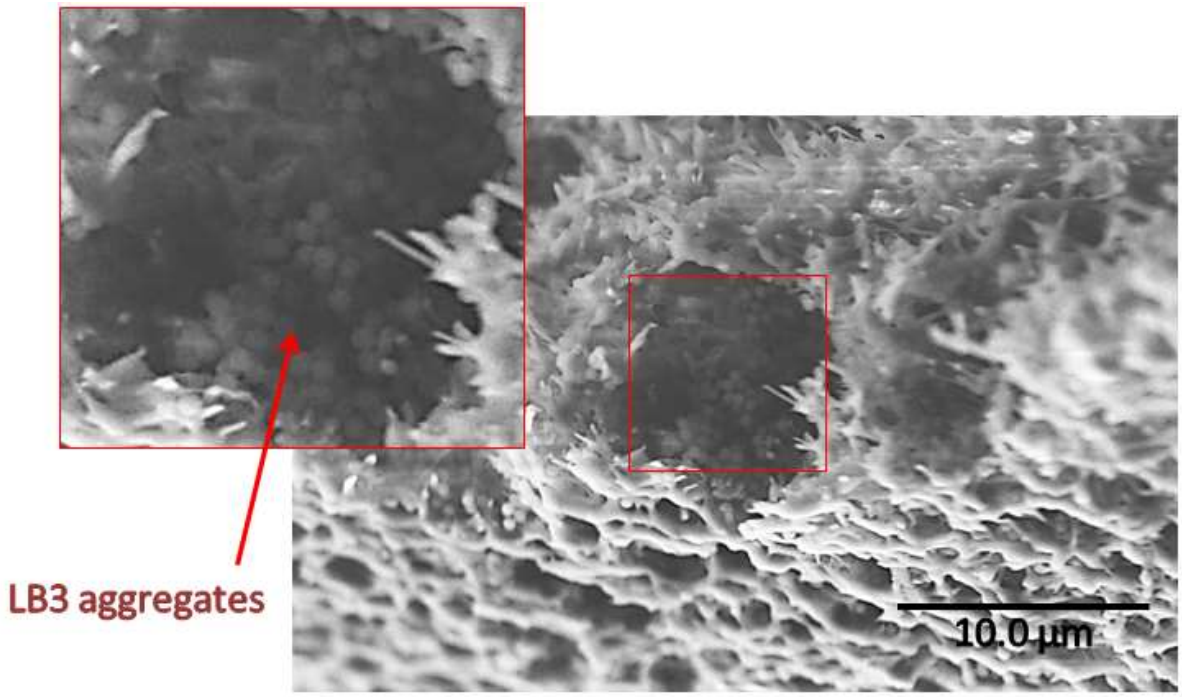

Figure 5.31: SEM micrograph of $P_{15}T_{55}Pl_0$-$H_{30}C_f$ showing LB3 aggregates inside the membrane large pores near the top surface

As $P_{15}T_{54}Pl_1$ membrane prepared at 30% RH had smaller mean flow pore diameter, it showed the highest recovery of almost 99%. Surface hydrophilicity as shown from contact angle measurement and hindrance of depth accumulation due to small pore diameter (see Table 5.1) were responsible for this behavior. Similarly, 30% RH exposure had the highest performance among all $P_{15}T_{55}Pl_5$ samples owing to its structure. Both membranes at 60 and 80% RH had higher reduction and lower recovery. Due to the higher entrapment of LB3 in their matrix, back flushing of both was not enough to flush out the LB3 trapped inside the

membranes matrices. However, at 80% RH the smaller pore size reflected the slightly better performance (Figure 5.29 (b,c)).

Generally, the addition of Pluronic increased bulk hydrophilicity. Figure 5.32 compares the cross-section images of two membranes with comparable mean flow pore diameter (≈183 nm). However, they have different compositions ($P_{15}T_{55}Pl_0$-$H_{60}C_f$ and $P_{15}T_{50}Pl_5$-$H_{80}C_f$), and hence, different bulk hydrophilicity. As LB3 are hydrophilic in nature, images show LB3 beads diffusing all over the cross-section (Figure 5.32 (a,c)) with the membrane of high bulk hydrophilicity ($P_{15}T_{50}Pl_5$-$H_{80}C_f$). On the contrary, $P_{15}T_{55}Pl_0$-$H_{30}C_f$ membrane sample shows LB3 beads only on the top surface. It is however worth mentioning that the diffusion of LB3 through membrane versus its accumulation on the membrane surface did not show a negative effect on recovery. This is ascribed to the facilitated backwash of entrapped LB3 in case of membranes with higher bulk hydrophilicity.

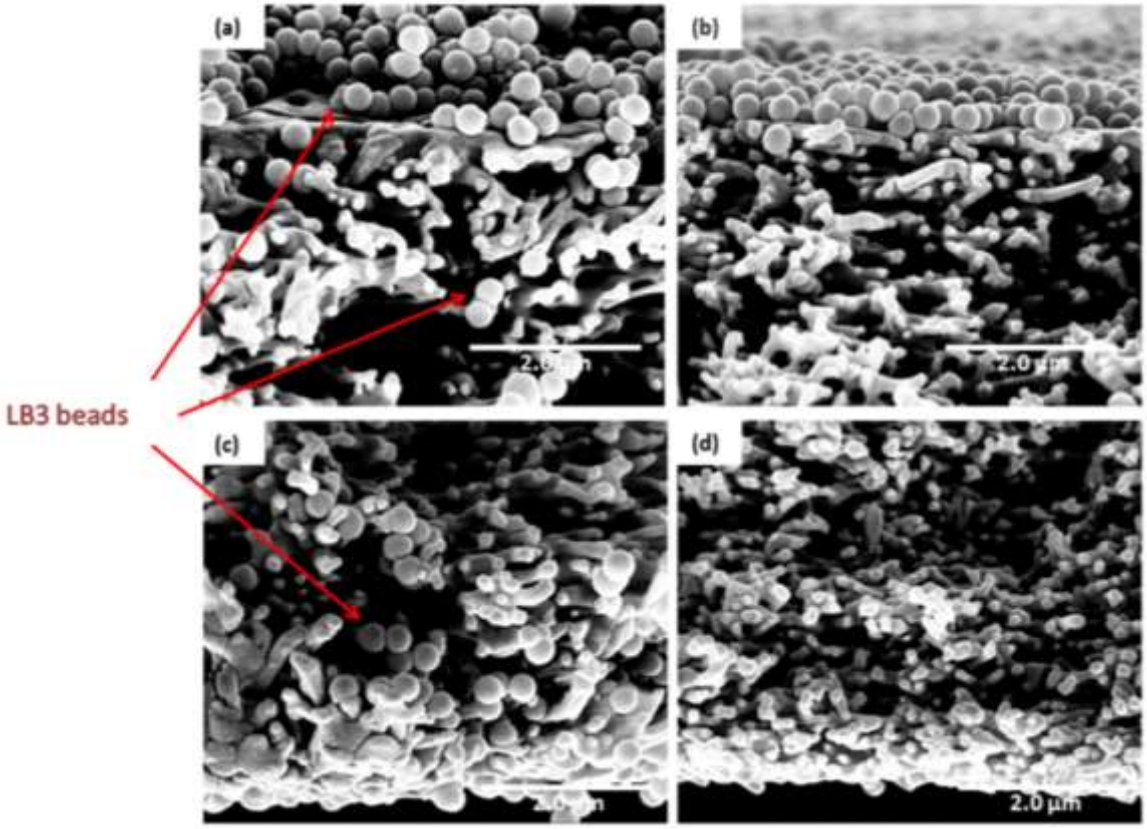

Figure 5.32: SEM micrographs of $P_{15}T_{50}Pl_5$-$H_{60}C_f$ and $P_{15}T_{55}Pl_0$-$H_{80}C_f$ showing cross section near top surface (a, b) and near bottom surface (c, d), respectively

Interestingly, further to the addition of 1wt% Plu, the membranes at 60 and 80% RH exposure had lower RFR% as compared with $P_{15}T_{55}Pl_0$ samples under the same conditions. Knowing that all RFR runs were conducted under isobaric condition, one shall assume that higher quantity of LB3 passed through $P_{15}T_{54}Pl_1$ at the same period of time compared to their complementary $P_{15}T_{55}Pl_0$ samples. However, the increased hydrophilicity is the reason for such decrease in RFR value. For instance, at 60% RH with pore size of 242 nm for

$P_{15}T_{54}Pl_1$ and 183 nm for $P_{15}T_{55}Pl_0$, the successful trade-off with Plu addition diminished the expected negative effect of larger pore diameter. As the increased bulk hydrophilicity hindered the attachment of LB3 to the membrane inner matrix and the beads washing-out was relatively easier.

Comparably, at 80% RH, 1wt% Plu composition showed inferior performance despite of its mean pore diameter of 154 nm versus 219 nm in case of 5wt%. While as $P_{15}T_{50}Pl_5$ had 42.2% larger pore size than $P_{15}T_{55}Pl_1$, the hydrophilicity compensated this factor and the flux reduction was approximately similar for both with higher recovery of $P_{15}T_{54}Pl_5$.

Cyclic filtration runs were conducted to evaluate the membrane recovery performance. As represented in Figure 5.33, $P_{15}T_{55}Pl_0$-$H_{80}C_f$ membrane samples showed better performance than $P_{15}T_{55}Pl_0$-$H_{60}C_f$ due to the relatively smaller average pore diameter that concluded to lower degree of LB3 beads entrapment. Accordingly, the cumulative loss in performance was relatively lower than that observed for $P_{15}T_{55}Pl_0$-$H_{60}C_f$ membrane samples.

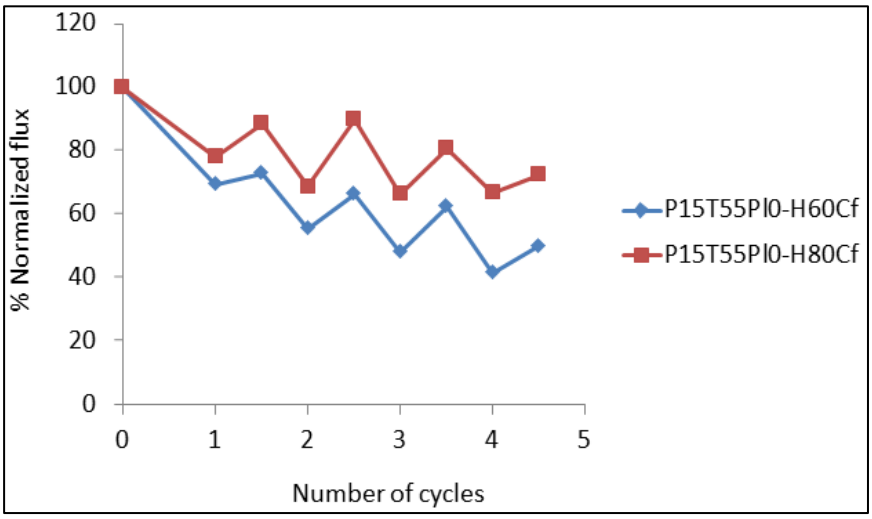

Figure 5.33: LB3 cyclic filtration curves for membrane samples of $P_{15}T_{55}Pl_0$ prepared at 60% and 80% RH under forced convection

Similar behavior was observed with $P_{15}T_{54}Pl_1$ and $P_{15}T_{50}Pl_5$ samples, where membranes prepared at 80% RH showed better performance than those prepared at 60% RH. This agrees with the observation in the preceding paragraph that the decrease in average pore diameter with the increase in RH degree of exposure, resulted in lower degree of LB3 beads entrapment; and accordingly, better performance. Furthermore, all samples that incorporated Plu in its structure (Figure 5.34) demonstrated better performance than that of $P_{15}T_{55}Pl_0$ samples (Figure 5.33). However, increasing Plu content from 1 wt% to 5 wt% did not show significant improvement in membrane performance. This is believed to be due to the antagonistic factors that interplay with increasing membrane Plu content.

It was observed earlier that increasing membrane Plu content not only increased the membrane average pore diameter, but also increased membrane wettability and bulk

hydrophilicity. Thus, considering that cyclic filtration is affected by both factors, it is expected that the increase in the average pore size would negatively affect the cyclic filtration performance. On the contrary, increasing membrane bulk hydrophilicity should improve the cyclic filtration performance. Subsequently, both factors nearly demolish the significance of increasing membrane Plu content and samples of 1 wt% and 5 wt% Plu demonstrated comparable performance.

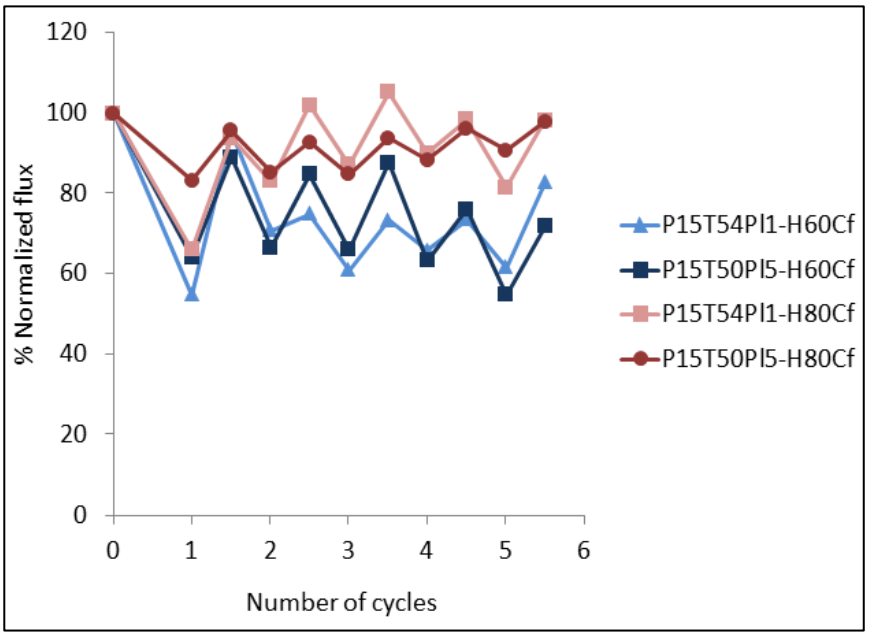

Figure 5.34: LB3 cyclic filtration curves for membrane samples of $P_{15}T_{54}Pl_1$ and $P_{15}T_{50}Pl_5$ prepared at 60% and 80% RH

5.3.2. Compaction resistance performance

TFC membranes are made of thin PA layer supported by the underlying membrane that typically has an asymmetric morphology. The asymmetry of the support layer is essential so that the skin layer could effectively stabilize the integrity of the top PA thin film. However, the inner structure of the support layer is of great influence on the overall membrane performance, including the membrane fouling resistance and mechanical stability. Accordingly, our motivation to improve membrane lifetime was through increasing the support layer hydrophilicity and mechanical strength; yet, maintaining the availability of the support membrane skin surface.

In a previous section, we have demonstrated the adopted conditions to fabricate the semi-symmetric structure. Further to that, semi-symmetric structure showed superior bulk hydrophilicity as compared to isotropic structure of same composition. Thus, in order to achieve the one of the main objectives of our study, the compaction resistance was tested to compare semi-symmetric to asymmetric support layer. $P_{15}T_{55}Pl_0$ solution was used to prepare semi-symmetric and asymmetric support layers tailored by modifying the fabrication conditions. As shown in Table 5.5, the initial hydraulic permeability of the support layer with semi-symmetric cross-section was higher by 12% due to its thinner skin

thickness. Furthermore, as demonstrated in Figure 5.35, the semi-symmetric membrane had lower permeability loss under compaction and higher recovery value when pressure was released. This indicated that the semi-symmetric structure would be a better substitute to the typical asymmetric support membranes in TFC membrane formation.

Table 5.5: Hydraulic permeability of membranes with different cross-sectional morphology using $P_{15}T_{55}Pl_0$ solution

Conditions	Cross-sectional structure	J_w (L/m2.hr.bar)		
		Initial (J_0)	Compacted at 1 bar (J_c)	Recovery (J_r)
30% RH-Free convection for 1 min	Semi-symmetric	1732	1581 (91.3%)	1628 (94%)
LIPS	Asymmetric	1520	1345 (88.5%)	1374 (90.4%)

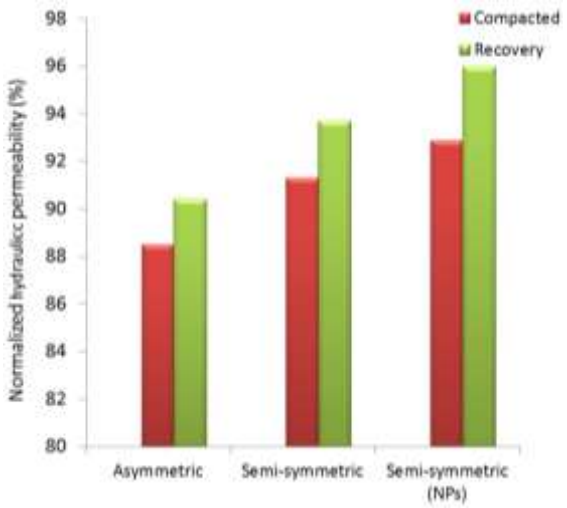

Figure 5.35: The hydraulic permeability of compacted asymmetric and semi-symmetric membranes of same composition and semi-symmetric nanocomposite membranes and their recovery after pressure release for one cycle

On the other hand, the addition of NPs did not show a significant increase in compaction resistance. Still, slight improvement was observed where the semi-symmetric membrane containing NPs at 0.1 wt% was tested as represented in Table 5.6.

Table 5.6: Hydraulic permeability before and after compaction of membranes with and without NPs, as well as, the permeability recovery after pressure release

Membrane	Cross-sectional structure	J_w (L/m2.hr.bar)			
		Initial (J_0)	Compacted at 1 bar (J_c)	Recovery (J_r)	
$P_{15}T_{55}Pl_0$-$H_{30}C_0$	Semi-symmetric	1732	1581 (91.3%)	1628	(94%)
$P_{15}T_{54.9}N_{0.1}$-$H_{30}C_0$	Semi-symmetric	1939	1801 (92.9%)	1861	(96%)

5.4. TFNC performance

To fabricate a stable TFC membrane, the support layer surface has to have a relatively small pore diameter to effectively support the thin PA layer on top of it. That is why most of the TFC commercial membranes have an asymmetric support layer. Because the skin layer of the asymmetric support membrane maintains high stability for the PA layer upon applying pressure during operation [161,163]. On the other hand, it is preferable for the support layer to have low resistance to water flow in order not to decrease TFC membrane flux. Thus, support membrane hydrophilicity, average pore diameter and skin layer thickness are quite important to be considered in order to have efficient TFC membrane [161,168,169]. For instance, interfacial polymerization process for PA formation might take place inside the pore if the diameter is wide enough. Hence, no solute rejection would be noticed for the TFC membrane because of the PA layer defects (as shown in Figure 5.36). Also, even if the PA formed an intact film it might be broken when high pressure is applied. Accordingly, support membranes with relatively small pore diameter or that comprise a skin layer are preferred for TFC fabrication.

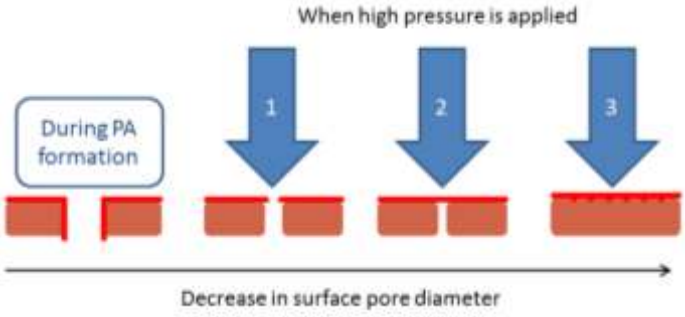

Figure 5.36: Schematic presentation of the importance of the support layer surface pore diameter

TFC membrane samples were prepared using various support layers. In order to study the influence of the support layer structure, a PA thin layer was applied to asymmetric and semi-symmetric support membranes of comparable composition. Afterwards, FTIR spectroscopy measurements were done to verify the PA synthesis. As seen in Figure 5.37, the FTIR spectra of the $P_{15}T_{50}Pl_5$-$H_{30}C_0$ support membrane shows the characteristic peaks of PES. The strong transmittances appear at 1151 cm^{-1} for SO_2 bond stretching, 1244 cm^{-1} for ether bond vibration and 1490 cm^{-1} for C-S vibration [200]. The macromolecular hydrophilic additive (Plu) did not show a characteristic peak. However, the transmittance at 1105 cm^{-1} is a combined effect of C-O bond stretching in both PES and Plu (schematically presented in Figure 5.38) [93]. The TFC membrane showed characteristic peaks for PA layer. This included the appearance of aromatic amine bonds stretching at 1240, 1290 and 1320 cm^{-1}. Also, amide bonds stretch vibrations appeared at 1680 cm^{-1}.

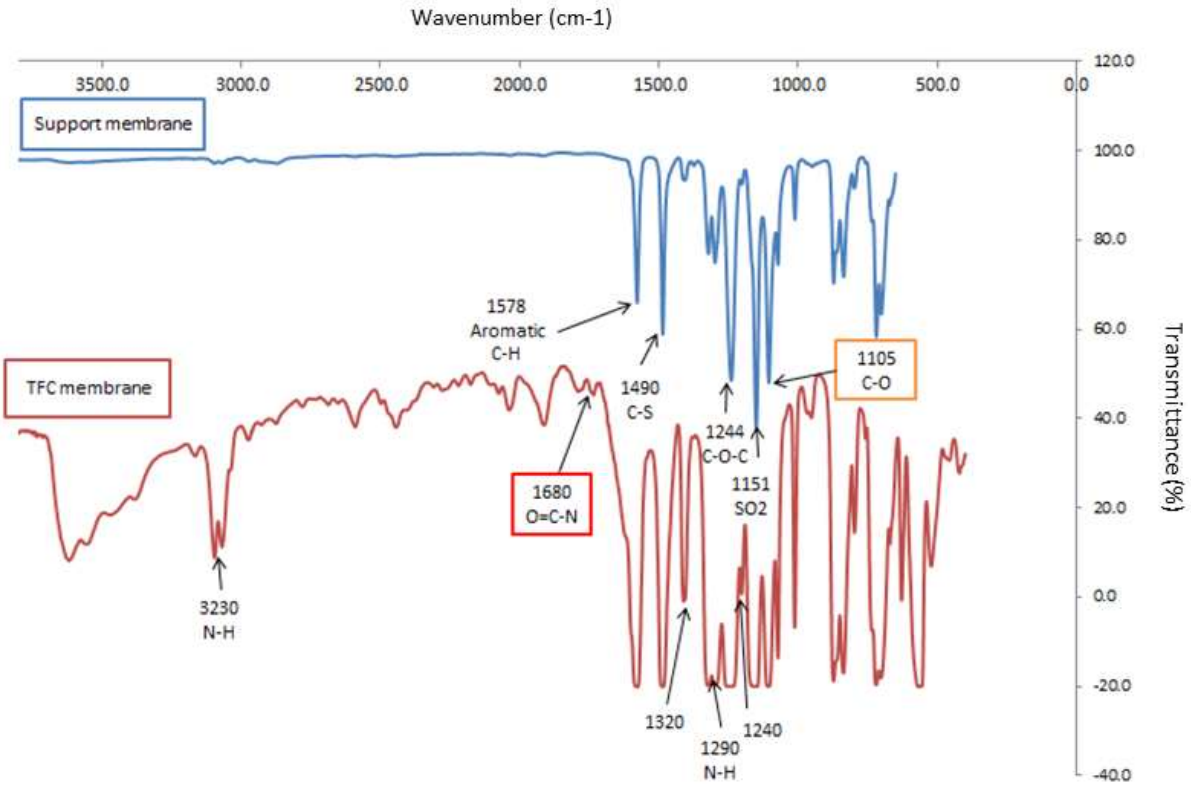

Figure 5.37: Comparison of representative FTIR spectra of the support membrane $P_{15}T_{50}Pl_5$-$H_{30}C_0$ and its TFC membrane (after applying the PA layer)

As per the results showed in Table 5.7, substituting the asymmetric support with the semi-symmetric support increased the TFC permeability by 8.01%, yet, salt rejection was not significantly altered. This increased permeability is owing to the thinner skin layer of the semi-symmetric structure. On the other hand, the thin skin layer could still effectively support the applied PA with the same competence as seen in Figure 5.39.

Further to that, semi-symmetric supports of increasing Plu content were used to prepare TFC membranes. The TFC of the support membrane $P_{15}T_{54}Pl_1$-$H_{30}C_0$ had higher permeability and lower salt rejection compared to that of $P_{15}T_{50}Pl_5$-$H_{30}C_0$ support membrane. This is due to the higher surface porosity of $P_{15}T_{54}Pl_1$-$H_{30}C_0$ support membrane skin layer. This increased surface porosity increased the permeability and poorly supported the PA layer. Thus, defects on the PA layer might have been formed, hence, the salt rejection decreased.

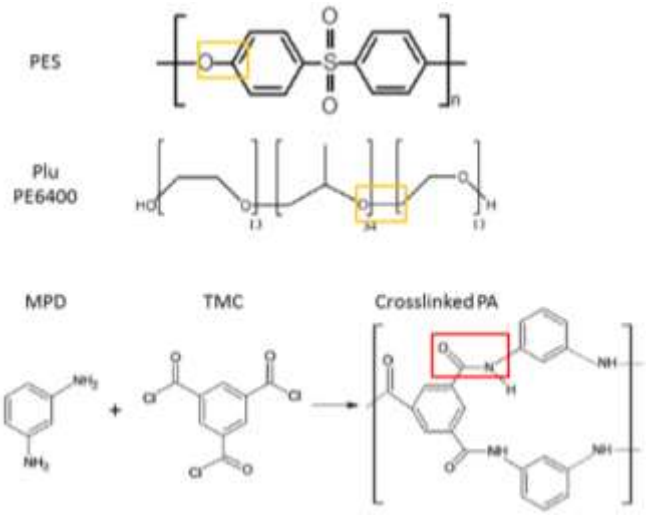

Figure 5.38: Schematic presentation of chemical structures of PES, Plu and PA [94,200]

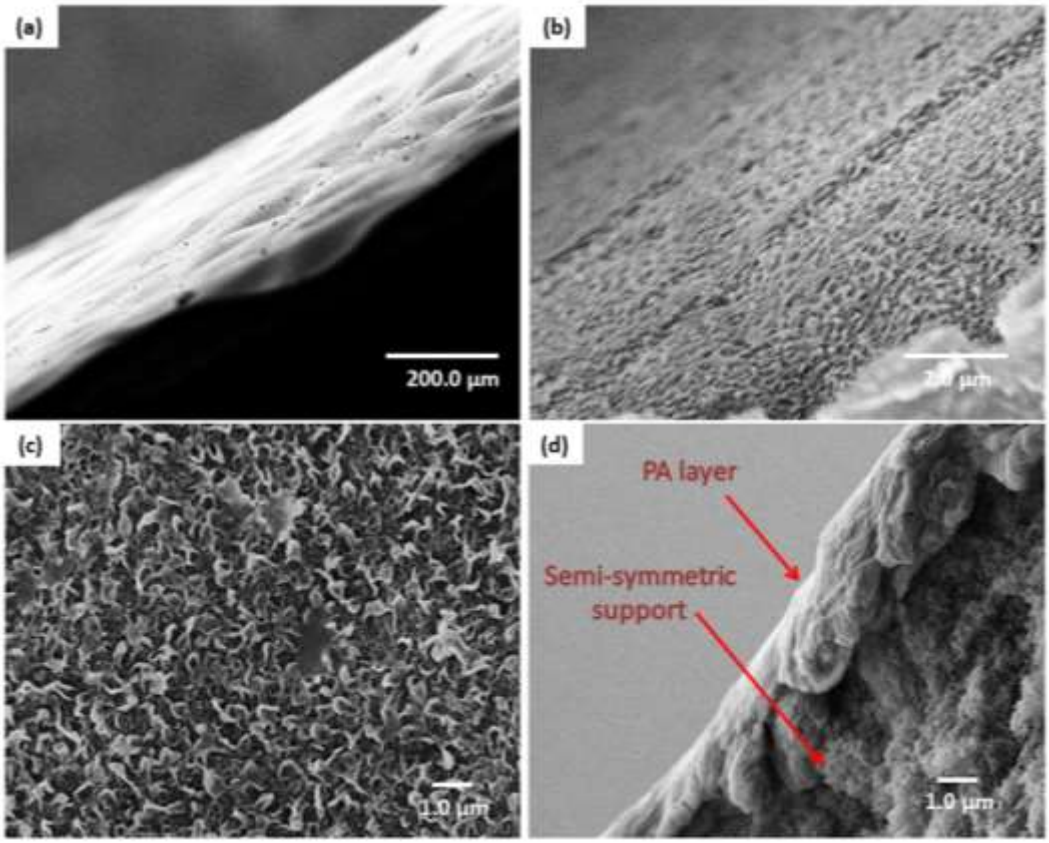

Figure 5.39: SEM micrographs showing the (a) top side view, (b) focus on top surface and (c) top surface, (d) top cross section of TFC membrane based on $P_{15}T_{55}Pl_0$-$H_{30}C_0$ semi-symmetric support

On the other hand, TFNC membranes were prepared using the semi-symmetric nanocomposite support layers as seen in Figure 5.40. Nanoparticles introduction showed an

increase in the membrane permeability. Support layers containing 0.05 wt% and 0.1 wt% TiO_2 increased the permeability by 4.46% and 26.77%, respectively as represented in Table 5.7.

Table 5.7: TFC membranes water flux, rejection and salt permeability based on different support membranes

Support membrane	Support membrane structure	Permeability (L/m2.hr.bar)	Permeability enhancement[a] (%)	Rejection (%)
$P_{15}T_{45}PI_0$-$H_{30}C_0$	Asymmetric	0.907 ± 0.08	0	91.43
$P_{15}T_{55}PI_0$-$H_{30}C_0$	Semi-symmetric	0.986 ± 0.06	9	91.73
$P_{15}T_{54}PI_1$-$H_{30}C_0$	Semi-symmetric	1.77 ± 0.24	95	89
$P_{15}T_{50}PI_5$-$H_{30}C_0$	Semi-symmetric	1.051 ± 0.12	16	93.47
$P_{15}T_{54.95}N_{0.05}$-$H_{30}C_0$	Semi-symmetric	1.03 ± 0.072	14	92.53
$P_{15}T_{54.9}N_{0.1}$-$H_{30}C_0$	Semi-symmetric	1.25 ± 0.053	38	91.64

[a] *Permeability enhancement was calculated as percentage increase in permeability in respect to the permeability of TFC membrane prepared using asymmetric support layer.*

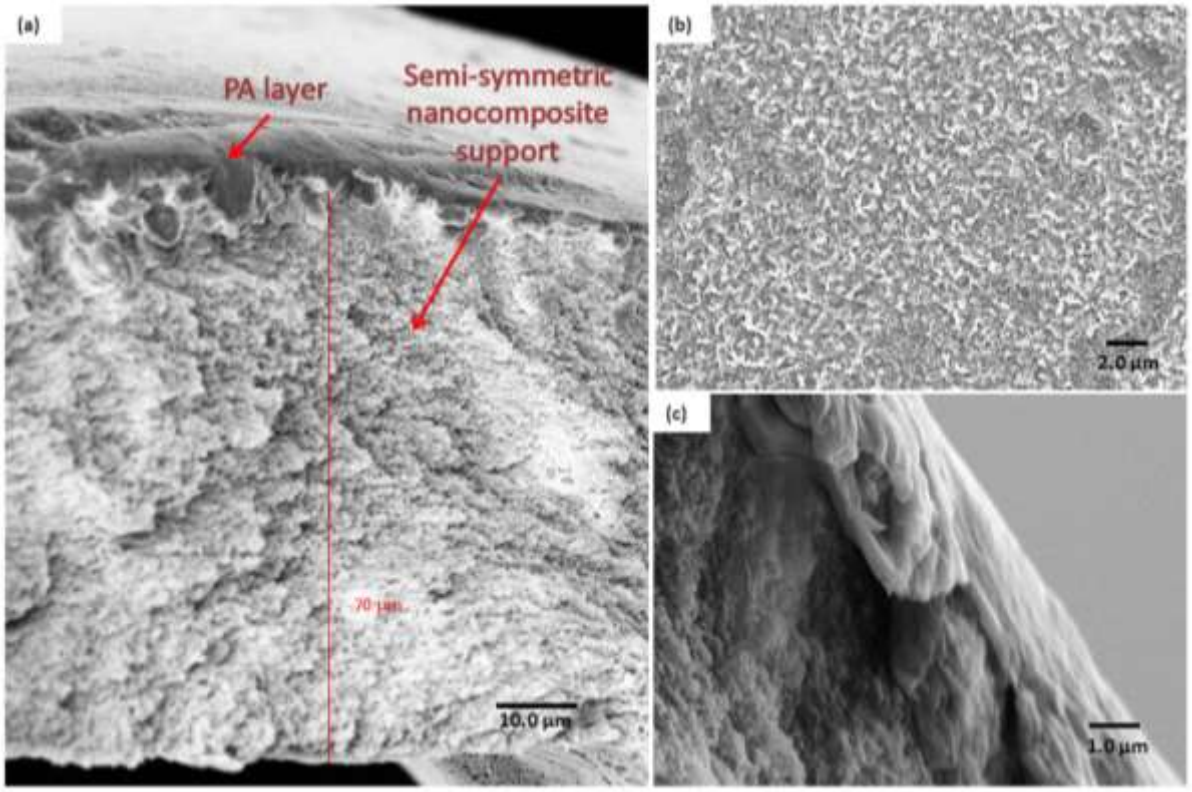

Figure 5.40: SEM micrographs showing the (a) cross section, (b) focus on top surface, and (c) top cross section of TFNC membrane based on $P_{15}T_{54.9}N_{0.1}$-$H_{30}C_0$ semi-symmetric support

Chapter 6

Conclusions and Outlook

Chapter 6 : Conclusions and Outlook

The further advancement of membrane desalination technology relies on the membrane durability and performance. The current challenge for such a sustainable process is increasing the membrane lifetime without compromising its permeability and salt rejection. In this study, the development of TFNC support layer tackled both challenges through increasing the membrane compaction resistance and hydrophilicity. In this study we showed different approaches to tailor the TFNC membrane support-layer structure and properties. Those approaches included the RH degree at exposure, exposure time and convection condition. The convection condition during VIPS process was found to be highly influential on the cast solution thermodynamics. Thus, a relatively new membrane cross sectional morphology was revealed upon fine tuning of the process parameters, which is the semi-symmetric morphology.

In the process of developing high performance TFNC support layer, hydrophilic additives were incorporated to increase the membrane throughput. Two types of additives were studied, a hydrophilic block copolymer (Plu) and inorganic nanoparticles (TiO_2). H^1NMR analysis was used to study the degree of entrapment of Plu in the final membrane structure which was significantly affected by the fabrication process. In addition, contact angle measurements and wettability were used for a comparative study of the hydrophilicity enhancement by NPs versus Plu. Also, for Plu containing membranes, microfiltration fouling experiments were conducted to reveal the fouling resistance to polystyrene beads.

Further to that, cast solutions with different compositions were tailored to yield semi-symmetric membranes to serve as a TFNC support layer. SEM imaging and the capillary flow porometer were used to study the effect of VIPS parameters on membrane final morphology. Based on the results presented in this study, the TFC support layer with semi-symmetric morphology holds various advantages when compared with its asymmetric counterpart. The semi-symmetric structure showed higher hydraulic permeability without compromising the PA layer supporting property. Furthermore, the semi-symmetric membranes had higher compaction resistance and higher recovery percentages enduring high pressure applications.

The introduction of TiO_2 nanoparticles further increased the hydraulic permeability and compaction resistance of the semi-symmetric support. Although, NPs addition changed the cast solution thermodynamic properties, we were successful in tailoring the process conditions to obtain the semi-symmetric structure based on the previous practice using Plu.

Finally, for future perspective some complimentary work can be suggested as follows:

- Further study of the thermodynamic states of the solution under VIPS/NIPS combined process using dynamic Fourier transform infrared and cloud point measurements.

- Studying the influence of different hydrophilic additives to obtain the semi-symmetric structure and further improve it.
- Optimization of the PA thin film application on the semi-symmetric support to enhance its salt rejection.
- Investigating long term RO performance of TFNC based on semi-symmetric support.
- Scaling up of the fabricated TFNC and undertake a comparative study with currently available commercial TFC.

References:

1 Vital water graphics - an overview of the state of the world's fresh and marine waters. 2nd edition. *United Nations Environmental Programme*, (2008). Adapted from: <http://www.unep.org/dewa/vitalwater/index.html>, accessed on July 2015.

2 Progress on drinking water and sanitation: special focus on sanitation, *World Health Organization,* (2008). Adapted from: <http://www.who.int/water_sanitation_health/monitoring/jmp2008/en/>, accessed on July 2015.

3 World health statistics. *World Health Organization*, (2008)b. Adapted from: <http://www.who.int/whosis/whostat/2008/en/>, accessed on July 2015.

4 UN water fact sheets. *United Nations Educational, Scientific, and Cultural Organization*, (2013). Adapted from: <http://www.unwater.org/water-cooperation-2013/water-cooperation/facts-and-figures/en/>, accessed on July 2015.

5 Water and energy, *World Water Assessment Programme*, (2014). Adapted from: <http://www.unesco.org/new/en/natural-sciences/environment/water/wwap/wwdr/2014-water-and-energy/>, accessed on July 2015.

6 Facing the challenges, *World Water Assessment Programme*, (2014). Adapted from: < http://www.unesco.org/new/en/natural-sciences/environment/water/wwap/wwdr/2014-water-and-energy/ >, accessed on July 2015.

7 Water in a changing world, *World Water Assessment Programme*, (2009). Adapted from: <http://www.unesco.org/new/en/natural-sciences/environment/water/wwap/wwdr/wwdr3-2009-> , accessed on July 2015.

8 Managing water for all, *Organization for Economic Cooperation and Development,* (2009). Adapted from: <http://www.oecd.org/env/resources/managingwaterforallanoecdperspectiveonpricingandfinancing.htm> accessed on July 2015.

9 World population prospects. Population Division Database. Detailed Indicators-2015 Revision, *United Nations Department of Economic and Social Affairs* (2013a). Adapted from: < http://esa.un/undp/wpp/Publications/ > accessed on June 2015,

10 Annual report, *United Nations-Habitat*, (2010). Adapted from: < http://unhabitat.org/un-habitat-annual-report-2010/ > accessed on July 2015.

11 Water for food security and nutrition, *High Level Panel of Experts on Food Security and Nutrition*, (2015). Adapted from: < http://www.fao.org/cfs/cfs-hlpe/en/ > accessed on July 2015.

12 Batisha, A.F. Water desalination industry in Egypt, *Eleventh International Water Technology Conference*, Sharm El-Sheikh, Egypt Jan. 2007.

13 Fahim M. A.; Hassanein M. K.; Khalil A. A.; Abou Hadid A. F. Climate change adaptation needs for food security in Egypt, *Nature and Science* **12**, 68-74 (2013).

14 Adaptation to Climate-change Induced Water Stress in the Nile Basin: A Vulnerability Assessment Report, *United Nations Environment Programme* (2013), Adapted from: <http://www.unep.org/dewa/assessments/EcoSystems/water>, accessed on July 2015.

15 Youssef, R.M.; Sakr, M.L.; Shakweer, A.F. Desalination Technology Roadmap 2030, *The Cabinet Information and Decision Support Center*, Egypt 2007.

16 Osman, G. DESERTEC Cost Analysis and Economic Impact Assessment, *World Wind Energy Association,* (2011). Adapted from: < http://www.esi-africa.com/wp-content/uploads/Galal_Osman.pdf > accessed on July 2015.

17 Ettouney, H. Design & Analysis of humidification dehumidification desalination process II, *Desalination*, **183,** 341-352 (2005).

18 Saidur, R.; Elcevvadi, E.T.; Mekhilef, S. An overview of different distillation methods for small scale applications. *Renew. Sust. Energ. Rev.* **15**, 4756-4764 (2011).

19 Müller-Holst H. Solar thermal desalination using the multiple effect humidification (MEH) method. Solar Desalination for the 21st Century. 215–25 (2007).

20 Energy options for water desalination in selected ESCWA member countries. *United Nations. Economic and Social Commission for Western Asia*. (2001).

21 Ulbricht,M. Advanced functional polymer membranes, *Polymer*, **47,** 2217-2262 (2006).

22 Wang, Y.; Kim, J.-H.; Choo, K.-H.; Lee, Y.-S.; Lee, C.-H. Hydrophilic modification of polypropylene microfiltration membranes by ozone-induced graft polymerization, *J. Membr. Sci.*, **169(2)**, 269-276 (2000).

23 Lee, H.J.; Safert, F.; Strathmann, H.; Moon, S.H. Designing of an electrodialysis desalination plant, *Desalination*, **142**, 267-286 (2002).

24 Karaghouli, A.; Kazmerski, L. Energy consumption and water production cost of conventional and renewable-energy-powered desalination processes. *Renew. Sust. Energ. Rev.* **24**, 343-356 (2013)

25 Energy Makes All the Difference: Desalination Operating Costs Compared - Chart, *Global Water Intelligence*, 8 (2007). Adapted from: < https://www.globalwaterintel.com/global-water-intelligence-magazine/8/2/uncategorized/chart-of-the-month > accessed on July 2015.

26 Loupasis s. Technical analysis of existing renewable energy driven desalination schemes. *Commission of the European Communities, Directorate General for Energy and Transport*, (2001).

27 Lachish U. Osmosis and thermodynamics. *Am. J. Phys.* **75(11**). 997 – 998 (2007).

28 Semiat R. Energy issues in desalination processes. *Environ. Sci. Technol.* **42**,8193-8201 (2008).

29 Karagiannis, I.C.; Soldatos, P.G. Water desalination cost literature: review and assessment. *Desalination*. **223**, 448-456 (2008).

30 Jaber, I.S.; Ahmed M.R. Technical and economic evaluation of brackish groundwater desalination by reverse osmosis (RO) process. *Desalination* **165,** 209-213 (2004).

31 Mohamed E.S.; Papadakis, G.; Mathioulakis, E.; Belessiotis, V. The effect of hydraulic energy recovery in a small sea water reverse osmosis desalination system; experimental and economical evaluation. *Desalination* **184,** 241–246 (2005).

32 Borsani, R.; Rebagliati, S. Fundamentals and costing of MSF desalination plants and comparison with other technologies. *Desalination* **182,** 29–37 (2005).

33 Wu S. Analysis of water production costs of a nuclear desalination plant with a nuclear heating reactor coupled with MED processes. *Desalination* **190,** 287–294 (2006).

34 Al-Karaghouli, A.; Renne, D.; Kazmerski, L. Solar and wind opportunities for water desalination in the Arab regions. *Renew. Sust. Energ. Rev.* **13**, 2397–2407 (2009).

35 Mezher, T.; Fath, H.; Abbas, Z.; Khaled, A. Techno-economic assessment and environmental impacts of desalination technologies. *Desalination.* **266**, 263-273 (2011).

36 Nour-Eldin M. Untraditional water resources priorities survey. *Environment and Climate Change Research Institute*, Egypt; 2000.

37 Desalination in Addressing Water Scarcity. *Economic and Social Commission for Western Asia*, 2009. Retrieved from <http://www.escwa.un.org/information/pubaction.asp?PubID=620> accessed on July 2015.

38 Desalting projects report No. 17. *Wangnick Inventory*, 2002. Retrieved from <https://www.desalination.com/articles/11552> accessed on July 2015.

39 Camacho, L.; Dumee, L.; Zhang, J. Advances in Membrane Distillation for Water Desalination and Purification Applications. *Water*. **5,** 94-196 (2013).

40 Loeb, S.; Sourirajan, S. Sea Water Demineralization by Means of an Osmotic Membrane, in Saline Water Conversion–II, Advances in Chemistry Series Number 28, *Am. Chem. S.,* 117–132 (1963).

41 Cadotte, J.E.; Steuck, M.J.; Petersen, R.J. Research on in-situ-formed condensation polymers for reverse osmosis membranes, NTIS Report No. PB- 288387, loc. cit, 1978 (Mar).

42 Cadotte, J.E.; Cobian, K.E.; Forester, R.H.; Petersen, R.J. Continued evaluation of insitu-formed condensation polymers for reverse osmosis membranes, NTIS Report No. PB-253193, loc. cit, 1976 (Apr).

43 Adapted from <www.roplant.or.kr> accessed on February 2015.

44 Adapted from *Membrane sciences course* materials; M. Ulbricht presentation, 2013.

45 Membrane separation market, *Transparency Market Research* 2014. Adapted from: <http://www.transparencymarketresearch.com/membrane-separation-market.html> accessed on February 2015.

46 Kesting, R.E., Synthetic Polymeric Membranes, *John Wiley & Sons*, New York (1985)

47 Mulder, M. Basic Principles of Membrane Technology, *Kluwer Academic Publishers*, (1996).

48 Van de Witte, P.; Dijkstra, P.J.; Van den Berg, J.W.A.; Feijn, B.J. Phase separation processes in polymer solutions in relation to membrane formation, *J. Membr. Sci.* **117,** 1 (1996).

49 Park, H.C.; Kim, Y.P.; Kim, H.Y.; Kang, Y.S. Membrane formation by water vapor induced phase inversion, *J. Membr. Sci.* **156,** 169 (1999).

50 Abu Tarboush, B.J.; Rana, v.; Matsuura, T.; Arafat, H.A.; Narbaitz, R.M., Preparation of thin-film-composite polyamide membranes for desalination using novel hydrophilic surface modifying macromolecules, *J. Membr. Sci.* **325,** 166–175 (2008).

51 Liu, N.A.; Hashim, Y.T.; Abed, M.R.M.; Li, K. Progress in the production and modification of PVDF membranes, *J. Membr. Sci.* **375**, 1–27 (2011).

52 Zsigmondy, R.; Bachmann, W.Z. “Uber Neue Filter”, *Z. Anorg. U. Allgem. Chem.* ***103***, 119–128 (1918).

53 Elford, W.J. Principles governing the preparation of membranes having graded porosities. The properties of ‘gradocol’ membranes as ultrafilters, *Trans. Faraday Soc.* **33**, 1094–1104. (1937).

54 Yip, Y.; McHugh, A.J. Modeling and simulation of nonsolvent vapor-induced phase separation, *J. Membr. Sci.* **271,** 163–176 (2006).

55 Wang, Q.; Wang, Z.; Wu, Z. Effects of solvent compositions on physicochemical properties and anti-fouling ability of PVDF microfiltration membranes for wastewater treatment, *Desalination* **297,** 79–86 (2012).

56 Peng, Y.; Fan, H.; Dong, Y.; Song, Y.; Han, H. Effects of exposure time on variations in the structure and hydrophobicity of polyvinylidene fluoride membranes prepared via vapor-induced phase separation”, *Appl. Surf. Sci.* **258**, 7872–7881 (2012).

57 Shin, S.J.; Kim, J.P.; Kim, H.J.; Jeon, J.H.; Min, B.R. Preparation and characterization of polyethersulfone microfiltration membranes by a 2-methoxyethanol additive, *Desalination.* **186**, 1–10 (2005).

58 Bikel, M.; Punt, I.G.M.; Lammertink, R.G.H.; Wessling, M. Micropatterned polymer films by vapor-induced phase separation using permeable molds, *ACS Appl. Mater. Interfaces.* **12**, 2856–2861 (2009).

59 Giron`es, M.; Akbarsyah, I.J.; Nijdam, W.; van Rijn, C.J.M.; Jansen, H.V., Lammertink, R.G.H., Wessling, M. Polymeric microsieves produced by phase separation micromolding, *J. Membr. Sci.* **283**, 411–424 *(*2006).

60 Khayet, M.; Garc´ıa-Payo, M. C.; Qusay, F.A.; Khulbe, K.C.; Feng, C. Y.; Matsuura, T. Effects of gas gap type on structural morphology and performance of hollow fibers, *J. Membr. Sci.* **311**, 259–269 (2008).

61 Ulbricht, M.; Schuster, O.; Ansorge, W.; Ruetering, M.; Steiger, P. Influence of the strongly anisotropic cross-section morphology of a novel polyethersulfone microfiltration membrane on filtration performance, *Sep. Purif. Technol.* **57**, 63–73 (2007).

62 Watchanida, C.; Bouyer, D.; Pochat-Bohatier, C.; Deratani, A.; Dupuy, C. Effect of a drying pretreatment on morphology of porous poly(Ether-Imide) membrane prepared using vapor induced phase separation, *Dry. Technol.* **24 (10)**, 1317–1326 (2006).

63 Peng, N.; Chung, T. S.; Chng, M. L.; Aw,W. Evolution of ultra-thin dense-selective layer from single-layer to dual-layer hollow fibers using novel Extem R _ polyetherimide for gas separation, *J. Membr. Sci.* **360**, 48–57 (2010).

64 Li, C.L.; Wang D.M.; Deratani, A.; Quémener, D.; Bouyere, D.; Lai, J.Y. Insight into the preparation of poly(vinylidene fluoride) membranes by vapor-induced phase separation. *J. Membr. Sci.* **361,** 154–166 (2010).

65 Nguyen, Q.T.; Alaoui, Q.T.; Yang, H.; Mbareck, C. Dry-cast process for synthetic microporous membranes: Physico-chemical analyses through morphological studies. *J. Membr. Sci.* **358**, 13–25 (2010).

66 Michaels, A.S. High Flow Membrane, US Patent No. 3,615,024 (October, 1971).

67 Baker, R. Membrane Technology and Applications. Third Edition, *John Wiley & Sons*, (2012).

68 Smolders, C.A.; Reuvers, A.J. Formation of Membranes by Means of Immersion Precipitation, *J. Membr. Sci.*, 67-86 (1987).

69 Sterling, V.; Scnven, L.E. Interfacial turbulence Hydrodynamic stablhty and the Marangom effect. *AIChE. J*. **5,** 514 (1959).

70 Ray, R. J.; Kranz, W. B.; Sam, R. L. Linear stablhty theory model for finger formation 1s asymmetric membranes, *J. Membr. Sci.* **23,** 155 (1985).

71 Strathmann, H.; Kock, K.; Amar P.; Baker, R. W. The formation mechanism of asymmetric membranes, Desalination, **16,** 179 (1975).

72 Smolders, C.A.; Reuvers, A J.; Boom R.M.; Wienk I.M. Microstructures in phase-inversion membranes. Part 1. Formation of macrovoids. *J. Membr. Sci.* **73**, 259-275 (1992).

73 Wang, D.-M.; Lin, F.-C.; Wu, T.-T.; Lai, J.-Y. Formation mechanism of the macrovoids induced by surfactant additives, *J. Membr. Sci.* **142(2),** 191-204 (1998).

74 Di Luccio, M.; Nobrega, R.; Borges, C. P. Microporous anisotropic phase inversion membranes from bisphenol-A polycarbonate: study of a ternary system, *Polymer*, **41**, 4309–4315 (2000).

75 Barth, C.; Gonçalves, M.C.; Pires, A.T.N.; Roeder, J.; Wolf, B.A. Asymmetric polysulfone and polyethersulfone membranes: effects of thermodynamic conditions during formation on their performance. *J. Membr. Sci.* **169**, 287–299 (2000).

76 Lee H.J.; Jung, B.; Kang, Y. S.; Lee, H. Phase separation of polymer casting solution by nonsolvent vapor. *J. Membr. Sci.* **245,** 103–112 (2004).

77 Altinkaya, S.A.; Yenal, H. Ozbas, B. Membrane formation by dry-cast process Model validation through morphological studies. *J. Membr. Sci.* **249**, 163–172 (2005).

78 Sua, Y.S.; Kuo, C.Y.; Wang, D.M.; Lai, J.Y.; Deratani, A.; Pochate, C.; Bouyer, D. Interplay of mass transfer, phase separation, and membrane morphology in vapor-induced phase separation, *J. Membr. Sci.* **338**, 17–28 (2009).

79 Beysens, D.; Steyer, A.; Guenoun, P.; Fritter, D.; Knobler, C.M., How does dew form? *Phase Transitions*, **31**, 219-246 (1991).

80 Wenfang, L.U.; Zhiping, Z.; Lei, S.; Mingzhen, W. Formation of Polyethersulfone Film with Regular Microporous Structure by Water Vapor Induced Phase Separation. *Chin. J. Chem. Eng.* **18 (3)**, 150-157 (2010).

81 Peng, Y.; Fan, H.; Ge, J.; Wang, S.; Chen, P.; Jiang, Q. The effects of processing conditions on the surface morphology and hydrophobicity of polyvinylidene fluoride membranes prepared via vapor-induced phase separation. *Appl. Surf. Sci.* **263**, 737–744 (2012).

82 Hołda, K.; H.y Aernouts, B.; Saeys, W.; kelecom J. V. Study of polymer concentration and evaporation time as phase inversion parameters for polysulfone-based SRNF membranes. *J. Membr. Sci.* **442**, 196–205 (2013).

83 Hansen, C.M. Polymer science applied to biological problems: Prediction of cytotoxic drug interactions with DNA. *Eur. Polym. J.* **44,** 2741–2748 (2008).

84 Wei, Y.-M.; Xu, Z.-L.; Yang, X.-T.; Liu H.-L. Mathematical calculation of binodal curves of a polymer/solvent/non-solvent system in the phase inversion process. Desalination. **192**, 91–104 (2006).

85 Barzin, J.; Sadatnia, B. Theoretical phase diagram calculation and membrane morphology evaluation for water/solvent/polyethersulfone systems. Polymer **48**, 1620-1631 (2007).

86 Barzin, J.; Sadatnia B. Correlation between macrovoid formation and the ternary phase diagram for polyethersulfone membranes prepared from two nearly similar solvents. *J. Membr. Sci.* **325,** 92–97 (2008).

87 Li, S.G.; van den Boomgaard, Th.; Smolders, C.A.; Strathmann, H. Physical gelation of amorphous polymers in a mixture of solvent and non-solvent. *Macromolecules* **29,** 2053 (1996).

88 Han, J.; Lee, W.; Choi, J.M.; Patel, R.; Min, B.R. Characterization of polyethersulfone/polyimide blend membranes prepared by a dry/wet phase inversion: Precipitation kinetics, morphology and gas separation. *J. Membr. Sci.* **351**, 141–148 (2010).

89 Tsai, J. T.; Su, Y. S.; Wang, D. M.; Kuo, J. L.; Lai, J. Y.; Deratani, A. Retainment of pore connectivity in membranes prepared with vapor-induced phase separation. *J. Membr. Sci.* **362**, 360–373 (2010).

90 Kang, J.S.; Kim K.Y.; Lee, Y.M. Preparation of PVP immobilized microporous chlorinated polyvinyl chloride membranes on fabric and their hydraulic permeation behavior. *J. Membr. Sci.* **214**, 311–321 (2003).

91 Han, M. J.; Nam, S. T. "Thermodynamic and rheological variation in polysulfone solution by PVP and its effect in the preparation of phase inversion membrane. *J. Membr. Sci.* **202**, 55–61 (2002).

92 Wang, Y.-Q.; Su, Y.-L.; Ma, X.-L.; Sun, Q.; Jiang, Z.-Y. Pluronic polymers and polyethersulfone blend membranes with improved fouling-resistant ability and ultrafiltration performance. *J. Membr. Sci.* **283**, 440–7 (2006).

93 Susanto, H.; Ulbricht, M. Characteristics, performance and stability of polyethersulfone ultrafiltration membranes prepared by phase separation method using different macromolecular additives. *J. Membr. Sci.* **327**, 125 (2009).

94 Susanto, H; Stahra, N.; Ulbricht M. High performance polyethersulfone microfiltration membranes having high flux and stable hydrophilic property. *J. Membr. Sci.* **342**, 153–64 (2009).

95 Peng, J.M.; Su, Y.L.; Zheng, L.L.; Wang, L.J.; Jiang, Z.Y.; Chen, W,J. Separation of oil/water emulsion using Pluronic F127 modified polyethersulfone ultrafiltration membranes. *Sep. Purif. Technol.* **66**, 591–7 (2009).

96 Li, B.; Zhao, W.; Su, Y.L.; Jiang, Z.Y.; Dong, X.; Liu, W.P. Enhanced desulfurization performance and swelling resistance of asymmetric hydrophilic pervaporation membrane prepared through surface segregation technique. *J. Membr. Sci.* **326**, 556–63 (2009).

97 Sadrzadeh, M.; Bhattacharjee, S. Rational design of phase inversion membranes by tailoring thermodynamics and kinetics of casting solution using polymer additives. J. Membr. Sci. **441**, 31–44 (2013).

98 Van der Bruggen, B. Chemical modification of polyethersulfone nanofiltration membranes: A review. *J. Appl. Polym. Sci.* **114,** 630–642 (2009).

99 Kim, H.; Lee, K.-H. Effect of PEG additive on membrane formation by phase inversion. *J. Membr. Sci.* **138**, 153 (1998).

100 Reuvers, A.J.; Smolders, C.A. Formation of membranes by means of immersion precipitation. Part II. The mechanism of formation of membranes prepared from the system cellulose acetate–acetone–water. *J. Membr. Sci.* **34,** 67 (1987).

101 Boom, R.M.; Wienk, I.M.; van den Boomgaard, T.; Smolders, C.A. Microstructure in phase inversion membranes. Part 2. The role of a polymeric additive. *J. Membr. Sci.* **73,** 277 (1992).

102 Torrestiana, S.B.; Basurto, R.I.O. Effect of nonsolvent on properties of spinning solution and polyethersulfone hollow fiber ultrafiltration membranes. *J. Membr. Sci.* **152,** 19 (1999).

103 Xu, Z.L.; Qusay, F.A. Polyethersulfone (PES) hollow fiber ultrafiltration membranes prepared by PES/non-solvent/NMP solution. *J. Membr. Sci.* **233** 101 (2004).

104 Chakrabarty, B.; Ghoshal, A.K.; Purkait, M.K. Effect of molecular weight of PEG on membrane morphology and transport properties. *J. Membr. Sci.* **309**, 209 (2008).

105 Ohya, H.; Shiki, S.; Kawakami, H. Fabrication study of polysulfone hollow-fiber microfiltration membranes Optimal dope viscosity for nucleation and growth. *J. Membr. Sci.* **326**, 293–302 (2009).

106 Wang, Z.; Ma, J., The role of nonsolvent in-diffusion velocity in determining polymeric membrane morphology. *Desalination* **286,** 69–79 (2012).

107 Venault, A.; Wu, J.-R.; Chang, Y.; Aimar, P. Fabricating hemocompatible bi-continuous PEGylated PVDF membranes via vapor-induced phase inversion. *J. Membr. Sci.* **470,** 18–29 (2014).

108 Sadrzadeh, M.; Bhattacharjee, S., Rational design of phase inversion membranes by tailoring thermodynamics and kinetics of casting solution using polymer additives. *J. Membr. Sci.* **441**, 31–44 (2013).

109 Young, T.H.; Chen, L.W. Pore formation mechanism of membranes from phase inversion process. *Desalination*, ***103***, 233–247 (1995).

110 Peng, N.; Chung, T.-S.; Li, K.Y. The role of additives on dope rheology and membrane formation of defect-free Torlon® hollow fibers for gas separation. *J. Membr. Sci.* **343,** 62–72 (2009).

111 Lin, K.Y.; Wang, D.M.; Lai, J.Y. Non-solvent-induced gelation and its effect on membrane morphology. *Macromolecules,* **35 (17),** 6697–6706 (2002).

112 Fu, X.Y.; Sotani, T.; Matsuyama, H. Effect of membrane preparation method on the outer surface roughness of cellulose acetate butyrate hollow fiber membrane. *Desalination.* **233,** 10 (2008).

113 Jansen, J.C.; Buonomenna, M.G.; Figolia, A.; Drioli, E. Ultra-thin asymmetric gas separation membranes of modified PEEK prepared by the dry–wet phase inversion technique. *Desalination **193**,* 58–65 (2006).

114 Greenwood, J.M.; Johnson, J.S.; Witham, M.J. Preparation of polyethersulfone membranes, US Patent No. 6,056,903 (2000).

115 Li, J.F.; Xu, Z.L.; Yang, H. Microporous polyethersulfone membranes prepared under the combined precipitation conditions with non-solvent additives. *Polym. Adv. Technol.* **19**, 251 (2008).

116 Lin, H.; Huang, C.P.; Li, W.; Ni, C. Ismat Shah, S., Tseng, Y.-H. Size dependency of nanocrystalline TiO2 on its optical property and photocatalytic reactivity exemplified by 2-chlorophenol. *Appl. Catal*. *B,* **68(1)**, 1-11 (2006).

117 Schaep, J.; Vandecasteele, C.; Leysen, R.; Doyen, W. Salt retention of Zirfon® membranes *Sep. Purif. Technol.* **14,** 127-131 (1998).

118 Yu, L.-Y.; Shen, H.-M.; Xu, Z.-L. PVDF–TiO2 composite hollow fiber ultrafiltration membranes prepared by TiO2 sol–gel method and blending method. *J. Appl. Polym. Sci.* **113(3),** 1763-1772 (2009).

119 Gilbert, B.; Ono, R.K.; Ching, K.A.; Kim, C.S. The effects of nanoparticle aggregation processes on aggregate structure and metal uptake. *J. Colloid Interf. Sci.* **339,** 285-295 (2009).

120 Bae, T.H.; Tak,T.M. Effect of TiO2 nanoparticles on fouling mitigation of ultrafiltration membranes for activated sludge filtration. *J. Membr .Sci.* **249,** 1-8 (2005).

121 Elimelech, M.;, Zhu, X.; Childress, A.E.; Hong, S. Role of membrane surface morphology in colloidal fouling of cellulose acetate and composite aromatic polyamide reverse osmosis membranes. *J. Membr .Sci.* **127**, 101-109 (1997).

122 Li, J.H.; Xu, Y.Y.; Zhu, L.P.; Wang, J.H.; Du, C.H. Fabrication and characterization of a novel TiO2 nanoparticle self-assembly membrane with improved fouling resistance. *J. Membr. Sci.* **326**, 659-666 (2009b).

123 Luo, M.-J.; ,Zhao, J.-Q.; Tang, W.; Pu, C.-S. Hydrophilic modification of poly (ether sulfone) ultrafiltration membrane surface by self-assembly of TiO2 nanoparticles. *Appl. Surf. Sci.* **249**, 76-84 (2005).

124 Arthanareeswaran, G.; kaivelan, P.T. Fabrication of cellulose acetate–zirconia hybrid membranes for ultrafiltration applications: performance structure and fouling analysis, *Sep. Purif. Technol.* **74**, 230–235 (2010).

125 Hamid, N.A.A.; Ismail, A.F.; Matsuura, T.; Zularisam, A.W.; Lau, W.J.; Yuliwati, E.; Abdullah, M. S. Morphological and separation performance study of polysulfone/ titanium dioxide(PSF/TiO2) ultrafiltration membranes for humic acid removal. *Desalination* **273**, 85–92 (2011).

126 Zhao, S.; Wang, P.; Wang, C.; Sun, X.; Zhang, L. Thermostable PPESK/TiO2 nanocomposite ultrafiltration membrane for high temperature condensed water treatment. *Desalination* **299,** 35–43 (2012).

127 Louie, J.S.; Pinnau, I.; Ciobanu, I.; Ishida, K.P.; Ng, A.; Reinhard, M. Effects of polyether–polyamide block copolymer coating on performance and fouling of reverse osmosis membranes. *J. Membr. Sci.* **280**, 762–770 (2006).

128 Kim, S.H.; Kwak, S.-Y.; Sohn, B.-H.; Park, T.H. Design of TiO2 nanoparticle self-assembled aromatic polyamide thin-film-composite (TFC) membrane as an approach to solve biofouling problem. *J. Membr. Sci.* **211**, 157–165 (2003).

129 Yu, J.C.; Yu, J.; Hoa, W.; Zhao, J. Light-induced super-hydrophilicity and photocatalytic activity of mesoporous TiO2 thin films. *J. Photochem. Photobiol. A* **148,** 331-339 (2002).

130 Rong, M.Z.; Zhang, M.Q.; Ruan, W.H. Surface modification of nanoscale fillers for improving properties of polymer nanocomposites: a review. *J. Mater. Sci. Technol.* **22**, 787–796 (2006).

131 Yang, Y., Zhang, H., Wang, P., Zheng, Q., Li, J., The influence of nano-sized TiO2 fillers on the morphologies and properties of PSF UF membrane. *J. Membr. Sci.* **288**, 231-238 (2007).

132 Teow, Y.; Ahmad, A.; Lim, J.; Ooi, B. Studies on the surface properties of mixed-matrix membrane and its antifouling properties for humic acid removal. *J. Appl. Polym. Sci.* **128**, 3184–3192 (2013).

133 Sotto, A.; Boromand, A.; Zhang, R.; Luis, P.; Arsuaga, M.J.; Kim, J.; Van der Bruggen, B. Effect of nanoparticle aggregation at low concentrations of TiO2 on the hydrophilicity, morphology, and fouling resistance of PES–TiO2 membranes. *J. Colloid Interf. Sci*. **363**, 540–550 (2011).

134 Mulder, J. Basic Principles of Membrane Technology, *Kluwer Academic Publishers*, **383** (1996).

135 Kim, I.C.; Lee, K.H.; Tak, T.M. Preparation and characterization of integrally skinned uncharged polyetherimide asymmetric nanofiltration membrane. *J. Membr. Sci.* **183**, 235–247 (2001).

136 Wu, G.; Cui, S.G.L.; Xu, Y. Preparation and characterization of PES/TiO2 composite membranes. *Appl. Surf. Sci.* **254**, 7080–7086 (2008).

137 Razmjou, A.; Mansouri, J.; Chen, V. The effects of mechanical and chemical modification of TiO2 nanoparticles on the surface chemistry, structure and fouling performance of PES ultrafiltration membranes. *J. Membr. Sci.* **378,** 73– 84 (2011).

138 Cao, X.; Ma, J.; Shi, X.; Ren, Z. Effect of TiO2 nanoparticle size on the performance of PVDF membrane *Appl. Surf. Sci.*. **253,** 2003-2010 (2006).

139 Chen, Z.; Deng, M.; Chen, Y.; He, G.; Wu, M.; Wang, J. Preparation and performance of cellulose acetate/polyethyleneimine blend microfiltration membranes and their applications. *J. Membr. Sci.* **235**, 73–86 (2004).

140 Shin, S.J.; Kim, J.P.; Kim, H.J.; Jeon, J.H.; Min, B.R. Preparation and characterization of polyethersulfone microfiltration membranes by a 2-methoxyethanol additive. *Desalination*. **186**, 1–10 (2005).

141 Sun, H.; Liu, S.; Ge, B.; Xing, L.; Chen, H. Cellulose nitrate membrane formation via phase separation induced by penetration of non-solvent from vapor phase. *J. Membr. Sci.* **295,** 2–10 (2007).

142 Caquineau. H.; Menut, P.; Deratani, A.; Dupuy, C. Influence of the Relative Humidity on Film Formation by Vapor Induced Phase Separation. *Polym. Eng. Sci*. **43(4)**, 798-808 (2003).

143 Menut, P.; Pochat-Bohatier, C.; Deratani, A.; Dupuy, C.; Guilbert, S. Structure formation of poly (ether-imide) films using non-solvent vapor induced phase separation: relationship between mass transfer and relative humidity. *Desalination.* **145**, 11-16 (2002).

144 Matsuyama, H.; Teramoto, M.; Nakatani, R.; Maki, T. Membrane formation via phase separation induced by penetration of non-solvent from vapor phase II. Membrane morphology. *J. Appl. Polym. Sci.* **74**, 171–178 (1999).

145 Park, H.C.; Kim, Y.P.; Kim, H.Y.; Kang, Y.S. Membrane formation by water vapor induced phase inversion. *J. Membr. Sci.* **156**, 169 (1999).

146 Altinkaya, S.A.; Yenal, H.; Ozbas, B. Membrane formation by dry-cast process Model validation through morphological studies. *J. Membr. Sci.* **249**, 163–172 (2005).

147 Tsai, H.A.; Kuo, C.Y.; Lin, J.H.; Wang, D.M.; Deratani, A.; Pochat-Bohatier, C.; Lee, K.R.; Lai, J.Y. Morphology control of polysulfone hollow fiber membranes via water vapor induced phase separation. *J. Membr. Sci.* **278,** 390–400 (2006).

148 Tanaka, H. Viscoelastic phase separation, *J. Phys.: Condens. Matter.* **12,** 207 (2000).

149 Gao, L.; Tang, B.; Wu, P. An experimental investigation of evaporation time and the relative humidity on a novel positively charged ultrafiltration membrane via dry–wet phase inversion. *J. Membr. Sci.* **326**, 168–177 (2009).

150 Menut, P.; Suc, Y.S.; Chinpa, W.; Pochat-Bohatier, C.; Deratani, A.; Wang, D.M.; Huguet, P.; Kuo, C.Y.; Lai, J.Y.; Dupuy, C. A top surface liquid layer during membrane formation using vapor-induced phase separation (VIPS): Evidence and mechanism of formation. *J. Membr. Sci.* **310,** 278–288 (2008)

151 Bouyer, D.; Werapun, W.; Pochat-Bohatiera, C.; Deratani, A. Morphological properties of membranes fabricated by VIPS process using PEI/NMP/water system: SEM analysis and mass transfer modeling. *J. Membr. Sci.* **349**, 97–112 (2010)

152 Pinnau, I.; Korosa, W.J. Qualitative Skin Layer Formation Mechanism for Membranes Made by Dry/ Wet Phase Inversion. *J. Polym. Sci. Pol Phys*. **31**, 419-427 (1993)

153 Brown, G.L. Formation of films from polymer dispersions J. Polym. Sci., 22,423-434 (1956)

154 Ismail, A.F.; Ng, B.C.; Abdul Rahman, W.A.W.; Effects of shear rate and forced convection residence time on asymmetric polysulfone membranes structure and gas separation performance. *Sep. Purif. Technol.* **33,** 255-272 (2003)

155 Yip, Y.; McHugh, A.J. Modeling and simulation of non-solvent vapor-induced phase separation. *J. Membr. Sci.* **271**, 163–176 (2006)

156 Khare, V.P.; Greenberg, A.R.; Krantz, W.B. Vapor-induced phase separation effect of the humid air exposure step on membrane morphology Part I. Insights from mathematical modeling. *J. Membr. Sci.* **258**, 140–156 (2005)

157 Morgan, P.W. Condensation polymers: by interfacial and solution methods, *Polym. Rev*. **10**, 19–64 (1965)

158 Cadotte, J.E.; Cobian, K.E.; Forester, R.H.; Petersen, R.J. Continued evaluation of in situ-formed condensation polymers for reverse osmosis membranes, *NTIS Report* No. PB-253193, (1976)

159 Wang, K.Y.; Chung, T.S. Fabrication of polybenzimidazole (PBI) nanofiltration hollow fiber membranes for removal of chromate. *J. Membr. Sci.* **281**, 307–315 (2006)

160 Boussu, K.; Van der Bruggen, B.; Vandecasteele, C. Study of the characteristics and the performance of self-made nanoporous polyethersulfone membranes. *Polymer*. **47,** 3464–3476 (2006)

161 Sotto, A.; Rashed, A.; Zhang, R.-X.; Martínez, A.; Braken, L.; Luis, P.; Van der Bruggen, B. Improved membrane structures for seawater desalination by studying the influence of sublayers. *Desalination.* **287,** 317–325 (2012)

162 Oh, N.W.; Jegal, J.; Lee, K.H. Preparation and characterization of nanofiltration composite membranes using polyacrylonitrate (PAN). II. Preparation and characterization of polyamide composite membranes. *J. Appl. Polym. Sci.* **80**, 2729–2736 (2001)

163 Singh, P.S.; Joshi, S.V.; Trivedi, J.J.; Devmurari, C.V.; Rao, A.P.; Ghosh, P.K. Probing the structural variations of thin film composite RO membranes obtained by coating polyamide over polysulfone membranes of different pore dimensions. *J. Membr. Sci.* **278**, 19–25 (2006)

164 Ghosh, A.K.; Hoek, E.M.V. Impacts of support membrane structure and chemistry on polyamide–polysulfone interfacial composite membranes. *J. Membr. Sci.* **336**, 140–148 (2009)

165 Fathizadeh, M.; Aroujalian, A.; Raisi, A. Effect of lag time in interfacial polymerization on polyamide composite membrane with different hydrophilic sub layers. *Desalination.* **284,** 32–41 (2012)

166 Pendergast, M.M.; Ghosh, A.K.; Hoek, E.M.V. Separation performance and interfacial properties of nanocomposite reverse osmosis membranes. *Desalination.* **308**, 180–185 (2013)

167 Cho, Y.H.; Han, J.; Han, S.; Guiver, M.D.; Park, H.B. Polyamide thin-film composite membranes based on carboxylated polysulfone microporous support membranes for forward osmosis. *J. Membr. Sci.* **445**, 220–227 (2013)

168 Wang, K.Y.; Chung, T.; Amy, G. Developing thin-film-composite forward osmosis membranes on the PES/SPSf substrate through interfacial polymerization, AIChE **58(3),** 770–781 (2012)

169 Han, G.; Chung, T.-S.; Toriida, M.; Tamai, S. Thin-film composite forward osmosis membranes with novel hydrophilic supports for desalination. *J. Membr. Sci.* **423,** 543–555 (2012)

170 Lau, W.J.; Ismail, A.F.; Misdan, N.; Kassim, M.A. A recent progress in thin film composite membrane: A review. *Desalination.* **287,** 190–199 (2012)

171 Kong, C.L.; Kanezashi, M.; Yamomoto, T.; Shintani, T.; Tsuru, T. Controlled synthesis of high performance polyamide membrane with thin dense layer for water desalination. *J. Membr. Sci.* **362**, 76–80 (2010)

172 Wei, X.Y.; Wang, Z.; Chen, J.; Wang, J.X.; Wang, S.C. A novel method of surface modification on thin-film-composite reverse osmosis membrane by grafting hydantoin derivative. *J. Membr. Sci.* **346**, 152–162 (2010)

173 Rao, A.P.; Joshi, S.V.; Trivedi, J.J.; Devmurari, C.V.; Shah, V.J. Structure–performance correlation of polyamide thin film composite membranes: effect of coating conditions on film formation. *J. Membr. Sci.* **211**, 13–24 (2003)

174 Ghosh, A.K.; Jeong, B.H.; Huang, X.F.; Hoek, E.M.V. Impacts of reaction and curing conditions on polyamide composite reverse osmosis membrane properties. *J. Membr. Sci.* **311,** 34–45 (2008)

175 Hydranautics LFC, *Hydranautics*. Retrieved from <http://www.membranes.com/index.php?pagename=lfc> accessed on June 2015

176 GE Product Literature, *General Electric*. Retrieved from <http://www.gewater.com/lib/prod lit/index.jsp> accessed on June 2015

177 Reverse Osmosis and Nanofiltration Elements, *Dow FilmTec*. Retrieved from <http://www.dowwaterandprocess.com/products/ronf.htm.> accessed on June 2015

178 Soroush, A.; Barzin, J.; Barikani, M.; Fathizadeh, M. Interfacially polymerized polyamide thin film composite membranes: Preparation, characterization and performance evaluation. *Desalination*. **287**, 310–316 (2012)

179 Zhang, R.-X.; Vanneste, J.; Poelmans, L.; Sotto, A.; Wang, X.-L.; Van der Bruggen, B. Effect of the Manufacturing Conditions on the Structure and Performance of Thin-Film Composite Membranes. *J. Appl. Polym. Sci.* **125**, 3755-3769 (2012)

180 Petersen, R.J. Composite reverse-osmosis and nanofiltration membranes. *J. Membr. Sci.* **83**, 81 (1993)

181 Kuehne, M.A.; Song, R.Q.; Li, N.N.; Petersen, R.J. Flux enhancement in TFC RO membranes. *Environ. Prog.* **20**, 23 (2001)

182 Zworykin, V.K.; Hillier, J.; Snyder, R.L. Scanning electron microscope. *Am. Soc. Test. Mater*. **117,** 15-23 (1942)

183 Wang, Y.; Petrova, V. Nanotechnology research methods for foods and bioproducts. First Edition, *John Wiley & Sons*, 103-126 (2012)

184 Wang, Y.; Padua, G.W. Formation of zein microphases in ethanol-water. *Langmuir* **26**, 12897-12901 (2010)

185 Fang, Y.; Tolley, H.D.; Lee, M.L. Simple capillary flow porometer for characterization of capillary columns containing packed and monolithic beds. *J. Chromatogr. A*, **1217**, 6405–6412 (2010)

186 Jacobasch, H.J.; Grundke, K.; Schneider, S.; Simon, F. Surface Characterization of Polymers by Physico-Chemical Measurements. *J. Adhesion* **4**, 48 (1995)

187 International Union of Pure and Applied Chemistry, Technical Report: Measurement and Interpretation of Electrokinetic Phenomena, *Pure Appl.Chem.*, **77**, 1753-1805 (2005)

188 Gohy, J.F.; Varshney, S.K.; Jérôme, R. Water-Soluble Complexes Formed by Poly(2-vinylpyridinium)-block-poly(ethylene oxide) and Poly(sodium methacrylate)-block-poly(ethylene oxide) Copolymers. *Macromolecules* **34**(10), 3361 (2001)

189 Kumar, G.; Prabhu, K.N. Review of non-reactive and reactive wetting of liquids on surfaces. *Adv. Colloid Interface Sci.* **133**, 61–89 (2007)

190 Wulf, M.; Grundke, K.; Kwok, D.Y.; Neumann, A.W. Influence of different alkyl side chains on solid surface tension of polymethacrylatesJ. *Appl. Polym. Sci.* **77**, 2493 (2000)

191 Tadmor, R. Line energy and the relation between advancing, receding and Young contact angles. *Langmuir* **20**(18), 7659–64 (2004)

192 Young, T. An Essay on the Cohesion of Fluids. *Trans. R. Soc. Lond.* **95**, 65-87 (1805)

193. ElSherbiny, I. M.A.; Ghannam, R.; Khalil, A.S.G.; Ulbricht, M. Isotropic macroporous polyethersulfone membranes as competitive supports for high performance polyamide desalination membranes. *J. Membr. Sci.* **493**, 782–793 (2015).

194 Iritani, E.; Katagiri, N.; Ishikawa, Y.; Cao, D-Q. Cake formation and particle rejection in microfiltration of binary mixtures of particles with two different sizes. *Sep. Purif. Technol.* **123**, 214–220 (2014)

195 Zhao, Z.; Zheng, J.; Peng, B.; Li, Z.; Zhang, H.; C.Han, C. A novel composite microfiltration membrane: Structure and performance. *J. Membr. Sci.* **439**, 12–19 (2013)

196 Zhuang, X.; Shi, L.; Jia, K.; Cheng, B.; Kang, W. Solution blown nanofibrous membrane for microfiltration. *J. Membr. Sci.* **429**, 66–70 (2013)

197 Welty, J.R.; Wicks, C.E.; Wilson, R.E. Fundarnentals of Momentum. Heat and Mass Transfer. Third Edition, *John Wiley & Sons,* (1984)

198 Shi, Q.; Ye, S.; Kristalyn, C.; Su, Y.; Jiang, Z.; Chen, Z. Probing molecular-level surface structures of polyethersulfone/Pluronic F127 blends using sum-frequency generation vibrational spectroscopy, *Langmuir* **24,** 7939 (2008)

199 Suk, D.E.; Matsuura, T.; Park, H.B.; Lee, Y.M. Synthesis of a new type of surface modifying macromolecules (nSMM) and characterization and testing of nSMM blended membranes for membrane distillation, *J. Membr. Sci.* **277,** 177 (2006)

200 Maruf, S.H., Greenberg, A.R., Pellegrino, J., Ding Y. Fabrication and characterization of a surface-patterned thin film composite membrane. *J. Membr. Sci.* **452**, 11–19 (2014)